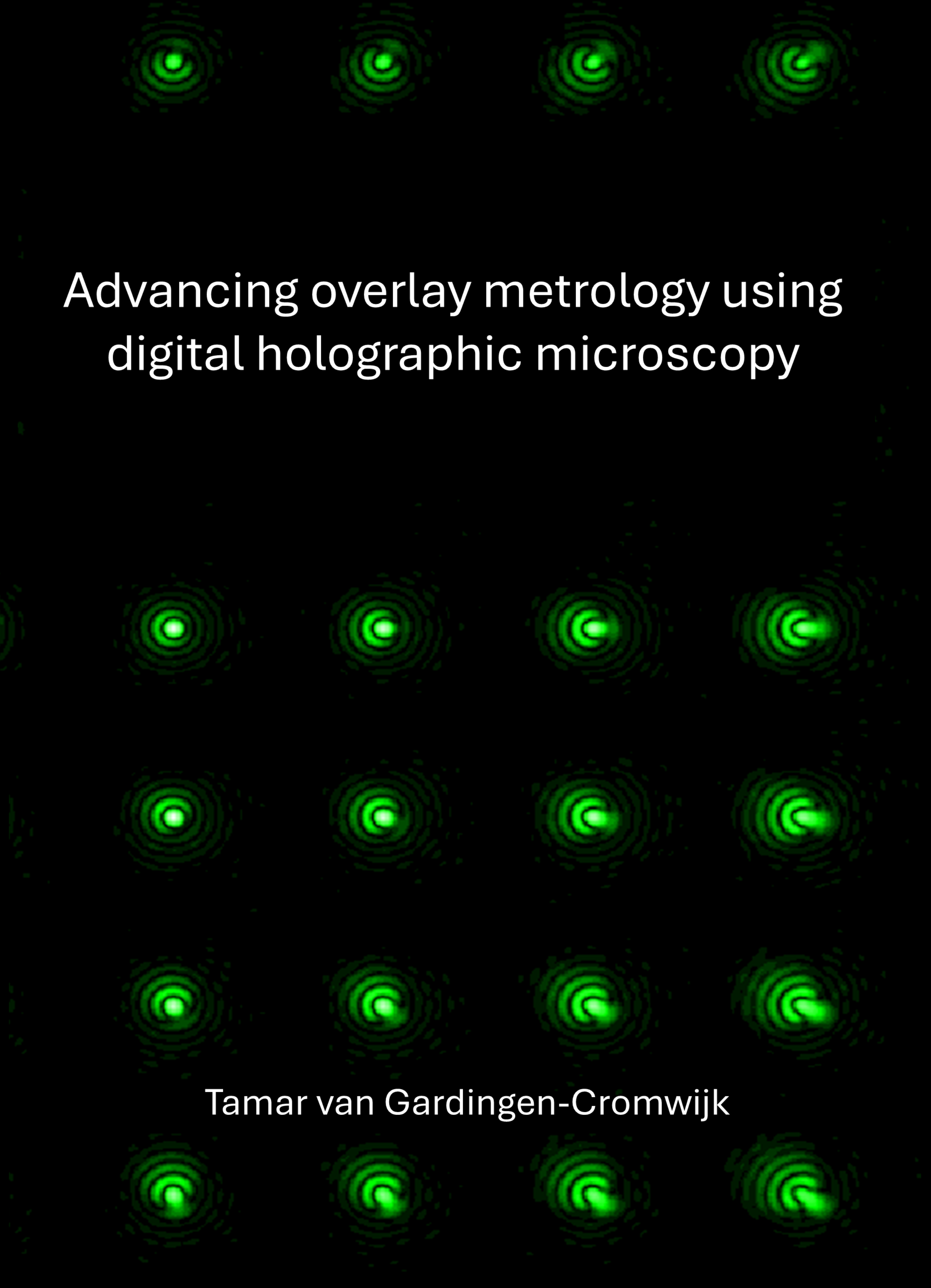

Advancing overlay metrology using digital holographic microscopy

Tamar van Gardingen-Cromwijk

ADVANCING OVERLAY METROLOGY USING DIGITAL HOLOGRAPHIC MICROSCOPY

Tamar van Gardingen-Cromwijk

Ph.D. thesis, Vrije Universiteit Amsterdam, 2025
Cover: A measured nanohole array after the first computational aberration correction step, showing the linear coma aberrations of the objective lens. Measured at 532 nm wavelength with a nanohole diameter of 200 nm and an array period of 7 µm.

ISBN: 978-94-923-2392-7

An electronic version of this dissertation is available at: research.vu.nl

VRIJE UNIVERSITEIT

Advancing overlay metrology using digital holographic microscopy

ACADEMISCH PROEFSCHRIFT

ter verkrijging van de graad van Doctor of Philosophy
aan de Vrije Universiteit Amsterdam,
op gezag van de rector magnificus
prof.dr. J.J.G. Geurts,
volgens besluit van de decaan
van de Faculteit der Bètawetenschappen
in het openbaar te verdedigen
op donderdag 3 juli 2025 om 9.45 uur
in de universiteit

door

Tamara Christina Cromwijk

geboren te Best

promotor:	prof.dr. A.J. den Boef
copromotoren:	prof.dr. J.F. de Boer
	prof.dr. S.M. Witte
promotiecomissie:	dr. L.V. Amitonova
	dr. P.J. de Groot
	dr.ir. J. Kalkman
	prof.dr. A.P. Mosk
	prof.dr. W.M.G. Ubachs

The work described in this thesis was carried out at the Advanced Research Center for Nanolithography (ARCNL), a public-private partnership between the University of Amsterdam (UvA), the Vrije Universiteit Amsterdam (VU), the University of Groningen (RUG), the Netherlands Organisation for Scientific Research (NWO), and the semiconductor equipment manufacturer ASML.

Contents

1 Introduction **1**
- 1.1 Overlay metrology . . . 3
- 1.2 Holography . . . 8
- 1.3 DHM for overlay metrology . . . 11
- 1.4 Scope of this thesis . . . 14

2 Experimental Setup **17**
- 2.1 Dark-field off-axis DHM setup . . . 18
- 2.2 Extension into the near-infrared . . . 21

3 Computational non-isoplanatic lens aberration correction **23**
- 3.1 Introduction . . . 24
- 3.2 Theory . . . 24
  - 3.2.1 Lens design . . . 25
  - 3.2.2 Aberration correction . . . 26
  - 3.2.3 Isoplanatic aberration correction . . . 27
  - 3.2.4 Pupil distortion correction . . . 28
  - 3.2.5 Singular value decomposition (SVD) based correction . . . 29
- 3.3 Experimental results . . . 31
  - 3.3.1 Non-isoplanatic aberration calibration . . . 31
  - 3.3.2 Non-isoplanatic aberration correction . . . 31
  - 3.3.3 Potential limitations . . . 34
  - 3.3.4 Near-Infrared wavelength range . . . 35
- 3.4 Conclusion . . . 37

4 Computational correction of the illuminations spot profile **39**
- 4.1 Introduction . . . 40
- 4.2 Illumination spot profile calibration . . . 41
- 4.3 Experimental results . . . 43
  - 4.3.1 Overlay target measurements . . . 43
  - 4.3.2 Robust overlay against positioning errors . . . 46
- 4.4 Conclusion . . . 49

5 Computational vibration mitigation using phase interpolation **51**

5.1 Introduction . . . 52
5.2 Theory . . . 53
  5.2.1 Vibrations in digital holographic microscopy . . . 53
  5.2.2 Phase-interpolated correction . . . 54
  5.2.3 Phase fitting method . . . 54
5.3 Method . . . 55
  5.3.1 Michelson interferometer . . . 55
  5.3.2 Digital Holographic microscopy . . . 56
5.4 Experimental results . . . 57
  5.4.1 Single frequency . . . 57
  5.4.2 Multiple frequencies . . . 59
  5.4.3 Overlay measurement . . . 60
  5.4.4 Future improvements . . . 62
5.5 Conclusion . . . 63

6 Field-position dependent spurious apodization 65
6.1 Introduction . . . 66
6.2 Theory . . . 67
6.3 Experimental results . . . 70
  6.3.1 Imaging lens . . . 70
  6.3.2 Field-position dependent apodization . . . 71
  6.3.3 Controlling the amplitude variations in the pupil plane . . . 72
  6.3.4 Comparison of the theoretical model and the experimental data . . . 73
  6.3.5 Relevance for overlay metrology . . . 75
6.4 Proposed solutions . . . 76
6.5 Conclusion . . . 77

7 Computational correction of spurious apodization for arbitrary spectral shapes using a Fourier-Transform spectrometer 81
7.1 Introduction . . . 82
7.2 Theory and System Design . . . 83
  7.2.1 Concept FT-spectrometer . . . 83
  7.2.2 Theory . . . 83
7.3 Experiment . . . 85
  7.3.1 Experimental setup . . . 85
  7.3.2 Non-linearity correction method . . . 86
7.4 Results and discussions . . . 87
  7.4.1 Validation of calibration quality . . . 87
  7.4.2 Computational spurious apodization correction . . . 89
7.5 Future improvements . . . 93
7.6 Conclusion . . . 94

8 Computational image enhancement using model-based suppression of spurious imaging effects 97
8.1 Introduction . . . 98

8.2 Methods 100
8.2.1 Model-based digital pupil filter 100
8.3 Results 101
8.3.1 Zeroth order suppression 101
8.3.2 Model-based suppression of the impact of surrounding structures . . 106
8.4 Conclusion 108

9 Conclusions and future prospects 109

Summary 112

Samenvatting 114

Bibliography 117

Curriculum Vitae 125

List of Publications 125

Ten sentences 127

Acknowledgments 128

CHAPTER 1

INTRODUCTION

'If you cannot measure it, you cannot improve it.', was stated by Lord Kelvin, a 19th-century physicist and engineer [1]. With this statement he highlighted the fundamental role of measurement in scientific research and technological development. He recognized that development depended on the ability to accurately measure and control variables, and quantify them, whether in experiments or industrial processes. This understanding remains crucial today in any field of research or engineering.

This also holds for the semiconductor industry, where integrated circuits are manufactured on a wafer [2]. Here, optical wafer metrology is a key to the manufacturing process. Integrated circuit, i.e. chips which power nearly all modern electronic devices, are made through a highly complex and precise manufacturing process that involves multiple steps, as shown in Fig. 1.1 [3]. This process sequence is repeated resulting in chips with dozens of layers. In order for a chip to work properly after manufacturing, each layer should be positioned with sub-nanometer accuracy relative to a previous layer.

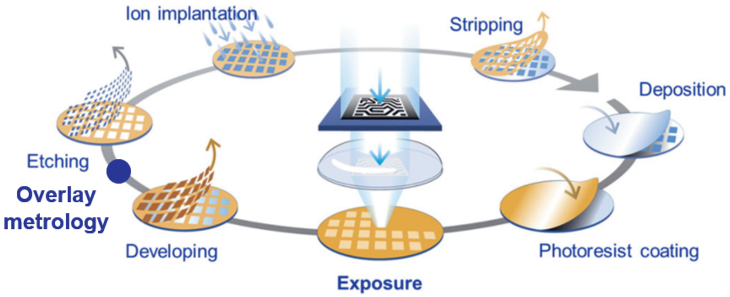

Figure 1.1: An schematic illustration of the semiconductor chip manufacturing loop.

This positioning is called overlay, which is the lateral misalignment of a newly patterned layer with respect to a previous layer in a multilayer stacked wafer. Overlay metrology is of importance for controlling the fabrication process and the early detection of problematic wafers [4]. The question of what is the best way to measure overlay precise, accurately and fast has kept the semiconductor industry engaged for decades.

In this thesis, we will explore the potential use of dark-field digital holographic microscopy (DHM) for advanced semiconductor overlay metrology. DHM distinguishes itself from other microscopy techniques by digitally recording the object as a hologram via interference of the object wave with a tilted reference wave allowing for computational corrections of the image [5–7]. The complex object image can be derived directly from the hologram using fast Fourier transform (FFT) techniques. The retrieved complex field gives access to amplitude and phase information which allows to correct for imperfections in the imaging system. We will examine its potential as a novel overlay metrology tool. Additionally, we will investigate solutions for current overlay metrology challenges, as well as those specific to DHM.

This chapter serves as a general introduction into overlay metrology and DHM. First, the concept of overlay metrology is introduced and its current challenges will be discussed. Thereafter, holography and the complex field retrieval will be explained. Next, we address the question why DHM is interesting for overlay metrology. This chapter concludes by presenting the scope of this thesis.

1.1 Overlay metrology

Overlay metrology uses optical measurement methods to quantify the overlay error. It enables real-time monitoring and feedback to lithography tools, ensuring that each layer is accurately aligned within sub-nanometer tolerances. Two commonly used methods for measuring overlay are image-based overlay metrology and diffraction-based overlay metrology, which will be explained in this section [8]. We conclude this section by discussing the current challenges in overlay metrology.

Imaged-based overlay

In imaged-based overlay (IBO) metrology high-resolution images of overlay targets are taken using optical microscope techniques [9]. IBO targets typically consist of geometric shapes, like lines and boxes, where different parts of the target lie in different layers of the multilayered stack. Fig. 1.2 shows three classical overlay marks in IBO, where the blue patterns indicate the marks in the bottom layer and the black patterns are positioned in the top layer. By measuring the relative displacement of the top and bottom patterns from the high-resolution image the overlay error can be determined.

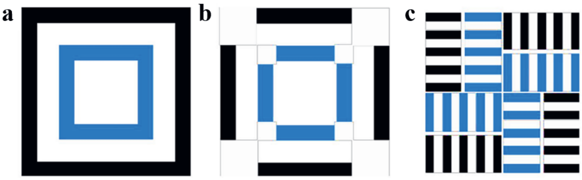

Figure 1.2: Typical imaged-based overlay marks. (a) Schematic illustration of a Box-in-Box (BiB) mark, (b) Bar-in-Bar (BiB) mark, and (c) Advanced Imaging Metrology mark (AIM).

Box-in-box (BiB) marks, Fig. 1.2 (a), were the first overlay targets used in IBO. In BiB marks the outer-box is patterned in the resist layer and the inner-box in patterned in the layer below. A microscope creates an image of the BiB target and overlay is determined from this image by measuring the position of the inner box with respect to the outer box edges. The traditional BiB marks were eventually replaced by grating marks, known as Advanced Imaging Metrology (AIM) marks [10], Fig. 1.2 (c). The grating patterns in AIM marks provide more reference points than simple BiB marks, enabling the system to detect smaller overlay errors. Despite the improved accuracy offered by AIM marks, IBO is still constrained by the optical resolution of the imaging system. As a result, it faces significant challenges to meet the sub-nanometer precision required by the semiconductor industry. Therefore, industry came up with scatterometry based analysis, the so-called diffraction-based overlay metrology.

Diffraction-based overlay

In diffraction-based overlay (DBO) metrology, overlay targets (e.g. µDBO targets) consist of two overlapping gratings, as illustrated in Fig. 1.3 (a) [11–13]. Rather than deriving overlay from the relative placement of two patterns, DBO retrieves the overlay by measuring the intensity of the diffraction orders coming from the overlapping diffraction gratings. Illuminating these overlapping grating results in a $+1^{\text{st}}$ and -1^{st} diffraction order, as shown in Fig. 1.3 (b). In case of perfect overlap, or zero overlay, the target is symmetric and hence the two diffraction orders have equal intensity. Once there is a mismatch in overlap, or an "overlay error", a difference in the intensity of the diffraction orders is measured which scales linearly with the overlay value.

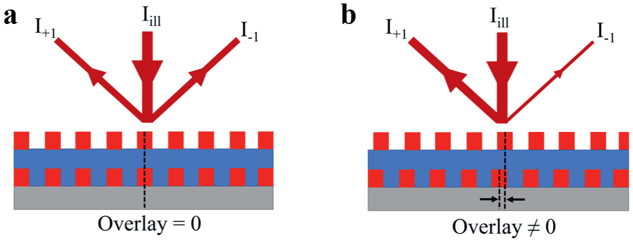

Figure 1.3: Concept of diffraction-based overlay metrology. Overlapping grating pairs, where one grating is positioned in the top layer and one grating in the bottom layer. In case of zero overlay, the $+1^{\text{st}}$ and -1^{st} intensities are equal (a). A relative lateral shift of the two gratings result in an intensity difference between the $+1^{\text{st}}$ and -1^{st} diffraction order (b).

A simplified plane wave propagation model is used here to explain the signal formation in DBO. Despite the simplification that is used, this model describes all the relevant features of DBO that are encountered in this thesis. Fig. 1.4 (a) shows a schematic illustration of this DBO signal formation, where plane waves diffract from two overlapping grating with the same pitch. The intensities I_{+1} and I_{-1} are then given by,

$$I_{+1} = |Ae^{i\alpha} + Be^{i\beta}|^2 = A^2 + B^2 + 2AB\cos(\beta - \alpha) \tag{1.1}$$

$$I_{-1} = |Ae^{-i\alpha} + Be^{i\beta}|^2 = A^2 + B^2 + 2AB\cos(\beta + \alpha) \tag{1.2}$$

where A and B are the amplitude of the diffracted waves from the top and bottom grating respectively. Here α represents the phase term introduced by the spatial translation of the top layer grating, which is proportional to overlay by the following relation:

$$\alpha = 2\pi\frac{OV}{P}, \tag{1.3}$$

where P is the grating pitch. β is the phase term of the bottom layer and depends on the optical thickness T, i.e. height difference between top and bottom layer, given by,

$$\beta \approx 4\pi\frac{T}{\lambda}, \tag{1.4}$$

where λ represents the wavelength. Since overlay values are typically small (i.e. nanometer) compared to the grating pitch P (i.e. a few hundred nanometer). Therefore, α is close to zero and the small angle approximation can be used; $\sin(\alpha) \approx \alpha$ and $\cos(\alpha) \approx 1$.

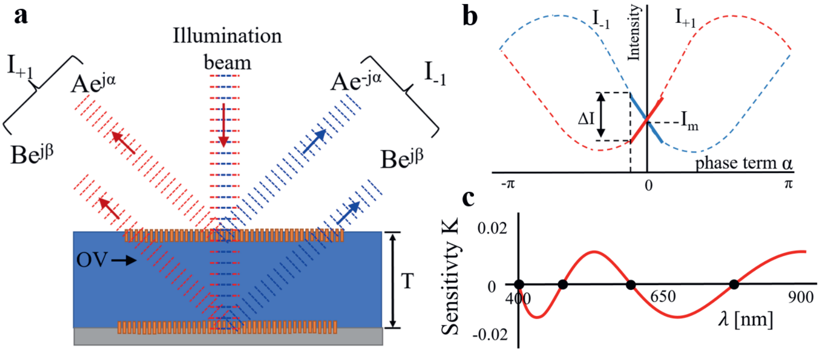

Figure 1.4: Signal formation in DBO. (a) Two overlapping grating pair with separation T. The illumination beam diffracts from the top and bottom grating, resulting in a two intensities I_{+1} and I_{-1}, which are sensitive to a relative shift between the top and bottom grating as indicated with phase term α. (b) Illustrative of intensity as function of phase term α. For small values of α the intensity functions behave linear. (c) The wavelength dependence of the sensitivity parameter K for two different grating separations T

Using this approximation the retrieved intensities I_{+1} and I_{-1} can be written as,

$$I_{+1} = A^2 + B^2 + 2AB\cos(\beta) + 4\pi\frac{AB}{P}\sin(\beta)OV, \tag{1.5}$$

$$I_{-1} = A^2 + B^2 + 2AB\cos(\beta) - 4\pi\frac{AB}{P}\sin(\beta)OV, \tag{1.6}$$

The overlay is then proportional to the relative intensity difference between the $+1^{\text{st}}$ and -1^{st} diffraction order given by,

$$\Delta I = 8\frac{AB}{P}\sin(4\pi\frac{T}{\lambda})OV. \tag{1.7}$$

For small overlay values with respect to the grating pitch, i.e. small values of α, the overlay is linearly proportional to the intensity difference ΔI, as shown in Fig. 1.4 (b). In this region, the intensity difference can be expressed as,

$$\Delta I = K \times OV, \tag{1.8}$$

where K is the unknown stack-dependent sensitivity parameter and OV overlay. This sensitivity parameter depends on the geometry of the grating, the material properties of the thin film stack and the measurement wavelength. The wavelength dependence of parameter K is shown in Fig. 1.4 (c). In order to measure overlay precisely the sensitivity K should be maximized and zero-crossing should be avoided. In Eq. 1.8, K is an unknown parameter making it impossible to calculate the overlay directly. Therefore, K will be eliminated from the equation by adding a known bias d to the overlay targets, as shown in Fig. 1.5 (a).

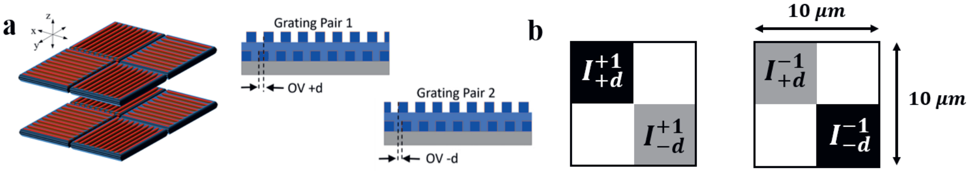

Figure 1.5: Concept of a µDBO target. (a) Two overlapping grating pair with a known bias $+d$ and $-d$ resulting in an intensity difference $+A$ and $-A$. (b) Illustrative concept of intensities on an overlay target.

One grating pair has a known bias shift of $+d$ and the second grating pair has a known bias shift of $-d$. Typically, this bias shift is 20 nm. This results in four measured intensities, I^{-d}_{+1}, I^{+d}_{+1}, I^{-d}_{-1}, I^{+d}_{-1}, where +1 and -1 refer to the diffraction orders and $+d$ and $-d$ to the biased pad which is measured, (Fig. 1.5 (b)). The four intensities lead to two measured intensity differences, given by,

$$\Delta I_+ = K \times (OV + d) = I^{+d}_{+1} - I^{+d}_{-1}, \tag{1.9}$$

$$\Delta I_- = K \times (OV - d) = I^{-d}_{+1} - I^{-d}_{-1}. \tag{1.10}$$

Combining Eq. (1.9) and Eq. (1.10) gives an expression for the overlay without the unkown sensitivity parameter K:

$$OV = d\left(\frac{\Delta I_+ + \Delta I_-}{\Delta I_+ - \Delta I_-}\right). \tag{1.11}$$

In comparison, IBO relies on directly imaging the overlay targets on the wafer. This method is fundamentally limited by the resolution of the imaging system. Moreover, IBO is highly sensitive to aberrations reducing the image quality. In contrast, DBO measures the overlay based on intensity. This approach bypasses the limitations imposed by optical resolution, allowing for more precise overlay measurements.

The intensities of the 1$^{\text{st}}$ diffraction orders coming from a DBO target can be measured in various ways. For example, ASML has developed a special dark-field microscope ("YieldStar") that images a µDBO target on a detector using only the 1$^{\text{st}}$ diffraction order. A simplified sketch of the YieldStar concept is shown in Fig. 1.6. Here, an aperture in the illumination pupil is used to illuminate the target in dark-field mode. From the two yellow quadrants in the illumination pupil the target diffracts a $+1^{\mathrm{st}}$, -1^{st} and 0^{th} order. A wedge in the detection pupil induces a spatial shift in the image plane and separate the images of the $+1^{\mathrm{st}}$, -1^{st} and 0^{th} order on the detector [14]. The images of interest, $+1^{\mathrm{st}}$ and -1^{st} diffraction orders, are then imaged in the top right and bottom left of the detector, as shown in Fig. 1.6 (b).

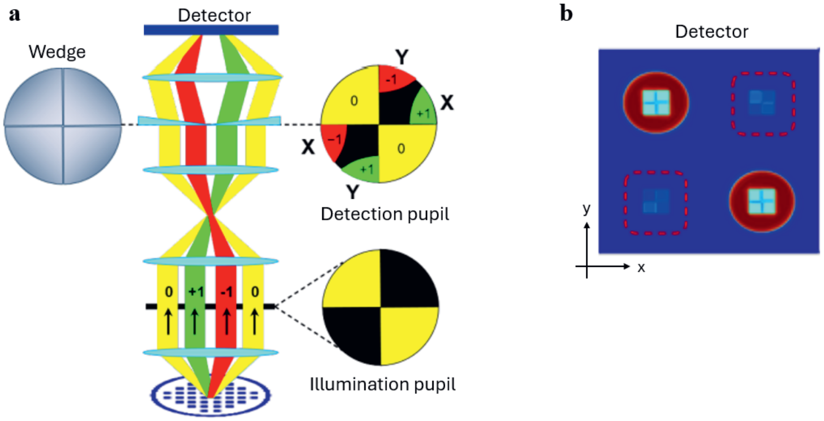

Figure 1.6: (a) A simplified sketch of Yieldstars dark-field imaging concept, resulting in an image of the μDBO target on the detector (b). [14]

Keeping up with the shrinking device dimensions, requires optical metrology to be more precise which can no longer be realized by conventional metrology at reasonable costs. In the next section, we will discuss the new challenges of overlay metrology. Thereafter, a novel overlay metrology tool will be introduced to address these new challenges.

Challenges in overlay metrology

Optical overlay metrology faces several critical challenges as the semiconductor industry pushes towards smaller device dimensions, advanced patterning techniques and increased complexity in device architectures. In this section, some of the key challenges in overlay metrology are listed:

- **Decreasing overlay tolerances:** As semiconductor nodes shrink, the critical dimensions of the device features become smaller, reducing the tolerable overlay error. Currently, requirements approach sub-nanometer accuracy levels which requires intensity level measurements in DBO with a relative precision of the order of 0.01% [15].

- **Smaller overlay targets:** It is essential to reduce the size of the target as well to minimize the metrology footprint on a wafer [16, 17]. Additionally, smaller overlay targets give more flexibility in terms of placement. However, smaller overlay structures require high image quality and resolution, resulting in expensive optics. Additionally, grating sizes in the overlay targets tend to become smaller than 3 × 3 μm^2 having only a few grating lines, resulting in target specific effect. Lastly, smaller targets are more sensitive to optical crosstalk from surrounding structures.

- **Low diffraction efficiency:** The weaker the diffracted signal from the top and bottom grating, the more difficult to measure an overlay error accurately. One of the consequences of semiconductor newest scanner, (i.e the high-NA EUV scanner), is the thin resist layer, having a layer thickness of 15 nm or less. For an overlay target this means that the scattering from the top layer is extremely weak, resulting in a low signal-to-noise ratio.
- **Material variations:** Advanced semiconductor manufacturing involves a wide variety of materials with different optical properties, such as dielectrics and metal layers. In this multi-layer stack the variation in refractive index and layer thickness can distort the optical signal used in overlay metrology. Moreover, some layers in the stack could be opaque for visible light. Therefore, an optical metrology tool should be capable of covering a wavelength range from 400 nm to 1000 nm, and ideally extend into the near-infrared range to effectively image through silicon.
- **Process-induced errors:** During manufacturing steps like etching, process-induced errors can occur in the overlay targets. Such errors can be grating deformation, grating asymmetry and thickness variations. Process-induced error can be difficult to predict and measure accurately, resulting in incorrect overlay values [18].
- **Throughput:** Semiconductor manufacturing is always pushing for high throughput, and metrology tools must keep up with production rates. Current acquisition times are in the order of a few milliseconds. Finding the right balance between through sampling for accuracy and maintaining high throughput is a major challenge, especially as device features become smaller and the cost of metrology must also stay at acceptable levels.

In this thesis, we will explore the potential use of dark-field DHM to address these challenges in overlay metrology. First, the concept of holography will be explained. Next, dark-field DHM as an overlay metrology will be discussed.

1.2 Holography

Holography is a technique that records and reconstructs the full complex-valued field using a reference wavefront. Unlike conventional imaging methods, holography retrieves both the intensity and phase information of the object under study.

History

Holography has evolved significantly since its inception. The concept was introduced in 1947 by the Hungarian electrical engineer and physicist Dennis Gabor, who used the idea of wavefront reconstruction to improve the resolution in electron microscopy [19]. Gabor was awarded the Nobel Prize in Physics in 1971, recognizing the profound impact of his ideas on imaging and optics. Although his initial work was largely theoretical and faced limitations due to the lack of coherent light sources, it laid the groundwork for future developments. His concept remained largely unexploited until the advent of laser technology in the 1960s, which enabled practical holography. The in-line configuration of Gabor's holographic setup was mainly limited by the noise resulting from a twin image. In 1962, Leith and Upatnieks successfully overcame this twin image problem, by introducing off-axis holography [20, 21]. Here, the off-axis configuration resulted in a complete separation of the twin image and the object image in the reconstruction, demonstrating the practical application of Gabor's concepts. Thereafter, Goodman and Lawrence [22], and Yaroslavskii and Merzlyakov [23] were among the first to propose the idea of recording and reconstructing holograms digitally. With the rapid development of high-resolution camera technology and computers, digital holography has emerged as a powerful tool, enabling phase and amplitude imaging in a broad range of applications such as biological imaging, telecommunication and 3D shape measurements [24].

Digital holographic microscopy

DHM acquires the coherent superposition of a reference beam and an object beam on an image sensor. From the recorded interference pattern (i.e. digital hologram) the complex-valued object field can be computationally retrieved with techniques like Fast Fourier transforms, which gives access to amplitude and phase of the object [5–7]. The reference and object fields at position r in the recording plane are given by,

$$E_o(\vec{r}) = |E_o| e^{i\phi_o(\vec{r})}, \tag{1.12}$$

$$E_r(\vec{r}) = |E_r| e^{i\phi_r(\vec{r})}, \tag{1.13}$$

where $|E_o|$ and $|E_r|$ are the amplitudes and ϕ_o and ϕ_r represent the phase of the object and reference field respectively. The coherent reference and object field interfere and the recorded intensity pattern of the digital hologram is then given by,

$$I(\vec{r}) = |E_o(\vec{r})|^2 + |E_r(\vec{r})|^2 + E_r(\vec{r})E_o^*(\vec{r}) + E_r^*(\vec{r})E_o(\vec{r}), \tag{1.14}$$

where $E_o(\vec{r})$ and $E_r(\vec{r})$ are the complex valued amplitude distributions of the object and reference beam on the image sensor position $\vec{r}$, respectively and $*$ indicates the complex conjugate. The first two terms from Eq. 1.14, $|E_o(\vec{r})|^2 + |E_r(\vec{r})|^2$, are called the auto-correlation signal (i.e DC signal) and only contain intensity information. Using holography we are interested in the cross-correlation (i.e. AC signal) terms, the third and fourth term from Eq. 1.14. These terms contain both the amplitude and phase information of the fields. These cross-correlation terms can also be expressed as,

$$
\begin{aligned}
E_r(\vec{r})E_o^*(\vec{r}) + E_r^*(\vec{r})E_o(\vec{r}) &= |E_o||E_r|(e^{-i\phi_o(\vec{r})}e^{+i\phi_r(\vec{r})} + e^{+i\phi_o(\vec{r})}e^{-i\phi_r(\vec{r})}) \\
&= 2|E_o||E_r|\cos[\phi_r(\vec{r}) - \phi_o(\vec{r})].
\end{aligned}
\tag{1.15}
$$

Eq. 1.15 shows that the cross-correlation terms depend on the relative phase difference of the reference and object field. This term is different for inline and off-axis holography. The most simple configuration is inline holography which is schematically illustrated in Fig. 1.7 (a).

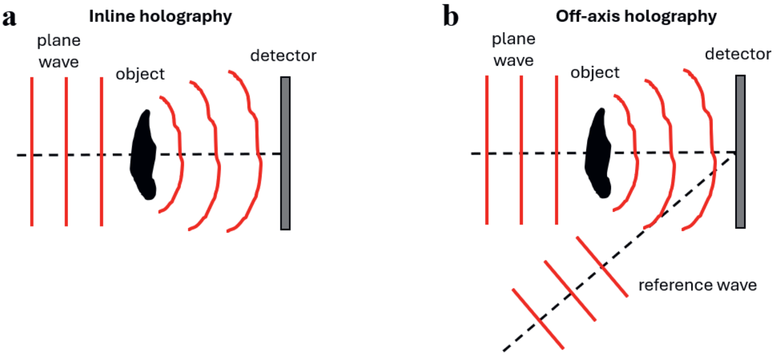

Figure 1.7: Illustration of inline (a) and off-axis (b) holography.

In case of inline holography, the object is illuminated with a plane wave. The object weakly scatters resulting in an object field and the remaining wave represents the reference field. Hence, the hologram recorded on the detector is an interference pattern of an object and reference both propagating along the same optical axis. Therefore, in the frequency domain it is challenging to extract the object field from the hologram as all four terms from Eq. 1.14 are overlapping in the center. Separation can be done by phase shifting, as was noted by Gabor, but the detectors and modulators were not available in the 1950s [19]. An elegant way to separate the cross-correlation terms from the auto-correlation signal is off-axis holography, as illustrated in Fig. 1.7 (b). Off-axis holography can be interpreted as spatial phase shifting. Here, the reference beam makes an angle with respect to the object beam, resulting in a linear phase gradient separating the cross-correlation terms from the auto-correlation signal in the frequency domain.

Complex field retrieval in off-axis holography

Fig. 1.8 (a) shows an example of an off-axis digital hologram. It can be clearly seen that the tilted reference beam results in a very dense fringe pattern [25]. By performing a FFT on this hologram, the spatial frequency spectrum is retrieved, as shown in Fig. 1.8 (b). The last two terms from Eq. 1.14, contain the phase information. In off-axis holography the terms can be fully separated from the auto-correlation signal, due to the tilt of the reference beam.[1] Selecting one of the cross-correlation terms from Eq. 1.14, shifting it to zero and performing an inverse FFT results in the retrieved complex-valued object field [26]. The complex-valued field contains both phase, Fig. 1.8 (c), and amplitude Fig. 1.8 (d) information from the object.

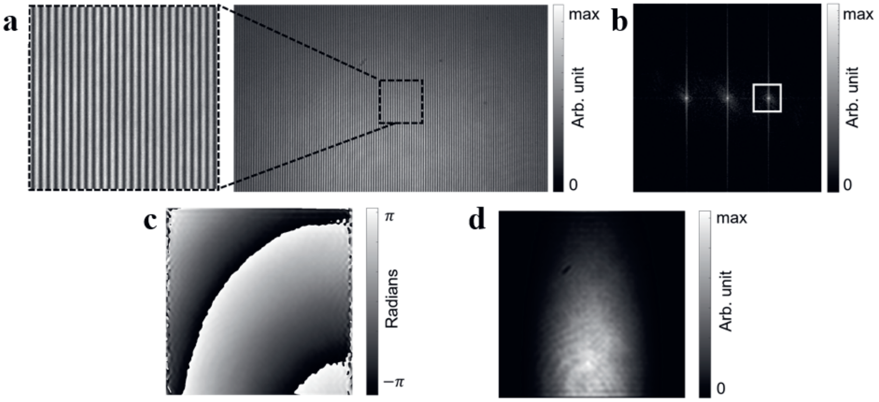

Figure 1.8: Signal retrieval in DHM. (a) Measured digital hologram with a zoomed image in the dashed box. (b) Obtained spatial frequency spectrum of the digital hologram, where the white box indicated the selected area in Fourier space. The inverse Fourier transform of selected area results in a retrieved complex object field, containing the phase information (c) and the amplitude information (d).

1.3 DHM for overlay metrology

DHM is a well-established technique for quantitative phase imaging that has been utilized for decades across various fields. However, its application in semiconductor metrology remains relatively unexplored [27]. The unique characteristics of a holographic imaging system in combination with increasingly demanding requirements encountered in semiconductor overlay metrology, call for further development of digital holography. Existing DHM applications typically use phase information, with less emphasis on amplitude details. However, in DHM for overlay metrology, achieving intensity measurements with a precision of 10^{-4} is crucial. Achieving such precision levels in DHM serves as the primary motivation for the work presented in this thesis. Each chapter in my thesis is dedicated, in some way, to achieving this 10^{-4} relative intensity precision level. Here, the concept of DHM for overlay metrology is presented.

In this thesis, we present dark-field off-axis DHM as a novel an promising approach to address the overlay metrology challenges outlined in section 1.1. The fundamental advantage of DHM is its ability to measure the complex field, retrieving an amplitude and phase, unlike conventional overlay metrology, which is limited to amplitude-only measurements. The goal is to simplify the optical hardware and address system imperfections through computational methods. The full complex field retrieval in DHM allows for such advanced signal processing. With the aid of such complex field measurement in combination with computational imaging techniques, it is possible to digitally correct in-line for lens aberrations. Additionally, DHM benefits from coherent amplification provided by the reference beam, enabling the detection of structures with low diffraction efficiency. Furthermore, the simple uncoated optics in DHM allows for imaging over a wavelength range from 400 nm to 1600 nm. Unlike conventional systems, DHM provides full NA imaging while enabling parallel acquisition of the $+1^{\text{st}}$ and -1^{st} diffraction orders, which enhances throughput and robustness in overlay measurement. First, the measurement concept of DHM for overlay metrology will be explained. Thereafter, the fundamental advantages of DHM will be discussed in detail.

---

[1] Assuming a bandwidth limited system with a NA stop

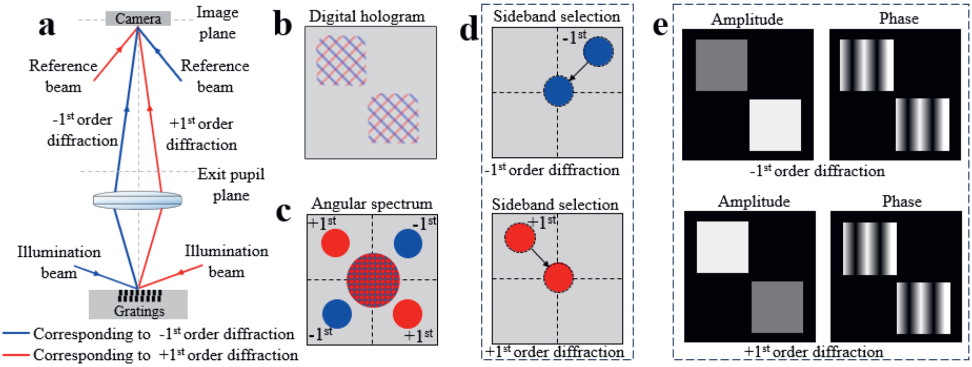
a
Camera
Image plane
Reference beam
Reference beam
-1st order diffraction
+1st order diffraction
Exit pupil plane
Illumination beam
Illumination beam
Gratings
Corresponding to -1st order diffraction
Corresponding to +1st order diffraction
b
Digital hologram
c
Angular spectrum
+1st
-1st
-1st
+1st
d
Sideband selection
-1st
-1st order diffraction
Sideband selection
+1st
+1st order diffraction
e
Amplitude
Phase
-1st order diffraction
Amplitude
Phase
+1st order diffraction

Figure 1.9: Schematic illustration of off-axis holographic recording and processing concept. **a** Schematics of the dark-field off-axis digital holography microscopy concept. **b** Recorded digital hologram with two overlapping interference patterns of the $+1^{\text{st}}$ and -1^{st} diffraction orders. **c** The spatial frequency spectrum of the digital hologram retrieved by performing an 2D-FFT. **d** Selecting the sidebands and translating them to the center of the pupil plane. **e** Reconstructed object fields via inverse FFT of the selected sideband, resulting in the retrieval of the object amplitude and phase information.

In the application of DBO metrology, both the $+1^{\text{st}}$ and -1^{st} diffraction orders should be measured. The 0^{th} diffraction order usually has no useful overlay information so, in order to use the full NA for imaging, a dark-field DHM configuration is chosen. Generally, metrology precision improves with smaller grating pitches so we illuminate the DBO targets with an oblique illumination beam which ensures that we can still collect a 1^{st} diffraction order even at longer wavelengths, as shown in Fig.1.9 (a). The $+1^{\text{st}}$ and -1^{st} diffraction order interfere with their corresponding off-axis reference fields at camera level. The resulting digital hologram intensity pattern consists of two overlapping interference patterns, as shown in Fig. 1.9 (b). Using a 2D FFT, the measured field is computationally back-propagated from the image plane to the pupil plane and an spatial frequency spectrum with a baseband and four sidebands is obtained, as schematically illustrated in Fig. 1.9 (c). The baseband is always positioned at the center of the Fourier transform of the hologram and does not contain any information about the phase of the object or angle of the reference wave. The sidebands encode all sample information, both in amplitude and phase. Due to the off-axis configuration of the reference beam, the $+1^{st}$ and -1^{st} diffraction order sidebands and their complex conjugates are fully-separated from the baseband [26, 28]. One of the sidebands is spatially filtered using a circular numerical filter which matches with the exit pupil of the objective lens and translated to the center of the pupil plane, Fig. 1.9 (d). Finally, an inverse FFT is performed on the translated sideband, which retrieves the object fields of either the $+1^{st}$ and -1^{st} diffraction orders depending on the selected sideband. The absolute value of the complex object field provides the amplitude information, and the argument of the reconstructed field provides the phase information, Fig. 1.9 (e). The retrieved amplitudes of the $+1^{st}$ and -1^{st} diffraction order images, schematically illustrated in the retrieved amplitude of Fig. 1.9 (e), will be used for DBO metrology on dedicated metrology targets. The obtained phase information will be utilized to enhance image quality in several ways.

Measuring the full complex-valued field of the $+1^{st}$ and -1^{st} diffraction using DHM has a few advantages over amplitude-only based DBO. The advantages and reasoning behind DHM as an overlay metrology tool are listed below:

- **Aberration correction:** DHM is able to correct for lens aberration since the complex field of the aberrated image is retrieved. This measured complex field can be computationally back-propagated to the exit pupil using Fourier transform techniques. In the exit pupil plane a wavefront correction can be applied. The wavefront error (i.e. aberrations) can be estimated upfront using a calibration measurement. This aberration correction results in high-image quality.

- **Simple sensor:** The computational aberration correction in DHM enables the use of optics with lower complexity and thus lower cost. Therefore, using a DHM tool for overlay metrology eliminates the need for high-quality, bulky, and expensive optics.

- **Broad wavelength range:** Expanding the wavelength range in conventional optical imaging systems is not straightforward due to the dependence on high-quality lenses with anti-reflective (AR) coatings. These coatings are wavelength-specific, limiting the usable wavelength range to a few hundred nanometers. However, DHM uses only a few optical elements that don't need AR coatings, enabling imaging across a broad wavelength range from 400 to 1600 nm, making through-silicon measurements possible.

- **Full-NA imaging:** The $+1^{st}$ and -1^{st} diffraction orders from the overlay target are incoherent with each other. As a result, both diffraction orders can utilize the full circular imaging NA of the lens, resulting in high-resolution images. Additionally, the incoherence of the $+1^{st}$ and -1^{st} diffraction order with each other allows for parallel acquisition of the $+1^{\text{st}}$ and -1^{st} diffraction order. This leads to an increase in throughput. However, a disadvantage of parallel acquisition is the shot noise of the other reference beam.

- **Computational image enhancement:** DHM's ability to computationally propagate between the image plane and pupil plane, due to its complex field retrieval, allows for advanced computational image enhancement techniques. By leveraging prior knowledge of the overlay target, model-based techniques can be applied to filter and enhance the signal of interest, thereby improving image quality.
- **Optical amplification:** In DHM a coherent reference beam interferes with the object beam. Next to providing phase information of the measured light, the reference beam also coherently amplifies the signal without adding additional noise on top of the fundamental shot noise. Optical amplification therefore offers shot-noise limited detection of very weakly scattering metrology targets even when using relatively noisy image sensors.

To summarize, the unique capabilities of DHM, such as aberration correction, computational image enhancement, and optical amplification, make it a potential tool for overlay metrology. Its ability to utilize simple optics, cover a broad wavelength range, and perform high-resolution imaging could lead to an improvement of overlay precision and accuracy. These advantages position DHM as a versatile and effective solution for the striking requirements in advanced metrology applications.

1.4 Scope of this thesis

The scope of this thesis is centered on pushing the boundaries of DHM to achieve intensity measurements with 10^{-4} precision level, which is not straightforward. As an often-used guideline, the precision of an overlay metrology tool must be about 10% of the overlay requirement [29–31]. Today, overlay requirements of some high-end semiconductor devices approach the 1 nm levels, resulting in a metrology precision that is of the order of 0.1 nm. While traditional DHM applications primarily focus on phase information, this work addresses the unique demands of overlay metrology, where such high-precision intensity measurements are essential. This defines the core objective of this research and shapes the focus of every chapter in this thesis.

This thesis aims to investigate the potential solutions to some of the big challenges of DHM as a novel overlay metrology tool. In this study, six key challenges are addressed. The questions explore the major difficulties of DHM, its practical implementation, and its potential to meet the demanding requirements of advanced metrology. Before addressing these challenges, the DHM experimental setup will be presented in Chapter 2. The used equipment will be discussed and the design choices will be explained.

In Chapter 3, a fast and accurate correction of non-isoplanatic aberrations over a wavelength range from visible to near-infrared is studied. This is done computationally in an efficient manner through co-design of a dedicated imaging lens and a three step algorithmic approach.

Next, in Chapter 4, the problem of an inhomogeneous illumination spot, caused by the oblique incidence of the illumination beam, is addressed. With experimental work, an calibration and correction method was studied to correct the inhomogeneous intensity of the illumination beam as well as the spatial profile.

A third fundamental challenge in dark-field DHM for overlay metrology comes with vibrationally challenging environments as found in high-productivity industry. Since DHM is an interferometric technique, it is inherently sensitive to undesired phase variations between object and reference beam. These phase variations lower the fringe contrast if they are integrated over a finite exposure time which leads to a reduced amplitude of the retrieved image. This results in significant overlay errors. In Chapter 5, a computational vibration mitigation method is studied using phase interpolation between a sequence of measured holograms.

While experimentally exploring these three challenges in dark-field DHM, some less foreseen challenges came across, which will be examined in the second part of this thesis. One of these unexpected phenomena is the spurious apodization caused by the finite bandwidth of the light source in combination with a wavelength-dependent focal length of the high-NA imaging lens. This effect leads to a significant field-position dependent apodization that affects the aberration-corrected point-spread function. This effect is experimentally and theoretically explored in Chapter 6. To correct for this spurious apodization, the spectrum of the source should be know accurately. Therefore, a simple FT-spectrometer with no moving parts was built and utilized to accurately measure the spectrum of the source and to leverage this information for correcting the spurious apodization, as discussed in Chapter 7.

In Chapter 8, experimental results on a model-based signal separation technique using digital pupil filtering for two different metrology challenges and demonstrate strong suppression of nuisance signals without resolution loss. This technique enables a further reduction in metrology target size while also offering opportunities to improve precision. Lastly, in Chapter 9, future prospects of this thesis are presented.

Reports on a (novel) overlay metrology technique often include an error budget that shows how stochastic and systematic error sources add-up to the required metrology precision for a certain baseline design. Examples of stochastic noise sources are laser noise, detector noise and shot-noise. Systematic error sources are, for example, imaging aberrations and illumination errors that lead to a process-dependent offset which is commonly known as Tool-Induced-Shift (TIS).

In this thesis we have made a conscious choice to not include an error budget. The main reason is that an error budget is usually made with the intent to compare the expected DHM performance with existing established overlay metrology tools. This comparison, however, is difficult to report since the relevant performance data of established metrology tools is not publicly available.

A secondary consideration is that stochastic noise source like shot noise in coherent detection schemes like DHM has already been extensively studied [32–34]. It's impact on measurement reproducibility is known and can be used in an error budget to come to a balanced trade-off between throughput and source brightness. Such a trade-off usually involves a cost-comparison between a brighter light source versus throughput gain. Such a cost comparison, however, was not considered as part of this research.

Despite the absence of an error budget, we believe that the explored new concepts and the results reported in this thesis provide valuable learnings that contribute to a performance improvement of DHM for overlay metrology.

CHAPTER 2

EXPERIMENTAL SETUP

This chapter will introduce the used dark-field DHM setup. We describe its main components and explain the design choices underlying the concept. Subsequently, we present the modifications made to extend the operational range from the visible to the near-infrared wavelength regime.

2.1 Dark-field off-axis DHM setup

The experimental data presented in this thesis is measured with our dark-field off-axis digital holographic microscope (DHM) breadboard setup. In this chapter we will describe the breadboard setup, the used components and the system criteria are discussed. A schematic representation of the DHM setup is shown in Fig. 2.1.

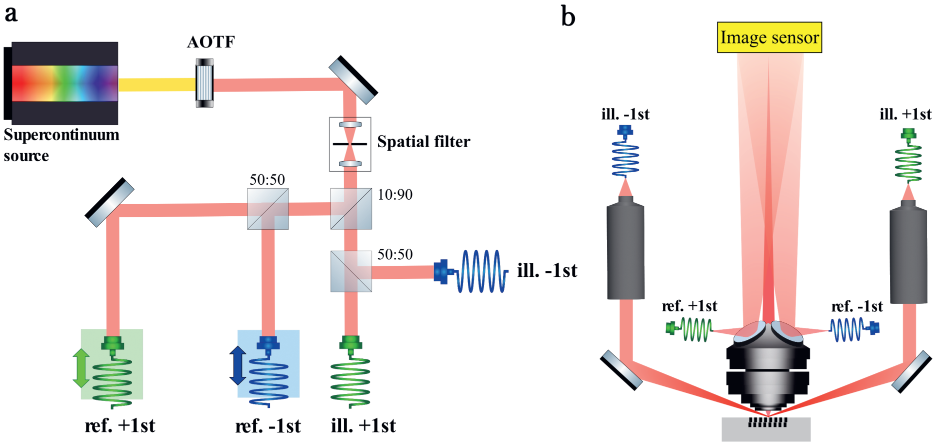

Figure 2.1: A schematic representation of the experimental setup. (a) An AOTF selects the desired wavelength coming from the spatially coherent supercontinuum white light source. The beam is cleaned from most of its speckle by the spatial filter, after which the beam is split in a reference and illumination beam by a 10:90 beamsplitter. 50:50 beamsplitters split the beam into two illumination and two reference beams. The two reference beam fibers are placed on a translation stage to create two delay lines. The beams are guided via polarization maintaining single mode fibers to the sensor head (b). At the sensor head, the light from each illumination fiber is collimated by an objective and illuminates the sample at an angle of 70°. The imaging lens captures both the $+1^{\text{st}}$ and -1^{st} diffraction orders. The diverging reference beams are reflected via a mirror on the camera.

The DHM consists of a fiber coupled Supercontinuum White light source (Leukos Rock 400) combined with an Acousto-Optical Tunable Filter (AOTF). This AOTF device provides beams with a bandwidth in the range of 3 nm to 8 nm and covers the visible range of 400 nm to 700 nm. The beam intensity from the coherent white light source is split with a 90:10 beamsplitter to create an illumination and reference beam respectively. Thereafter, a 50:50 beamsplitter is used in both paths for parallel acquisition of the $+1^{\text{st}}$ and -1^{st} diffraction orders. The light is then coupled in polarization-maintaining photonic crystal fibers (PM-PCFs), Aeroguide-15-PM from NKT, where each reference fiber is placed on a translation stage to act as a tunable delay line. The PM-PFCs transmit the light from the beamsplitting part, Fig. 2.1 (a), to sensor head, Fig. 2.1 (b). The sensor head has two off-axis illumination arms which illuminate the target from opposite directions at an incident angle of approximately 70° with respect to the normal plane of the sample. Light diffracted from the sample is then captured by the lens and imaged on the camera. The imaging lens is a custom-made objective manufactured by Anteryon [35]. The objective has a numerical aperture of 0.8 and consists of two lens elements, where one lens is an asphere. The design wavelength is 650 nm and has a focal length of 7.3 mm at the design wavelength. The magnification is this imaging system is 100×. At camera level the $+1^{\mathrm{st}}$ and -1^{st} diffracted orders coming from the object then coherently interfere with their corresponding reference beams resulting in two overlapping off-axis digital holograms. The two holograms are mutually incoherent due to a built-in optical path length imbalance which is larger than the coherence length. The camera is a Basler acA4112-gm that has a 12 Mpixel Sony IMX304 CMOS images sensor. This image sensor has a pixel pitch of 3.45 μm and the images are acquired with a 12-bit resolution.

Light source

The fiber coupled supercontinuum light source produces white light which is color filtered using an AOTF. The AOTF controls the light using acoustical waves in a crystal. The spatially coherent white light from the supercontinuum source is sent through the crystal and by tuning the frequency of the acoustic wave through the crystal, the desired wavelength of the optical wave is acousto-optically diffracted. The AOTF covers the visible regime from 400 - 700 nm.

Fibers

In a metrology tool the sensor head is preferably kept simple and light-weighted. As a result, the beamsplitting components are positioned in a separate part of the tool. In order for the light to travel from the beamsplitting part to the sensor head, fibers are used. The linear horizontal polarized light is coupled in polarization-maintaining single-mode photonic crystal fibers with a core diameter of 15 μm from NKT photonics.

Image sensor

The image sensor is an important component in our DHM setup. Firstly, the large full-well capacity of the image sensor is a valuable property of a camera for DHM. The full-well capacity is defined as the amount of charge that can be stored within an individual pixel without the pixel becoming saturated. In DHM, two object beams and two reference beams simultaneously illuminate the camera sensor, which can quickly saturate the pixels and limit the signal-to-noise ratio. As a result, DHM benefits from a camera with a large full-well. In our setup the full-well capacity is 10.2 ke^{-}. Secondly, the pixel size of the sensor plays a critical role in determining the quality, resolution, and overall performance of the imaging process. The pixel size of the camera sensor determines how finely this interference pattern of the retrieved hologram is sampled. Therefore, a small pixel size is preferred. In our setup the pixel size is 3.45 μm. This pixel size is closely related the maximum fringe density, which will be discussed below.

Off-axis reference angle

The fringe density depends on the off-axis angle of the reference beam with respect to the object beam, which also determines the separation of the auto-correlation and cross-correlation terms in the Fourier plane. The reference wave, tilted under an angle θ_{ref}, introduces a spatial frequency shift, as shown in Fig. 2.2.

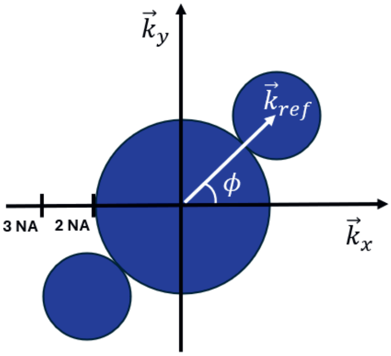

Figure 2.2: A schematic illustration of the baseband and two sideband in Fourier domain, where the position of the sideband is determined by the vector k_{ref}.

This spatial frequency shift can be expressed in the Fourier domain as,

$$|\vec{k}_{\text{ref}}| = \frac{2\pi \sin\theta_{\text{ref}}}{\lambda}. \tag{2.1}$$

The $\vec{k}_{\text{ref}}$ must satisfy two conditions in our DHM setup. Firstly, the cross-correlation signal should be completely separated from the auto-correlation term. The radius of the baseband in the Fourier domain is equal to 2NA and the sideband radius is NA. Therefore, the modulus of the reference k-vector should meet the following expression,

$$|\vec{k}_{\text{ref}}| > \frac{2\pi}{\lambda} \cdot \frac{3NA}{M}, \tag{2.2}$$

where NA is the numerical aperture of the objective and M the magnification of the setup. The condition described in Eq. 2.2 determines the minimal fringe density. The maximum fringe is determined by the Nyquist limit and related to the pixel size of the camera sensor. This Nyquist sampling theorem states that at least two pixels on the image sensor are required per period of the interference fringe,

$$f_{\text{max}} < \frac{f_s}{2} = f_N, \tag{2.3}$$

where f_{max} is the maximum frequency of the interference pattern, f_s the sampling frequency of the camera sensor and f_N the Nyquist frequency. Expressing the Nyquist limit as function of $\vec{k}_{\text{ref}}$ the following relation should hold,

$$|\vec{k}_{\mathrm{ref}}| + \frac{2\pi}{\lambda} \cdot \frac{NA}{M} < \frac{2\pi}{2p_x}, \tag{2.4}$$

where p_x indicates the pixel size. Combining Eq. 2.2 and Eq. 2.4 results in the following condition for the reference angle θ_{ref},

$$\frac{\lambda}{2p_x} - \frac{NA}{M} > \sin\theta_{\mathrm{ref}} > \frac{3NA}{M} \tag{2.5}$$

for our setup with a NA of 0.8, pixel size p_x of 3.45 µm, a magnification M of 100×, and for example a wavelength λ of 650 nm, the reference should be between 1.38° and 4.93°.

2.2 Extension into the near-infrared

A wide wavelength range is desirable due to the large variety of materials that are encountered in modern chip manufacturing. Some materials are transparent at short wavelengths (400 nm) but other materials like amorphous Carbon [36] only become transparent at longer wavelengths (> 1000 nm). To effectively manage these materials, an overlay metrology tool should preferably cover a very wide wavelength range from visible (VIS) to near-infrared (NIR) wavelengths. To explore the imaging performance of the DHM setup in the near-infrared (NIR) wavelength range, an extension in the beam splitting part has been built. A schematic representation of this setup is given in Fig. 2.3, similar to the setup described in Ref. [26]. After the fiber-coupled supercontinuum white light source (Leukos Rock 400) a dichroic mirror with a 950-nm cutoff wavelength is used to split the wavelength range into two different parts. One covers the visible regime, and the second covers the NIR wavelength range, as indicated in Fig. 2.3 (a) in green and red, respectively. For the longer wavelengths in the NIR regime, a filter wheel containing interference filters is used. The filters cover 1064 nm and a range of 1100 - 1600 nm in steps of 100 nm with a bandwidth varying from 10 nm to 12 nm.

After tuning the wavelength, the beam intensity is split using 70:30 beamsplitter for the NIR regime, to create an illumination and reference beam respectively. Two different beams splitting paths are realized for the visible and NIR wavelength range because the beamsplitters have wavelength dependent coatings. Thereafter, a non-polarizing 50:50 beamsplitter is used in both paths for parallel acquisition of the $+1^{\mathrm{st}}$ and -1^{st} diffraction orders. For the NIR regime the camera Aval ABA-013VIR-GE with Sony IMX990 sensor is used. This image sensor has 1296×1032 pixels in, respectively, the horizontal and vertical direction with a 5 µm pixel pitch.

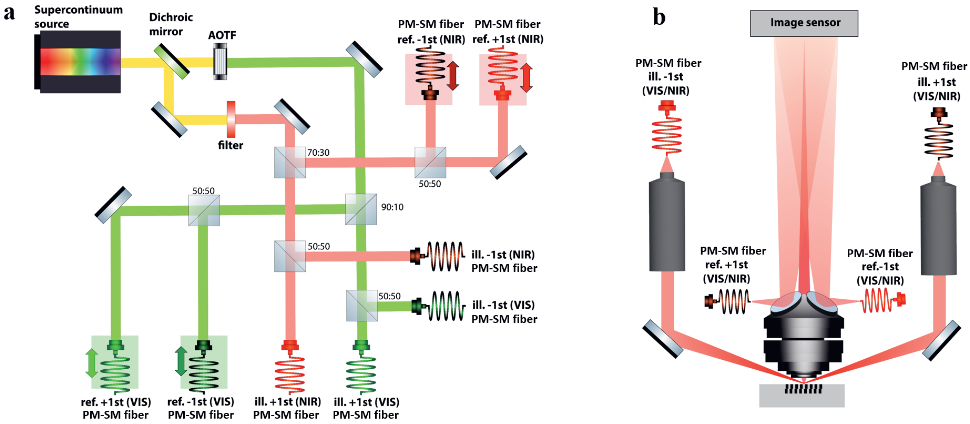
a
Supercontinuum source
Dichroic mirror
AOTF
filter
PM-SM fiber ref. -1st (NIR)
PM-SM fiber ref. +1st (NIR)
70:30
50:50
50:50
90:10
50:50
ill. -1st (NIR) PM-SM fiber
50:50
ill. -1st (VIS) PM-SM fiber
ref. +1st (VIS) PM-SM fiber
ref. -1st (VIS) PM-SM fiber
ill. +1st (NIR) PM-SM fiber
ill. +1st (VIS) PM-SM fiber
b
Image sensor
PM-SM fiber ill. -1st (VIS/NIR)
PM-SM fiber ill. +1st (VIS/NIR)
PM-SM fiber ref. +1st (VIS/NIR)
PM-SM fiber ref.-1st (VIS/NIR)

Figure 2.3: A schematic representation of the NIR extension. **a** The beamsplitter part of the setup consists of two parallel beam paths. The supercontinuum source is split via a dichroic mirror with a cut-off wavelength of 950 nm in two beams. One for the visible regime (400-700 nm), where the wavelength is tuned using an AOTF and the other beam for the near-infrared (NIR) (1064-1600 nm) tuning the wavelength with an interference filter. Each beam is split into a reference and illumination beam using a 90:10 and 70:30 beamsplitter for the visible and NIR regime respectively. Afterward, 50:50 beamsplitters split the beam into two illumination and two reference beams. The beams are guided via polarization maintaining single mode fibers to the sensor head. **b** The illumination beams coming from the fibers are collimated by an objective and are diffracted on the sample under an angle of 70°. The imaging lens captures both the $+1^{\mathrm{st}}$ and -1^{st} diffraction orders. Each diverging reference beams is redirected via a mirror to the image sensor.

CHAPTER 3

COMPUTATIONAL NON-ISOPLANATIC LENS ABERRATION CORRECTION

The dark-field digital holographic microscope uses a simple two-element imaging lens with a high numerical aperture and is capable of imaging from the visible to near-infrared regions. This combination of high resolution and large wavelength coverage was achieved by combining a simple imaging lens with a fast and accurate computational correction of non-isoplanatic aberrations. We present experimental results for overlay metrology targets that demonstrate the capability of our computational aberration correction in the visible and near-infrared wavelength regimes, which helps to advance semiconductor metrology.

Published as: T. van Gardingen-Cromwijk, S. Konijnenberg, W. Coene, M. Adhikary, T. Tukker, S. Witte, J. F. de Boer and A. den Boef, *Non-isoplanatic lens aberration correction in dark-field digital holographic microscopy for semiconductor metrology*, Light: Advanced Manufacturing 4, **36** (2023).

3.1 Introduction

Dark-field and multi-wavelength digital holographic microscopy (DHM) has already been described [37–42] for various imaging applications like detecting sub-wavelength particles with large contrast [37, 38], contrast enhancement in biological imaging [39], speckle-reduction [41] and improved surface profiling [42].

Herein, we present an off-axis dark-field DHM as an overlay metrology tool that can image over a wide wavelength range, from visible (VIS) to near infrared (NIR) wavelengths. The novel aberration correction capabilities of df-DHM reported in this study offer high imaging quality over a large field of view using a relatively simple custom-made high numerical aperture (NA) imaging lens. High-NA imaging, in combination with simple optics, introduces field position-dependent or non-isoplanatic aberrations in the imaging system. In this chapter, we describe a fast computational correction method that allows us to correct non-isoplanatic aberrations computationally with DHM and present the experimental results over a wide wavelength range from VIS to NIR. Wafer metrology is a new field that combines digital post-processing algorithms for non-isoplanatic aberration correction with custom-made optical design approaches. In astronomy, this technique was adopted a few years ago [43, 44]. However, in the context of astronomy the aberration corrections have been applied to incoherent systems whereas we are working with a coherent imaging system. Moreover, in astronomy, the throughput is irrelevant, whereas in the semiconductor industry, high throughput is a key indicator of a good metrology tool. In the next section, we present the processing steps and algorithms of the aberration correction method. In the Results section, we present additional experimental results obtained using aberration correction theory. Finally, we conclude by summarizing our findings.

3.2 Theory

The resolution of an imaging system improves when the NA of lenses increases. Therefore, a high-NA lens is required to create sharp images of small overlay metrology targets. Moreover, a high NA allows us to capture diffraction orders from metrology gratings over a wide range of pitches and wavelengths, thereby enabling robust overlay metrology [3, 45]. In this study, a 0.8-NA, two-element imaging lens was used. The drawback of a high NA in combination with only two uncoated lens elements is field position-dependent aberrations. Each object point within the field-of-view (FoV) experiences different aberrations. Such field position-dependent aberrations are also called non-isoplanatic aberrations, spatially varying blur, or 4D aberrations, wherein two dimensions are in the image plane and two dimensions are in the pupil plane [46].

These non-isoplanatic aberrations can be corrected computationally because DHM retrieves the phase and amplitude information of the object via the sidebands of the Fourier transform of the hologram. These sidebands represent the interference between the object wave and the reference wave. Using computational techniques, we can easily correct field position-independent aberrations or isoplanatic aberrations, such as spherical aberrations, with a simple deconvolution, which is performed as a multiplication in the Fourier space [47]. Such deconvolution is computationally inexpensive. Non-isoplanatic aberrations can be corrected by applying deconvolution per object point for a given area of the considered FoV, which is computationally expensive. To make non-isoplanatic aberration correction efficient, we focused on a certain class of field-dependent aberrations that can be easily corrected via pupil distortion. This leads to a correction method based on the following three steps:

1. Isoplanatic aberration correction
2. Pupil distortion correction
3. Singular value decomposition (SVD) correction

The SVD-based method can correct all arbitrary field position-dependent aberrations. However, its computational expense scales with the extent to which aberrations vary as a function of the field position. Therefore, for speed and computational expense, it is important to first correct the aberrations as much as possible using deconvolution and pupil distortion. The aberration correction steps are described in detail in this section. Before proceeding with the correction procedure, the lens design is discussed.

3.2.1 Lens design

Our imaging lens is the result of a co-optimization between an optical design and signal-processing algorithms [43, 44]. The lens has been co-designed with as few lens elements as possible and only allows aberrations that are easy to correct computationally using the algorithms reported in this paper.

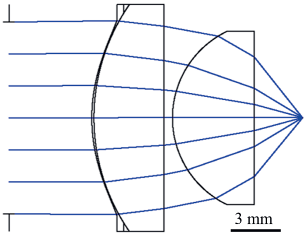

Figure 3.1: Schematic illustration of the two-element high-NA lens.

The custom-made imaging lens was manufactured by Anteryon (www.anteryon.com). It has an NA of 0.8 and consists of two uncoated lens elements, one of which is a plano-asphere, as shown in Fig. 3.1.

The lens is manufactured using a replication process [48, 49] and is fixed in a holder on which the reference beam mirrors are integrated such that the angle between the reference and object beam is optimised. The combination of a high NA and only two

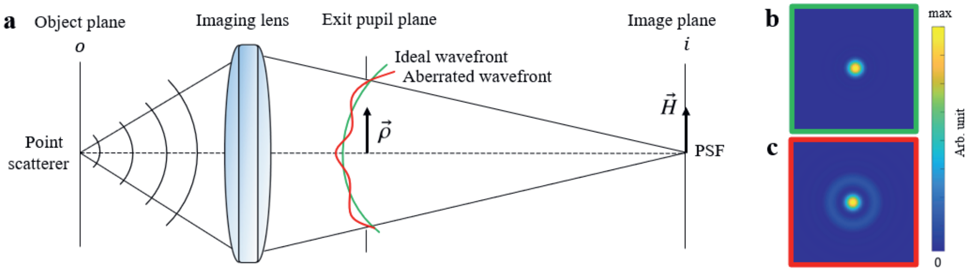

Figure 3.2: Imaging system characterized by its point-spread function (PSF) for one point in the field. Per point in the field the corresponding PSF is different due to non-isoplanatism. (a) Schematic representation of a point scatterer illuminating the imaging lens with spherical waves. (b) An aberration free imaging lens results in an ideal spherical wavefront and a diffraction-limited PSF in the image plane. (c) A non-ideal lens deforms the wavefront resulting in an aberrated PSF presented for the case of spherical aberrations.

lens elements yielded high field position-dependent aberrations, indicating that each field position yielded a different point spread function (PSF) in the image plane.

The lens was designed such that the aberrations correctable via pupil distortion, such as linear coma, have limited restrictions. All other field position-dependent aberrations, such as astigmatism, were minimised. This lens design allows the correction of non-isoplanatic aberration with low computational effort.

3.2.2 Aberration correction

In general, an imaging system is characterised by its PSFs, which are images of a single point source in an object, as shown in Fig. 3.2 (a). An optical system with a perfect imaging lens results in an ideal spherical wavefront and a diffraction-limited PSF, i.e. an Airy Disk, as shown in Fig. 3.2 (b). However, a non-ideal lens deforms the wavefront, resulting in an aberrated PSF, as shown Fig. 3.2 (c). Fig. 3.2 shows the aberrated PSF for one point in the field. Per point in the field the corresponding PSF is different due to non-isoplanatism. Generally, the aberration correction can be described as the inverse of the linear transformation of an 2D object function to an 2D image function. Mathematically speaking, such transformation can be defined in terms of an impuls response for all points, resulting in a 4D function. This function can be interpreted as a black box independent of the geometry of the lens. The 2D Fourier transform serves as a mathematical tool to describe the 4D transformation.

The mathematical relation between the object field $o(\vec{H})$ and the image field $i(\vec{H})$ is given by

$$i(\vec{H}) = FT^{-1}\left[\tilde{A}(\vec{\rho})\int e^{i\tilde{W}(\vec{\rho},\vec{H})}e^{i\vec{\rho}\cdot\vec{H}}o(\vec{H})\,d\vec{H}\right], \tag{3.1}$$

where FT denotes a 2D Fourier Transform, $\vec{H}$ denotes the coordinate vector in the object plane, $\vec{\rho}$ is the vector in Fourier space of the exit pupil plane, $\tilde{A}$ is the aperture function, $\tilde{W}$ is the non-isoplanatic aberration function and $\sim$ denotes a function in pupil space. The non-isoplanatic aberration function $\tilde{W}$ from Eq. 3.1 can be described with three terms,

$$\tilde{W}(\vec{\rho},\vec{H}) = \tilde{W}_{\mathrm{iso}}(\vec{\rho}) + \tilde{f}(\vec{\rho})\,\vec{H}\cdot\vec{\rho} + \delta\tilde{W}(\vec{\rho},\vec{H}). \tag{3.2}$$

Each term of Eq. 3.2 is corrected in one of the three aberration correction steps. The first term is corrected in the isoplanatic aberration correction step. The pupil distortion correction step corrects the second term of Eq. 3.2. Finally, during the SVD correction, the third aberration term, which comprises all the remaining aberrations given by $\delta\tilde{W}$, will be corrected.

3.2.3 Isoplanatic aberration correction

In the case of isoplanatic aberrations, the PSF deformation is constant over the FoV, i.e. field position-independent. Previously, we demonstrated the computational correction of isoplanatic aberrations via a single deconvolution of one PSF in the context of overlay metrology, as this was allowed for the lower NA lens used at a substantially smaller wavelength range [47]. In this method, a nano-sized point scatterer is imaged in the centre of the FoV, resulting in the retrieval of the wavefront aberration of the imaging lens. As the first correction step, deconvolution is applied to a measured image field by multiplying the field with the conjugate wavefront aberration in the Fourier space for a PSF, preferably selected at a location in the FoV close to the nodal point. The nodal point is the point of the optical system for which an incoming ray leaves the system with the same direction. For a curved surface, such as the imaging lens, the nodal point is located at the centre of the curvature of the surface.

For the correction of the isoplanatic aberration, the aberrated complex-valued image field $i(\vec{H})$ is retrieved from the camera in real space given by

$$i(\vec{H}) = h(\vec{H}) * o(\vec{H}), \tag{3.3}$$

where $h(\vec{H})$ represents the selected 2D PSF close to the nodal point in field space. By performing a 2D Fourier transform, we back-propagate the aberrated image field to the exit pupil in pupil space given by

$$\tilde{i}(\vec{\rho}) = \tilde{h}(\vec{\rho}) \cdot \tilde{o}(\vec{\rho}). \tag{3.4}$$

In pupil space, a deconvolution multiplication is performed on the aberrated image field $\tilde{i}(\vec{\rho})$ with the complex conjugate of the retrieved transfer function $\tilde{h}(\vec{\rho})^*$ to correct for the isoplanatic part $\tilde{W}_{\mathrm{iso}}$ of the aberration function in Eq. 3.2. This results in the following Wiener deconvolution, yielding the isoplanatic-aberration corrected object field in pupil space

$$\tilde{o}_{c1}(\vec{\rho}) = \frac{\tilde{h}(\vec{\rho})^*}{|\tilde{h}(\vec{\rho})|^2 + \epsilon} \cdot \tilde{i}(\vec{\rho}), \tag{3.5}$$

where ϵ is a non-zero positive value that mitigates the amplification of noise. Performing an inverse Fourier transform results in the isoplanatic-aberration corrected object field in field space, given by $o_{c1}(\vec{H})$. In the following part, the remaining non-isoplanatic correction steps will be explained.

3.2.4 Pupil distortion correction

As mentioned previously, non-isoplanatic aberrations can be corrected by applying deconvolution per object point. This method is computationally expensive because the computational expense scales with the degree of non-isoplanatism. This is not the case for pupil distortion. Pupil distortion represents non-isoplanatic aberrations that can be efficiently computationally corrected via coordinate remapping.

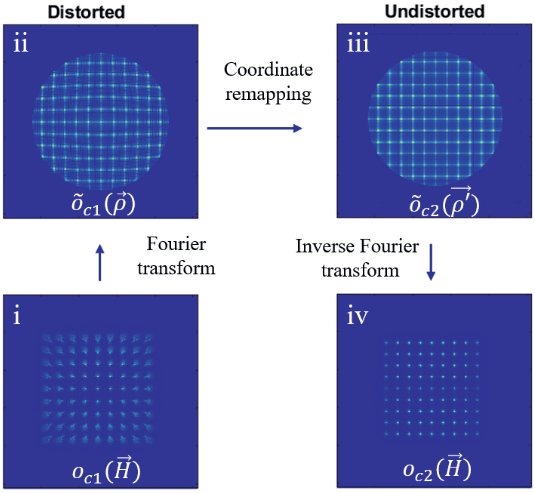

Figure 3.3: Simulated pupil distortion correction approach with the corresponding fields where (i)-(iv) indicates the sequential order of steps taken during the pupil distortion correction. (i) aberrated amplitude image simulated nano-hole test grid with arbitrary dimensions. (ii) Fourier transform of distorted image plane (i). (iii) Pupil plane after remapping of the pupil plane coordinates. (iv) Retrieved undistorded amplitude of the simulated test grid after pupil distortion correction.

As shown in Fig. 3.3, we computationally correct the pupil distortion by remapping the coordinates of the aberrated pupil plane. First, the isoplanatic corrected object field in field space $o_{c1}(\vec{H})$ is moved to the pupil field by Fourier transform, resulting in $\tilde{o}_{c1}(\vec{\rho})$. Then, in pupil space, the distortion is corrected by remapping the coordinates $\vec{\rho}$ of the distorted pupil field $e^{if(\vec{\rho})\vec{H}\cdot\vec{\rho}}$ to the coordinates $\vec{\rho}'$ of the undistorted pupil field, where

$f(\vec{\rho})$ represents the distortion strength. This distortion correction method can be shown in detail using coma aberrations as an example of pupil distortion. The wavefront deformation for low-order coma (W_{131}) is absent at the nodal point close to the center of the FoV, and increases linearly with the field coordinate $\vec{H}$ inside the FoV according to [46],

$$f(\vec{\rho}) = W_{131}(\vec{\rho}\cdot\vec{\rho}). \tag{3.6}$$

In combination with the phase of the regular factor in the Fourier transform relation given by $(\vec{H}\cdot\vec{\rho})$, one can rewrite Eq. 3.6 as

$$(\vec{H}\cdot\vec{\rho}) + f(\vec{\rho})(\vec{H}\cdot\vec{\rho}) = (\vec{H}\cdot\vec{\rho})(1 + W_{131}|\rho|^2). \tag{3.7}$$

After the correction, the coordinates correspond to the undistorted coordinates $\vec{\rho'}$ given by

$$(\vec{H}\cdot\vec{\rho})(1 + W_{131}|\rho|^2) \Rightarrow (\vec{H}\cdot\vec{\rho'}). \tag{3.8}$$

Therefore, the pupil coordinate remapping for only coma aberration W_{131} is given by

$$\vec{\rho}(1 + W_{131}|\rho|^2) \Rightarrow \vec{\rho'}, \tag{3.9}$$

where the factor W_{131} defines the distortion strength. This pupil coordinates remapping results in a distortion-corrected object field in pupil space given by $\tilde{o}_{c2}(\vec{\rho'})$. Then, performing an inverse Fourier transform results in the isoplanatic aberration and distortion-corrected intermediate object field in field space, given by $o_{c2}(\vec{H})$. This method is computationally efficient since it only contains two simple Fourier Transforms independent of the amount of pupil distortion.

3.2.5 Singular value decomposition (SVD) based correction

Next, to correct for remaining small residual aberrations, a more general correction method based on SVD is applied. The non-isoplanatic aberrated image, Eq. 3.10, can be described as a linear system with a 4D-PSF matrix denoted $H_{4\mathrm{D}}$ between the object o and the image i,

$$i = H_{4\mathrm{D}}\cdot o. \tag{3.10}$$

Since direct inversion is computationally very inefficient due to the large size of $H_{4\mathrm{D}}$, we assume that in a small region around a certain image point the PSF is approximately constant. This way, we can locally correct the image by applying a deconvolution with the PSF at that point. In order to apply $H_{4\mathrm{D}}$ and its inverse in a computationally efficient manner, we introduce an SVD-based deconvolution. The local deconvolution kernels for the 2D-PSFs, which remain after the first two correction steps, for all object points are reshaped into 1D columns, and are put in the transfer matrix C which has the following SVD-decomposition

$$C = U\cdot S\cdot V^T, \tag{3.11}$$

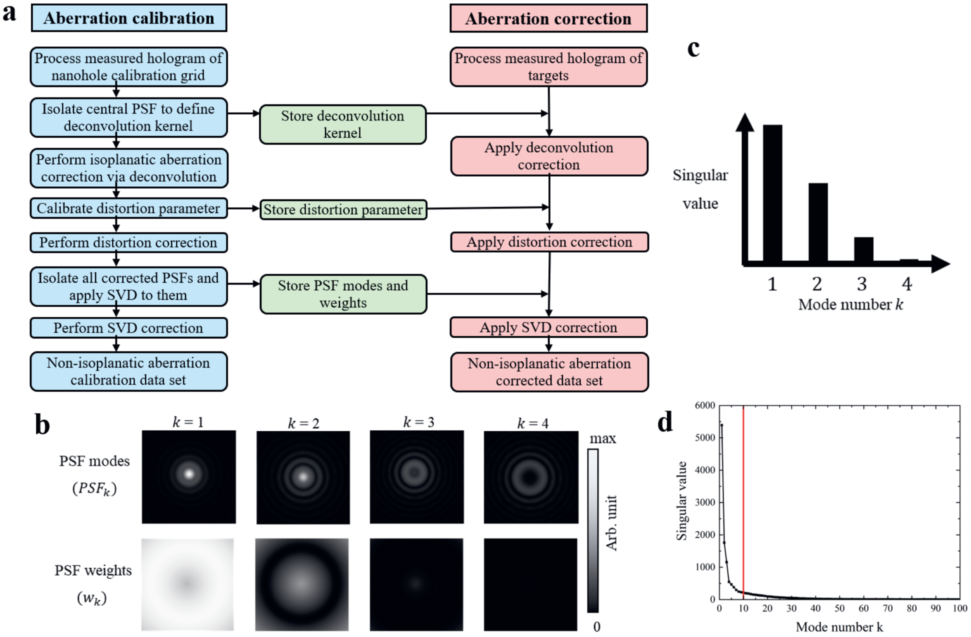
a
Aberration calibration
Process measured hologram of nanohole calibration grid
Isolate central PSF to define deconvolution kernel
Perform isoplanatic aberration correction via deconvolution
Calibrate distortion parameter
Perform distortion correction
Isolate all corrected PSFs and apply SVD to them
Perform SVD correction
Non-isoplanatic aberration calibration data set
Store deconvolution kernel
Store distortion parameter
Store PSF modes and weights
Aberration correction
Process measured hologram of targets
Apply deconvolution correction
Apply distortion correction
Apply SVD correction
Non-isoplanatic aberration corrected data set
c
Singular value
1
2
3
4
Mode number k
b
$k = 1$
$k = 2$
$k = 3$
$k = 4$
PSF modes
(PSF_k)
PSF weights
(w_k)
max
Arb. unit
0
d
Singular value
6000
5000
4000
3000
2000
1000
0
0
10
20
30
40
50
60
70
80
90
100
Mode number k

Figure 3.4: Supporting algorithm diagrams (a) Algorithm flowchart of non-isoplanatic aberration calibration and correction. (b) Simulated example of PSF modes and their corresponding weights. (c) Diagram of the singular value as function of mode number k from (b). (d) Experimentally obtained singular values as function of the mode number k with $k_{\max} = 10$ indicated with the red line.

where U is a matrix with its columns comprising the modal isoplanatic 2D-deconvolution kernels denoted by $U = d_k(\vec{H})$, where k denotes the column index of matrix U. The second part of Eq. 3.11 is a 2D matrix describing the 2D modal weight factors, which represents the non-isoplanatism, $S \cdot V^T = w_k(\vec{H})$, where k represents the row index of matrix $S \cdot V^T$. The aberration-corrected object-field is now obtained by performing the SVD-based deconvolution for 4D aberrations given by

$$o_{c3}(\vec{H}) = \sum_{k=1}^{k_{\max}} d_k(\vec{H}) * [w_k(\vec{H}) \cdot o_{c2}(\vec{H})], \tag{3.12}$$

where k_{max} denotes the number of used SVD-modes. By applying this SVD-theory one could describe each PSF in the FoV as a sum of PSF modes with a corresponding weight factor, as shown in a simulated example in Fig 3.4 (b).

The singular value represents the contribution of a certain PSF mode to the measured PSFs in the FoV, as illustrated in Fig 3.4 (c). The computational load of the SVD increases with the number of PSF modes defined as $k_{\max}$ and equals $(k_{\max} + 1)$ times a 2D-FFT. In this study, the singular value as function of mode number k decays exponentially, as shown in Fig 3.4 (d). Therefore, a value of 10 is chosen for $k_{\max}$. The overall aberration correction theory is translated into an algorithm, and the flowchart is presented in Fig. 3.4 (a). The algorithm is split into a calibration part and a correction part, which will be discussed in the Experimental results section.

3.3 Experimental results

In this section, we present an experimental demonstration of the non-isoplanatic lens aberration calibration and correction. First, the calibration procedure of the 4D PSFs with a specific calibration sample and the corresponding results are presented. Next, we present the non-isoplanatic aberration correction for dedicated overlay target images.

3.3.1 Non-isoplanatic aberration calibration

Calibration of the field position-dependent aberrations is required to perform the non-isoplanatic aberration correction described in the Theory section. The calibration sample consists of a 2D grid of nanoholes. The nanoholes were fabricated on a Si wafer with a SiN etching layer using E-beam lithography. Each nanohole, having a cylindrical shape with a diameter and depth of 100 nm, acts as a point scatterer by diffracting spherical waves. During calibration, the complex-valued image field of a nanohole grid is measured to determine the local PSF and thereby the aberrations at different object-field positions. Thus, the nanoholes probe the spatial variation of the 4D aberrations via multiple local PSFs. An example of a measured $70 \times 70\ \mu\text{m}^2$ calibration grid with a pitch of 7 µm is given in Fig. 3.5 (a). This calibration grid is measured using a wavelength of 532 nm.

From the measured field position-dependent PSFs presented in Fig. 3.5, it is clear that the aberrations contain a high amount of linear coma that increases towards the edges of the FoV, as indicated by the enlarged section in Fig. 3.5 (b). The tails of the PSFs point towards the nodal point of the optical system, shown in Fig. 3.5 (c). In our approach, there is a close cross-link between the correction and calibration of the aberrations. Because the calibration data and the target data follow the same processing steps, any uncertainty in the calibration grid centered at the nodal point is resolved. The center of the calibration grid therefore only needs to be roughly at the position of the nodal point.

3.3.2 Non-isoplanatic aberration correction

The calibration measurement presented in the previous section is used to perform computational correction following the three correction steps described in the Theory section. The purpose of the df-DHM setup is to measure overlay on dedicated overlay targets with different pitches. A test wafer with dedicated targets is used to verify the performance of the proposed correction approach. The gratings in the bottom layer are etched

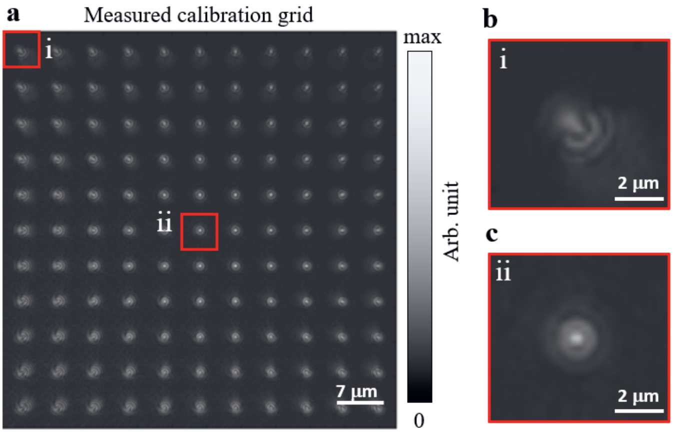

Figure 3.5: Retrieved amplitude of a measured nanohole-calibration grid. (a) 70 × 70 µm nano-hole calibration grid with a pitch of 7 µm at a measurement wavelength of 532 nm. (b) Magnified image of inset (i) where the PSF has high field position-dependent aberration levels. (c) Magnified image of inset (ii) where the PSF mainly suffers from isoplanatic aberrations.

in Si with an etch depth of 90 nm. The top layer gratings are lithographically made in a resist layer with a thickness of 90 nm. The square overlapping gratings have a size of either 5 µm, 8 µm or 10 µm and have a programmed overlay bias d of 20 nm.

A raw amplitude image of these overlay targets, retrieved from a single measured hologram without applying any lens aberration correction, is shown in Fig. 3.6 (a). In this image, overlay targets with sizes of 10 µm, 16 µm and 20 µm and varying pitches in the range of 400 nm to 900 nm are shown.

Fig. 3.6 is measured at a wavelength of λ = 532 nm and a bandwidth $\Delta\lambda$ = 1 nm. The aberrations are relatively low in the centre of the FoV. The 4D aberrations increase as one moves further towards the edges of the FoV. In particular, the small 10 × 10 µm^2 sized overlay targets are significantly affected by the field position-dependent lens aberrations. After correcting the field position-dependent aberrations we obtain the retrieved amplitude images presented in Fig. 3.6 (b). Notably, for the overlay targets with a large pitch (pitch: 700, 800, and 900 nm) relative to the measurement wavelength of 532 nm, the second diffraction order is captured by the imaging lens as well. This results in an interference pattern between the first and second diffraction orders on top of the homogeneous amplitude distribution of the first diffraction order. Fig. 3.6 (d) shows the vertical cross-sections of magnified insets (i) and (ii) of Fig. 3.6 (c). By comparing the uncorrected normalized amplitude (black) and aberration-corrected normalized amplitude (red) with the unaberrated simulated normalized amplitude (blue), it can be concluded that the aberration correction defines the target area more as a homogeneous square amplitude. Nevertheless, after aberration correction, there is still a deviation left with respect to the unaberrated simulated targets. The root cause of the residual error is discussed in the following section.

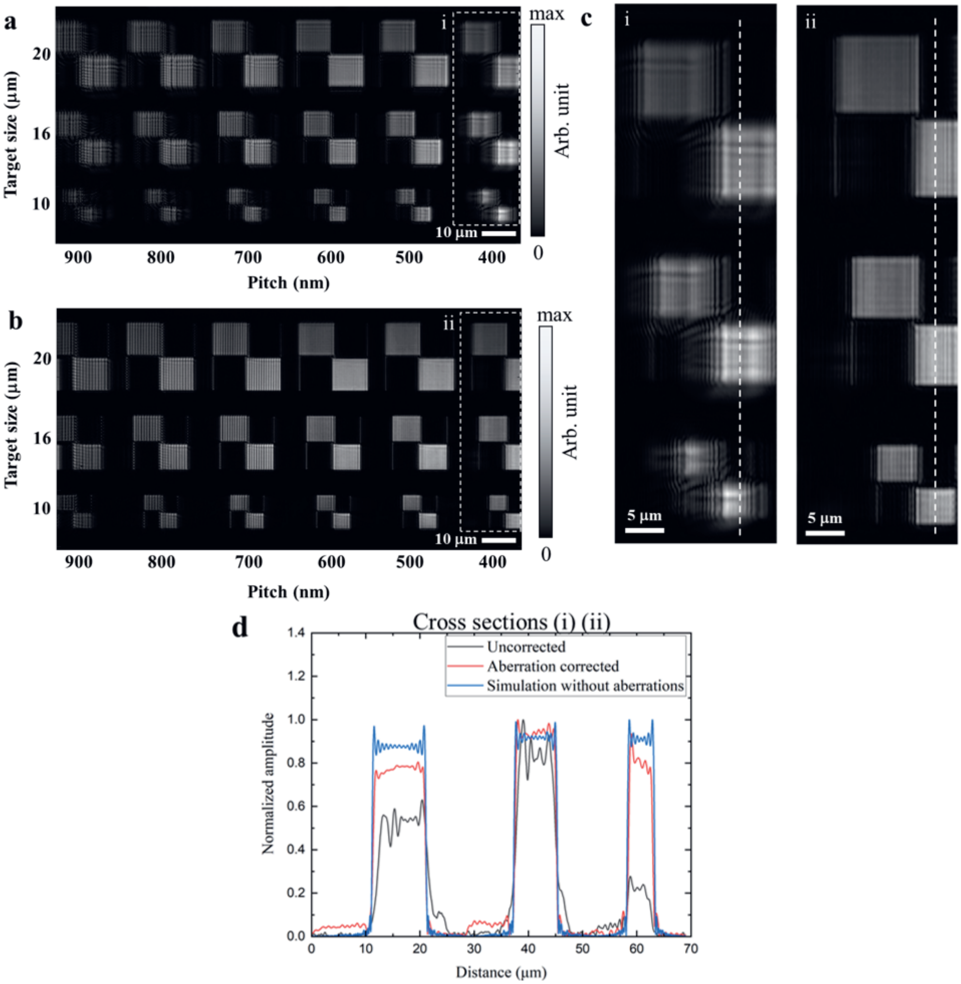

Figure 3.6: Experimental results of the aberration correction method for the VIS wavelength regime. (a) Retrieved amplitude image from a measured hologram of biased overlay gratings with sizes of 10 µm, 16 µm and 20 µm and varying pitches in the range of 400 nm to 900 nm. No lens-aberration correction has been applied to this image. The measurement has been performed at wavelength of λ = 532 nm and a bandwidth $\Delta\lambda$ = 1 nm over a FoV of 140 × 100 µm^2. (b) Field-position-dependent aberration corrected retrieved amplitude image from a measured hologram of biased overlay gratings. (c) Magnified image of the aberrated 400 nm pitch targets, inset (i) and magnified image of the aberration corrected 400 nm pitch targets, inset (ii). (d) Cross sections of the aberrated targets (c) (i), aberration corrected targets (c) (ii) and simulated targets without any aberrations.

3.3.3 Potential limitations

As presented in the previous section, residual aberrations remained after applying the aberration correction scheme. The wavefront error primarily results in the broadening of the PSF, which reduces its peak intensity. The quality of optical image formation can be properly quantified using the Strehl ratio S, originally introduced in astronomy by Karl Strehl [50]. The Strehl ratio is defined as the ratio of the peak intensity in the aberrated PSF to the peak intensity of a diffraction limited PSF [51]

$$S = \frac{I_{\text{PSF, measured}}}{I_{\text{PSF, diffraction-limited}}}, \tag{3.13}$$

where I_{PSF} is the maximum intensity of the PSF. A perfectly unaberrated optical system results in a Strehl ratio of 1.

To calculate the Strehl ratio of our df-DHM setup, we performed aberration correction on the nanohole calibration grid, as shown in Fig. 3.7.

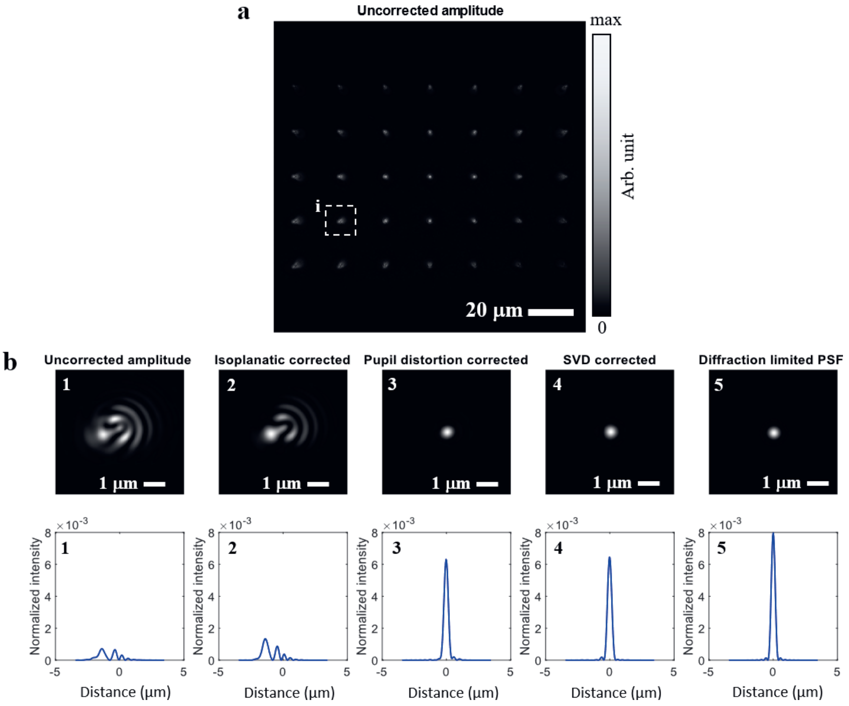

Figure 3.7: Non-isoplanatic aberration corrected PSF amplitude images measured at a wavelength of 532 nm compared to a simulated diffraction limited PSF. (a) Uncorrected amplitude image of nanohole calibration grid over the entire FoV. (b) Magnified amplitude image of inset (i) from (a). The columns from left to right decreases the aberration levels via the earlier described correction steps and their corresponding cross sections through the peak intensity (1-4). Compared to the simulated diffraction limited PSF (5).

Fig. 3.7 (a) shows the uncorrected amplitude image of the nanohole calibration grid measured at a wavelength of 532 nm. We calculated the Strehl ratio of a PSF which suffers from field position-dependent aberration, as indicated by (i). A magnified image of this PSF after each correction step and its corresponding cross-section are presented in Fig. 3.7(b) (1-4). Fig. 3.7 (b) (5) shows the simulated diffraction limited PSF. The calculated corresponding Strehl ratios after each aberration correction step are listed in Table 3.1.

Table 3.1: Strehl ratio after each aberration correction step

Processing step	**Strehl ratio**
Uncorrected	0.094
Isoplanatic correction	0.169
Pupil distortion correction	0.792
SVD correction	0.810

After a full aberration correction procedure the Strehl ratio equals $S = 0.810$. The difference with a perfect Strehl ratio of 1 can be explained according to the following limitations of the aberration correction method:

1. **Sample surface roughness:** The SVD step mainly suffers from sample surface roughness. The roughness of the sample surface adds noise to the SVD method because the PSFs are measured on a calibration grid sample.
2. **Lens surface roughness:** Similar to the sample surface roughness, the lens surface roughness also adds noise to the aberration correction, resulting in an image that is not perfectly corrected.
3. **PSF cropping:** Sample surface and lens roughness broadens the PSF significantly. During the SVD correction step, every PSF is cropped around a certain radius. Cropping, in combination with roughness, introduces errors by truncating the PSF.
4. **Maximum SVD modes:** The number of used SVD modes to describe the field position-dependent PSFs involves a trade-off between processing time and accuracy. Therefore, limiting the number of SVD modes used contributes to the overall residual aberrations.

Even though the above-mentioned limitations contribute to a residual aberration in the aberration corrected image, a Strehl ratio $S \geq 0.8$ generally corresponds to the diffraction-limited performance of the imaging system [52].

3.3.4 Near-Infrared wavelength range

Continuous developments in the semiconductor industry have led to the use of new materials that are almost opaque at VIS wavelengths and become more transparent at NIR wavelengths. One example is Ruthenium in the direct metal etch-processing steps

[53]. Here, we demonstrate the aberration correction capabilities at a NIR wavelength. In Fig. 3.8, we present an aberration correction measurement on overlay targets using a wavelength of 1300 nm. Fig. 3.8 (a) shows the retrieved amplitude from a hologram measured at a wavelength of λ = 1300 nm with a bandwidth of $\Delta\lambda$ = 12 nm. The pitch of the upper two overlay targets is 900 nm and that in the bottom three targets is 760 nm. Moreover, there is a small dust particle visible underneath the top right overlay target. It is important to note the FoV of the NIR camera with the Sony IMX990 sensor is 4.5 times smaller than the FoV of the VIS camera with the 12 Mpixel CMOS image sensor. As a result, the field position-dependent aberrations in the NIR measurements are less significant at the edges of the FoV compared to the VIS measurements. Fig. 3.8 (b) shows the field position-dependent aberration-corrected retrieved amplitude. In particular, the highly aberrated overlay targets with a pitch of 760 nm (bottom row), of which the 1st

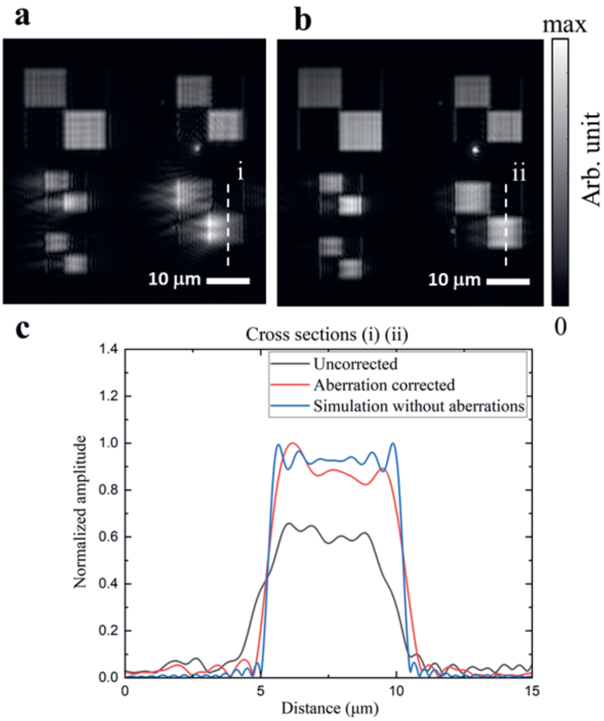

Figure 3.8: Experimental results of the aberration correction for the NIR wavelength regime. (a) A retrieved amplitude image of biased overlay targets with sizes of 10 µm, 16 µm and 20 µm and varying pitches of 900 nm (top two targets) and 760 nm (bottom three targets). No lens-aberration correction has been applied to this image. (b) A field-position-dependent aberration corrected retrieved amplitude image of the same biased overlay targets. The measurement has been performed with a wavelength of λ = 1300 nm and a bandwidth $\Delta\lambda$ = 12 nm. (c) Cross sections of the aberrated targets (a) (i), aberration corrected targets (b) (ii) and simulated targets without any aberrations.

diffraction order goes through the edge of image lens pupil, improve significantly after correction. Finally, in Fig. 3.8 (c), the cross section (i) and (ii) are compared to a simulated target without any aberrations. The cross sections show a significant improvement after aberration correction.

In this study, the experimental results at a measurement wavelength of 532 nm and 1300 nm are presented in detail. To demonstrate that this aberration correction method also has good performance between the two wavelengths, aberration correction was performed at wavelengths of 632 nm and 1064 nm. This results in the four Strehl ratios presented in Table 3.2, calculated for the PSFs at the edge of the FoV.

Table 3.2: Calculated Strehl ratio for different measurement wavelengths.

Wavelength (nm)	Strehl ratio
532	0.810
632	0.852
1064	0.756
1300	0.732

The highest Strehl ratio is achieved at a wavelength of 632 nm, which is closest to the objective design wavelength of 650 nm.

3.4 Conclusion

In conclusion, we demonstrated that in our df-DHM concept, where we retrieve the full complex field, we are able to correct the non-isoplanatic lens aberrations in a computationally efficient manner through the co-design of a dedicated imaging lens and a three-step algorithmic approach.

We first presented an uncoated 0.8-NA imaging lens that is designed to allow an optimal correction of the isoplanatic (field position-independent) aberrations and pupil distortion (linear coma) and minimizes the remaining non-isoplanatic aberrations such as field position-dependent astigmatism. Thereafter, we mathematically explained the three-step aberration correction procedure. Subsequently, we presented the experimental results of a calibration measurement in which non-isoplanatic lens aberrations are spatially probed using a grid of nanoholes, which act as point scatterers.

Next, using the measured aberration calibration, we demonstrated the correction capabilities of our three-step procedure in combination with the dedicated lens design. In the VIS regime at a wavelength of $\lambda = 532$ nm and a bandwidth $\Delta\lambda = 1$ nm the non-isoplanatic aberrations over a FoV of 140×100 μm^2 were corrected on several different overlay targets with various grating pitches. Additionally, we demonstrated the aberration correction capabilities of our df-DHM setup in the NIR regime at a wavelength of 1300 nm.

Therefore, using a custom-designed high-NA objective lens consisting of only two uncoated lens elements, we experimentally demonstrated these computational aberration correction methods over an extended wavelength range, proving the potential of df-DHM as a future wide-wavelength-range overlay metrology tool. Further studies on demonstrating and quantifying the benefits of overlay metrology over an extended wavelength range using the methods presented in this study and in Ref. [45] will be undertaken in the future.

CHAPTER 4

COMPUTATIONAL CORRECTION OF THE ILLUMINATIONS SPOT PROFILE

The spatially coherent illumination beam from a single-mode fiber in combination with the oblique illumination angle in our digital holographic microscopy concept, results in a non-uniform beam profile illuminating the overlay target. In this chapter, we explore the effects of this non-uniformity on overlay measurements. We experimentally demonstrate a calibration of this non-uniform beam profile using a large grating. We present a simple computational method to correct for this non-uniform illumination profile and we will show how this improves the robustness of the measured overlay for target position offsets

---

Published as: M. Adhikary, T. van Gardingen-Cromwijk, J. de Wit, S. Witte, J.F. de Boer and A. den Boef, *Illumination spot profile correction in digital holographic microscopy for overlay metrology*, J. Micro/Nanopattern. Maters. Metrol. **22**, 024001: 1-14 (2023)

4.1 Introduction

In the previous chapter, we demonstrated the image correction by calibrating and correcting aberrations in the imaging lens. Here, we continue to explore various computational enhancements to this digital holographic microscope (DHM) concept that would contribute to more precise and robust overlay measurements.

In this chapter, we explore the effects of a non-uniform illumination beam profile on the imaging of overlay targets and its effect on overlay measurements. In DHM, two oblique illumination beams are used that have an angle of approximately 70° relative to the normal of the grating plane. The imaging lens in our DHM setup has an NA of 0.8 which ensures that the 0^{th} diffraction order is not captured by this lens. These illumination beams generate a $+1^{\text{st}}$ order (coming from one illumination beam) and a -1^{st} order (coming from the other illumination beam). The intensities of the $+1^{\text{st}}$ and -1^{st} order beam are:

$$I_{+1} = I_{\text{ill}(+1)} \times \text{DE}\left(1 + \frac{K}{2} \times \text{OV}\right),\ I_{-1} = I_{\text{ill}(-1)} \times \text{DE}\left(1 - \frac{K}{2} \times \text{OV}\right), \tag{4.1}$$

where $I_{\text{ill}(+1)}$ and $I_{\text{ill}(-1)}$ are the illumination intensities of the two illuminations respectively, and DE is the diffraction efficiency of the grating stacks. Ideally, $I_{\text{ill}(+1)}$ and $I_{\text{ill}(-1)}$ need to be identical in both intensity level and profile, which can be challenging in experiments where 0.01% intensity difference should be measured. If we separately calibrate the individual illumination intensities for the two diffraction orders, then the corrected diffracted intensities from the targets $I_{\pm 1}^{\text{corr}} = I_{\pm 1} / I_{\text{ill}(\pm 1)}$ can be used to determine overlay that is independent of the individual intensities of the two arms.

In addition to correcting for the total intensity of each illumination beam, which can be done by deflecting part of the incident light with a beamsplitter into a photodiode, correction for the spatial intensity profile $I_{\text{ill}}(\vec{r})$, where $\vec{r}$ is the position vector, is also necessary to eliminate intensity variations within targets. While ideally, the targets would be illuminated by two top-hat uniform beam spots with the same intensity and polarization, it is usually difficult to achieve this in practice. Our DHM concept uses a spatially coherent near-collimated illumination beam from a single-mode fiber. This results in a Gaussian-like illumination beam profile on the wafer. However, a Gaussian illumination beam profile makes overlay metrology sensitive to target positioning errors. In this work, we first calibrate the beam profile of the Gaussian illumination beam by using a large diffraction grating and then use the calibrated profile to correct images of overlay targets to improve overlay accuracy and precision.

In the following sections, we will first present the results on the calibration of the illumination spot. Later we will show measurements on overlay targets and apply the calibrated spot profiles to correct the target images. We show that overlay values extracted from these measurements are clearly improved after the illumination beam spot is corrected, which demonstrates that our beam profile correction method improves the overlay metrology precision. We also show that consistent overlays can be measured when targets are placed at different relative locations of the illumination beam.

4.2 Illumination spot profile calibration

To measure the illumination beam spot $I_{\mathrm{ill}}(\vec{r})$ as incident on the overlay targets, we use a large grating as a calibration target. The size of the calibrating grating is much larger than the FoV of the imaging system and spot size. Since we are interested in calibrating a beam spot with an oblique incidence (approximately 70°), the pitch of the calibration grating is chosen in such a way so that with the chosen angle of incidence, the 1^{st} diffraction order from the grating is perpendicular to the grating surface. For these experiments, we use a commercially available grating from ThorLabs (GH13-18V - Visible Reflective Holographic Grating, 1800 lines/mm), which corresponds to a pitch size of 555.6 nm. For this pitch size, we choose a wavelength of 522 nm for the experiment, which is the wavelength at which the 1st order diffraction is normal to the grating surface when the angle of incidence is 70°. The first-order diffracted beams for both illumination arms are captured by the imaging lens and they transmit through the center of the exit pupil of the imaging lens, as shown in Fig. 4.1 (a).

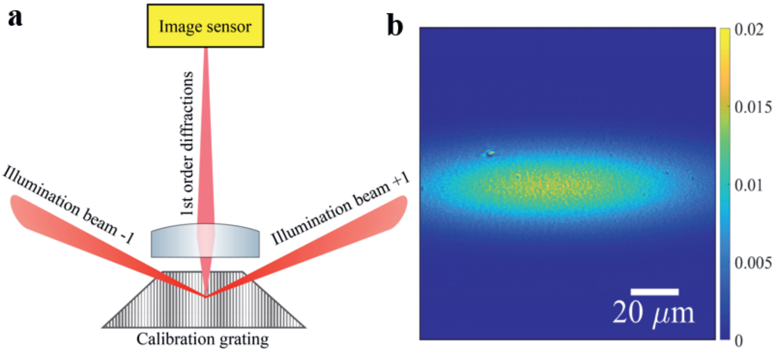

Figure 4.1: (a) A conceptual schematic of the illumination beam profile calibration for the DHM setup. The calibration target is a large grating that sends the 1^{st} order diffracted light to the image sensor through the middle of the imaging lens. The diffracted 1^{st} order beams from the two illumination beams coming from opposite directions are overlapped. (b) An intensity image on the camera of the overlapping $+1^{\mathrm{st}}$ and -1^{st} orders from the calibration grating produced by two oblique illumination beams from opposite directions.

The diffracted beams are then imaged on the sensor, as seen in Fig. 4.1 (a), which gives expected Gaussian-like beam profiles that are stretched along one direction due to the oblique incidence. In addition to the intensity profile, speckles are also observed that is caused by the optically rough surface of the calibration grating.

The imaged diffracted orders of the calibration grating are the calibrated intensity profiles of the illumination beams, which are overlapping in the FoV of the sensor. However, in our DHM concept, we can retrieve both complex illumination profiles on the grating using the parallel acquisition feature [54, 55]. Two overlapping digital holograms of the two illumination beams is created by coherently interfering the diffracted beams with their corresponding reference beams (Fig. 4.2 (a)). With a 2D Fast Fourier Transform (FFT), we digitally move to the pupil plane and obtain the baseband and the fully-separated sidebands containing the interference terms and their conjugates for both arms, as shown in Fig. 4.2 (b). In the pupil plane (i.e. each sideband of the frequency spectrum) a central amplitude peak is observed as expected for the diffraction orders. In addition, the whole NA of the lens is also filled with a background with homogenously distributed speckles, originating from the rough sample surface.

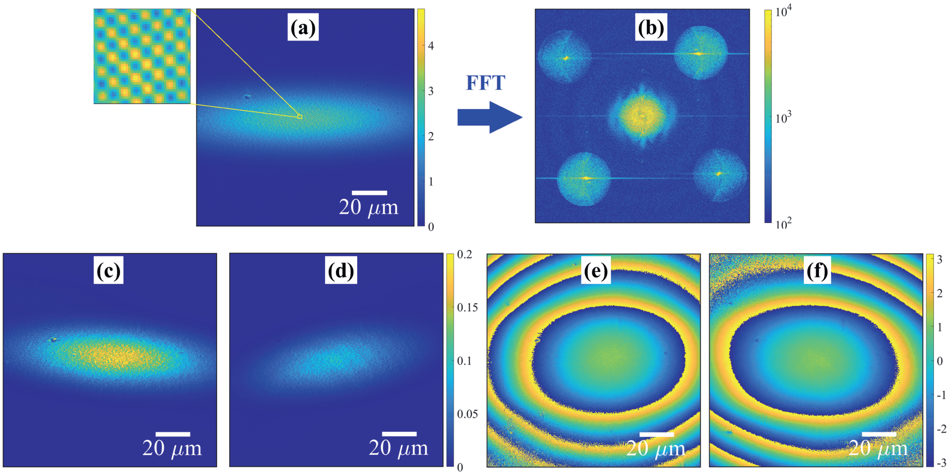

Figure 4.2: (a) Recorded overlapped holograms of the +1st and -1st orders of the beams diffracted by the calibration grating. The checkerboard pattern of the zoomed-in part of the digital hologram shows the two sets of interference fringes running in opposite directions diagonally. (b) The spatial frequency of the digital hologram after a 2D FFT, which includes the central baseband containing the DC terms and the sidebands containing the interference terms. (c,d) The reconstructed intensities and (e,f) 2π phases of the two diffraction orders from the calibration grating.

Next, with an inverse FFT of the sidebands, we reconstruct the complex field of the two illumination beams, $E^{\mathrm{ill}}_{+1}(\vec{r})$ and $E^{\mathrm{ill}}_{-1}(\vec{r})$ whose absolute values squared give the intensities (Fig. 4.2 (c,d)) and their arguments give their 2π wrapped phases (Fig. 4.2 (e,f)). Thus, we obtain the calibrated complex field of the illumination beam spot at a particular wavelength (in this case 522 nm). Note that the reconstructed intensities, plotted as the square of the absolute values of $E^{\mathrm{ill}}_{+1}(\vec{r})$ and $E^{\mathrm{ill}}_{-1}(\vec{r})$, are not the same. Later we show that this calibration step also helps to eliminate the effect of the intensity imbalance between the two arms on overlay measurements. It is to be noted that this is a one-time calibration step on a dedicated calibration target that can be placed on a fiducial plate inside the overlay metrology tool. For actual on-product overlay measurements, the same calibrated beam profiles would be used for correction.

4.3 Experimental results

4.3.1 Overlay target measurements

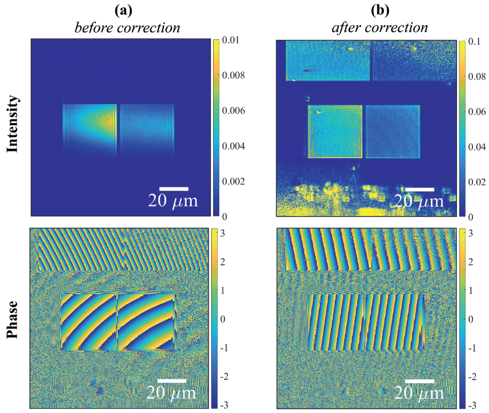

Figure 4.3: Reconstructed intensity (top) and 2π wrapped phase (bottom) of the +1 diffraction order for an overlay target pair (a) before and (b) after illumination spot correction.

After calibrating the complex illumination field, the calibration grating is replaced by a silicon test wafer containing pairs of overlay targets of size $38 \times 38\ \mu\text{m}^2$ with programmed overlay values in a range of -20 nm to 20 nm with a step size of 10 nm. Each target consists of two overlapping grating pairs with an overlay bias d of +20 nm and -20 nm. The overlay targets are measured in the DHM following the same procedure as the illumination beam measurement. Digital holograms of the +1$^{\text{st}}$ and -1$^{\text{st}}$ orders from the targets are recorded and the reconstructed amplitudes of the 9 sets of target pairs are shown in Fig. 4.4 (a). The illumination beam spot is clearly visible on the reconstructed intensity images of these large targets. The wrapped phase profile of the target pair shows curved 2π-wrapped phase jumps, implying the presence of a curved phase front. After this, the measured complex fields are corrected by dividing them by the pre-calibrated illumination spot as

$$E^{\text{obj}}_{+1(\text{corr})}(\vec{r}) = E^{\text{obj}}_{+1}(\vec{r})/E^{\text{ill}}_{+1}(\vec{r}), \text{ and } E^{\text{obj}}_{-1(\text{corr})}(\vec{r}) = E^{\text{obj}}_{-1}(\vec{r})/E^{\text{ill}}_{-1}(\vec{r}). \tag{4.2}$$

As seen in Fig. 4.3, the intensity gets significantly more uniform across each target after this correction step. Moreover, after correction, the 2π phase jumps run along straight lines indicating that the phase profile of the corrected target image is a tilted plane wave. This implies that the phase curvature before the correction step originates from the illumination optics, since the curvature gets eliminated in this correction process.

For both corrected and not corrected images of the overlay targets, the overlay values are calculated using the overlay equation presented in Chapter 1 (Eq. 1.11) with $d = 20$

nm. To calculate overlay, we use the mean intensity inside a region-of-interest (ROI) in each square, excluding the edges. The area of this ROI is kept constant for all targets for a fair comparison. The measured mean OVs as a function of the set OVs are plotted in Fig 4.4 (c). Before illumination spot correction, the overlay values are linear with the set values, with an offset of about 20 nm and a slope of 1.57. When the illumination correction is applied, the mean overlay values are much closer to the expected values with an offset of only 2.96 nm and the slope improves to 1.08. The overlay variations σ plotted in Fig. 4.4 (d) are derived from the pixel-to-pixel intensity variation in a target for two diffraction orders. Illumination spot correction significantly reduces this pixel-to-pixel overlay variation to a standard deviation that is less than 10 nm. The interesting part of this measurement is its robustness against the intensity imbalance between the two illuminations, as was seen in the reconstructed illumination intensities in Fig. 4.2 (c,d).

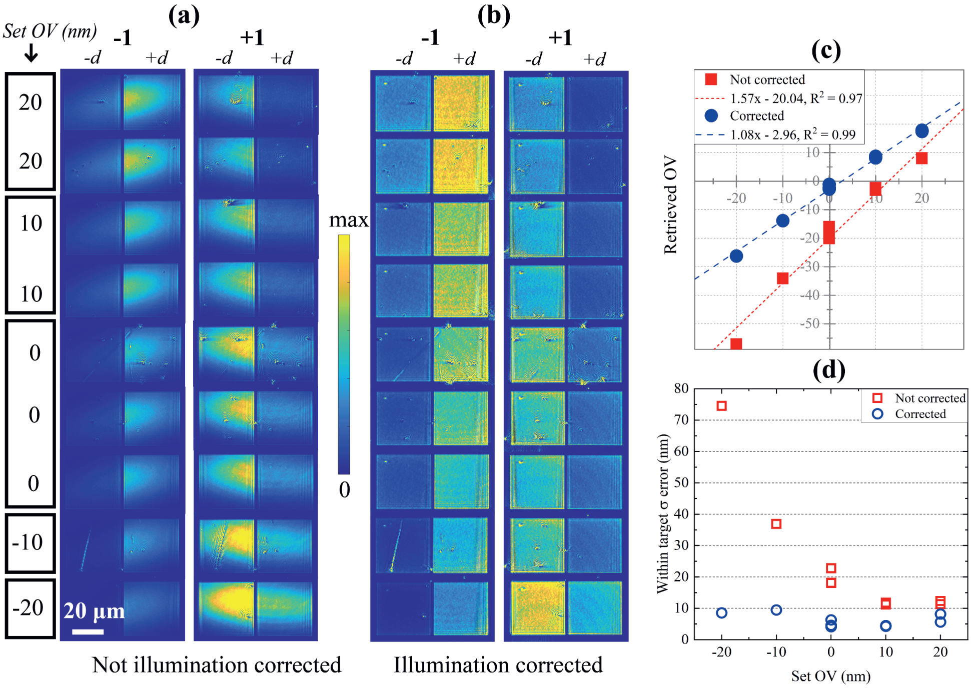

Not illumination corrected

Illumination corrected

Figure 4.4: The holographically reconstructed intensity images of the overlay target pairs for both diffraction orders (a) before and (b) after correction of the illumination spot, measured at wavelength 522 nm and bandwidth of a few nm. (c) The estimated mean overlay values estimated from uncorrected and corrected images as a function of programmed OVs. (d) Propagated σ error of the OVs derived from the pixel-to-pixel intensity variation in each target for two diffraction orders.

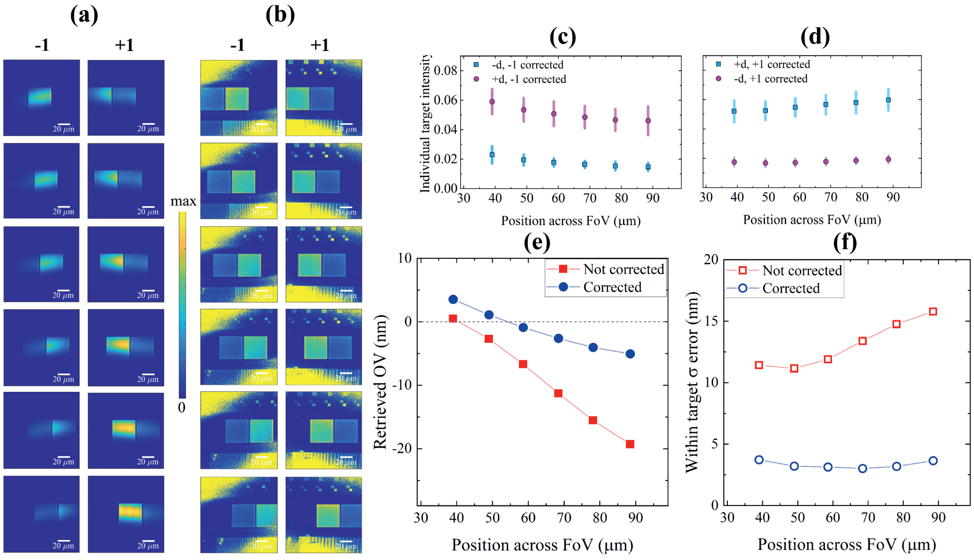

Figure 4.5: The -1st and +1st order reconstructed intensity images (a) before and (b) after illumination correction of a pair of overlay targets with programmed OV = 0 nm as the targets are moved across the camera FoV from left to right, measured at wavelength 522 nm and bandwidth of a few nm. (c,d) The mean corrected intensity of each individual target with their standard deviations as the error bars as a function of horizontal position on the FoV for -1st and +1st diffraction orders, respectively. (e) The extracted overlay values and (f) the σ errors propagated from the intensity errors in the targets as a function of position.

Another effect of the non-uniform illumination spot profile is the variation of the retrieve overlay value if the target position relative to the beam spot is changed. With illumination spot correction, we expect to eliminate this effect. Hence we check if we achieve more consistent overlay values for the same pair of targets at different relative locations within the illumination beam across the FoV. For this, we perform a measurement on one set of overlay set-get targets with set overlay of 0 nm by translating the targets across the FoV along the horizontal direction, while the illumination beams are kept constant. A total of 6 holographic images were captured by translating the stage with a step size of 10 µm. The reconstructed complex fields are corrected using the calibrated illumination field following the method discussed above. The -1st and +1st order reconstructed intensity images of the targets before and after correction of illumination spot are shown in Fig. 4.5 (a) and (b), respectively. The intensity profiles of the targets get significantly more uniform at all the measured locations after the correction steps. To quantify, the mean intensities of each target (+d and -d) for the -1$^{\text{st}}$ and +1$^{\text{st}}$ orders are plotted in Fig. 4.5 (c) and (d), respectively, as a function of FoV positions. The error bars on these data are the standard deviations of the intensities within each target. Slow linear intensity shifts with positive and negative slopes are observed for the +1st and -1st

Table 4.1: : OV parameters calculated from the position scan experiments

Wavelength	Coherence length	mean OV		standard deviation	
		uncorrected	corrected	uncorrected	corrected
522 nm	70 µm	-9.18 nm	-1.33 nm	7.59 nm	3.25 nm
632.8 nm	400 µm	-55.56 nm	3.97 nm	15.76 nm	0.75 nm

orders, respectively as a function of position. Next, the overlay values are calculated for each position of the targets and plotted as a function of position in Fig. 4.5 (e) for both uncorrected and corrected cases. Before illumination correction, the overlay values for the same pair of targets vary from 0 to -20 nm from left to right, with a steep slope with respect to position on the field, with relatively high standard deviations σ in the range of 11 nm to 16 nm, shown in Fig. 4.5 (f). After illumination correction, the overlay variation with field position is less, with overlay values +3 nm on the left and slowly decreasing to -6 nm on the right of the FoV. The overlay precision is significantly improved with σ being less than 4 nm at all locations. Although illumination correction improves the overlay precision, the values are not the same at all measured positions, which is undesired.

To explain the shift in overlay across FoV, we explore the possible reason behind this. The effect of field position-dependent amplitude variation in DHM has been explained by Cromwijk *et al.*[56]. According to this effect, when the source has limited monochromaticity with a bandwidth of several nm, the holographic imaging system's point spread function (PSF) changes from left to right on the FoV. This overall effect introduces an extra intensity imbalance on top of the intensity imbalance caused by the overlay, causing inaccuracy in overlay measurement when measured at different positions in the field. The illumination spot correction demonstrated here does not eliminate this effect. This effect and its correction will be discussed in more detail in Chapter 6.

4.3.2 Robust overlay against positioning errors

To check whether the shift in intensity with field position in our experiments is indeed caused by this effect, we perform another experiment by using a narrower bandwidth. For these measurements, we used a custom-made calibration grating with a pitch size of 692 nm for the illumination spot correction, which has much lower levels of surface roughness compared to the Thorlabs grating. The wavelength was set at 632.8 nm according to the availability of a narrow-pass filter for this wavelength and is closer to the calibration grating pitch. A laser-line interference filter is used to limit the bandwidth to only 1 nm resulting in a coherence length of about 400 µm, which is long enough compared to the OPD within the FoV. After calibration of the illumination spot for 1 nm bandwidth, the overlay targets are remounted in the setup and the experiments are repeated.

The holographic images of one set of targets with programmed OV = 0 are measured with 1 nm bandwidth at 632.8 nm center wavelength by moving them across the FoV

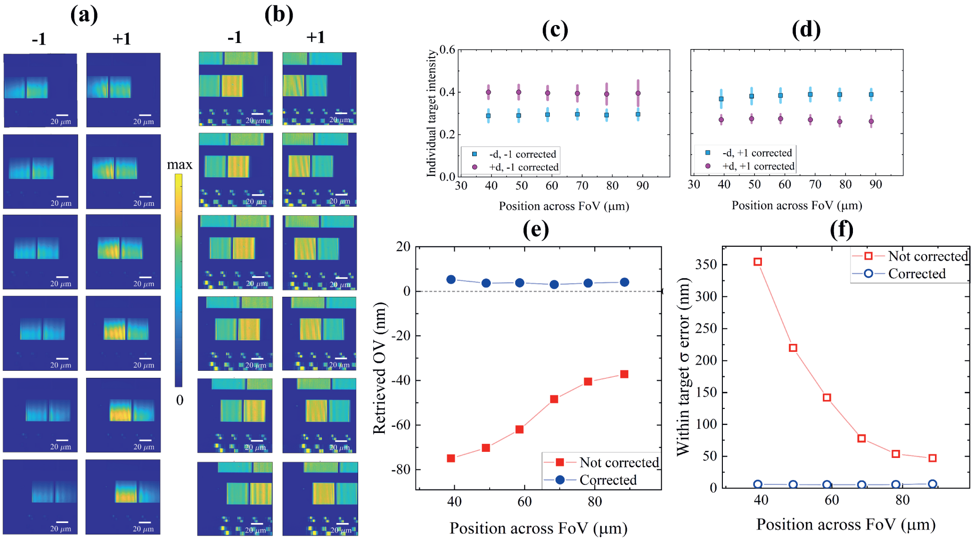

Figure 4.6: The -1st and +1st order reconstructed intensity images (a) before and (b) after illumination correction of a pair of overlay targets with programmed OV = 0 nm as the targets are moved across the camera FoV from left to right, measured at wavelength 632.8 nm and bandwidth of 1 nm. (c,d) The mean corrected intensity of each individual target with their standard deviations as the error bars as a function of horizontal position on the FoV for -1st and +1st diffraction orders, respectively. (e) The extracted overlay values and (f) the σ errors propagated from the intensity errors in the targets as a function of position.

along the horizontal axis. Fig. 4.6 (a) show the reconstructed intensities of the -1st and +1st orders of the overlay targets from the holograms at six different locations and Fig. 4.6 (b) shows intensity profiles after being divided by the calibrated illumination spot. The mean intensity and standard deviations of each target are extracted from the corrected intensities and plotted as a function of position in Fig. 4.6 (c,d). Compared to the position-dependent intensities in Fig. 4.5 (c,d), the corrected mean intensities here are more constant at every location, with σ error in each target within 7 nm, as seen in Fig. 4.6 (f). On the other hand, we observe large within target σ variations before correction, showing the usefulness of this method. This clearly translates to the calculated overlay values and their within target σ in Fig. 4.6 (e,f). In Table 4.1, we summarize the mean overlay and their standard deviations of all measured positions in the FoV for the two cases with different coherence lengths. The data show a clear improvement in overlay precision against target positioning error on the corrected data for the case of 400 μm bandwidth source. The overlay variation across a relatively large position variation of 50 μm in the FoV, given by the standard deviation of overlay values at each location is only 0.75 nm, as opposed to 3.25 nm for the case of 70 μm bandwidth source.

Next, The holographic images of the other overlay targets are also measured and the

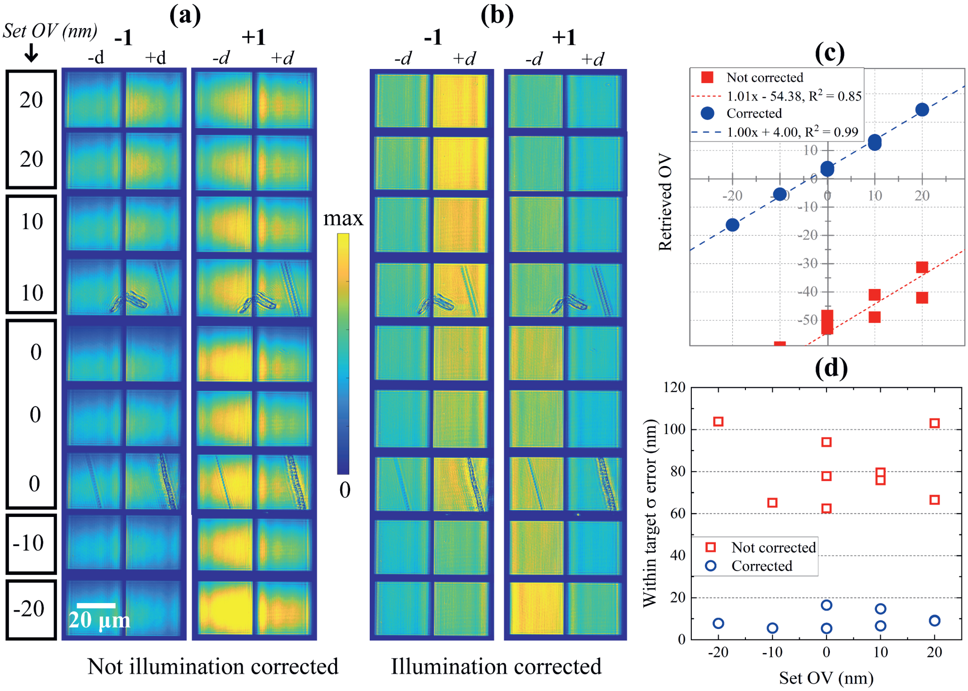

Figure 4.7: The holographically reconstructed intensity images of the overlay target pairs for both diffraction orders (a) before and (b) after correction of the illumination spot, measured at wavelength 632.8 nm and bandwidth of 1 nm. (c) The estimated mean overlay values estimated from uncorrected and corrected images as a function of programmed OVs. (d) Propagated σ error of the OVs from the intensity variation within each target.

uncorrected and corrected reconstructed intensity profiles are shown in Fig. 4.7 (a,b). Note that in this case the corrected intensity difference between the negatively biased ($-d$) and positively biased ($+d$) targets is lower than the case when a wavelength of 522 nm was used. This implies that the overlay sensitivity K is lower at 632.8 nm for these targets compared to that at 522 nm. Less sensitivity also implies that overlay measurements are more prone to mismatch between the two illumination beams in our DHM setup.

The overlay values and their errors within the target are estimated for both non-corrected and corrected cases and are plotted as a function of set OVs in Fig. 4.7(c,d). A good linear relation of the measured overlay values with the set values after correcting by the illumination spot as opposed to the uncorrected version indicates the effectiveness of this method. The overlay offset improves from -54 nm in the uncorrected case to +4 nm in the corrected case. These results indicate that with a sufficient coherence length of the source, consistent overlays can be estimated irrespective of the location of the targets with respect to the illumination beam spot.

The overlay offsets of a few nm after the correction could result from a small difference in the angles of incidence of the two illumination beams. Another effect is the polarization state of light used in the measurements. Linearly polarized light is used in the setup coupled into PM single-mode fibers. Although PM fibers are used, significant polarization crosstalk in such fibers can still be present. Thus, the polarization state after the fibers likely has elliptical components instead of being purely linearly polarized. The orientation of the linear polarization of the two illumination beams is assumed to be the same. Yet, a small difference in the angle of orientation can cause a difference in the diffraction efficiency in the -1st and +1st orders.

The larger pixel-to-pixel errors on overlay in the case of using 632.8 nm wavelength in Fig. 4.6 (f), 4.7 (d) as compared to 522 nm Fig. 4.4 (d), 4.5 (f) are primarily caused by a lower wavelength-dependent stack sensitivity. The targets' stack sensitivity is defined as a ratio of the intensity difference in the $-d$ and $+d$ targets, and their average intensity at $d = 20$ nm and 0 set overlay[57]. These values are between 0 and 1, with 0 being the intensity difference between the two targets having no sensitivity to overlay shift and 1 being the highest sensitivity. From the experimental data at 632.8 nm, the stack sensitivity is about 0.17, while the same targets have a higher stack sensitivity of about 0.51 when 522 nm wavelength was used. Lower sensitivity implies that overlay measurements are dependent on lower signal levels and hence more sensitive to imperfections in the measuring system.

4.4 Conclusion

The implementation of computational illumination spot correction significantly enhances the precision and robustness of overlay measurements in DHM. By carefully calibrating and correcting for non-uniform beam profiles, systematic errors originating from illumination intensity imbalances and target positioning inconsistencies are mitigated. Experimental results demonstrate substantial improvements in overlay accuracy and precision after applying these corrections. These findings show the value of computational techniques in optimizing DHM for advanced overlay metrology, laying the groundwork for addressing remaining imperfections through computational methodologies.

CHAPTER 5

COMPUTATIONAL VIBRATION MITIGATION USING PHASE INTERPOLATION

Digital holographic microscopy is an interferometric technique that is inherently sensitive to undesired phase variations between object and reference beam. These phase variations lower the fringe contrast if they are integrated over a finite exposure time which leads to a reduced amplitude of the retrieved image. This results in significant errors in applications that rely on a stable and accurate amplitude measurement, such as optical overlay metrology in the semiconductor industry. We present experimental results on a computational vibration mitigation method using phase interpolation between a sequence of measured holograms and demonstrate its capability to improve metrology precision in an overlay metrology application that uses digital holographic microscopy.

Published as: T. van Gardingen-Cromwijk, S. Konijnenberg, S. Witte, J.F. de Boer and A. den Boef, *Computational vibration mitigation using phase interpolation in digital holographic microscopy for overlay metrology*, Opt. Express **32**, 024001 (2023)

5.1 Introduction

Interferometry is a powerful technique that is used in a wide range of applications across various domains. By measuring the interference patterns of waves, interferometry enables precise measurements, imaging, and analysis in domains like astronomy [58], metrology [26], medical diagnostics [59] and optics manufacturing [60]. However, the accuracy of interferometry can be significantly degraded by undesired phase variations between the interfering beams due to, for example, mechanical vibrations. Vibrations during acquisition time in interferometry cause fringe washout [61], resulting in contrast loss which leads to an incorrect measurement result. Therefore, most interferometers are equipped with a system to damp or isolate the vibrations. Motorized equipment and cooling fans are removed from the system and even air turbulence is controlled [62]. The sensitivity of interferometers to vibrations is a fundamental challenge. However, in some metrology applications vibrations isolation is not feasible due to cost constraints or other system requirements. One example is optical overlay metrology where many overlay targets on a wafer need to be measured with an optical sensor while the wafer is moved at high velocities in a step-and-measure fashion in the shortest possible time. Under those demanding conditions, mechanical vibrations on the µm level between the optical sensor and the wafer are unavoidable [4]. Another vibration mitigation strategy is freezing in the motion using a higher acquisition frequency than the vibration frequency. Single shot DHM with a short acquisition time eliminates the challenge of vibrations in an interferometric system. However, in overlay metrology the overlapping gratings are thin, resulting in a low diffraction efficiency. Therefore, overlay measurements require an integration time on the order of milliseconds. This exposure time is too long to effectively freeze the vibrations resulting in fringe contrast loss. Since the retrieved overlay error in DBO is based on measured intensity values, fringe contrast loss due to vibrations directly degrade the precision of the measurement.

Since the 1960s, optical interferometry has been applied for whole-field, non-contact vibration measurement[63, 64]. For example, in Ref. [63, 64] holographic interferometry is used to visualize the amplitude of harmonic vibrations of an object by inspecting the contrast loss that occurs in the holographic fringes. However, so far phase-based vibration measurements have never been used to computationally correct for the fringe contrast loss due to these vibrations.

One interferometric technique that is highly robust against vibrations and air turbulence is known as "Dynamic Interferometry" [65–67]. In this approach, the two interfering beams are orthogonally polarized and an image sensor with a pixelated wire grid polarizer creates four interleaved interferograms with 90 degree phase steps. From these four interferograms, the phase difference between the interfering beams can be retrieved from a single camera acquisition which makes this techniques ideally suitable for testing large optics under regular atmospheric conditions [66]. However, our DHM-based overlay metrology method requires the parallel acquisition of two off-axis holograms [26], where each hologram of the metrology target is taken under different illumination settings. In that case it is not possible to use this Dynamic Interferometry technique to retrieve the images of the overlay metrology target.

In this work, we present a method based on high-speed digital holography for correcting fringe contrast loss due to vibrations and other sources like air turbulence. This is done by measuring a sequence of digital holograms with a high-speed camera in order to track the vibration of the object as a function of the time. The phase change between two exposures is interpolated in order to calculate the expected contrast loss per hologram. In the next section, we will first present the theory of our vibration mitigation method using phase interpolation. In section 5.3, we describe the Michelson interferometer setup, which is used to verify the method conceptually. Thereafter, we will present experimental results obtained. We conclude the paper by presenting an improvement in overlay precision using our phase-based vibration mitigation method and its potential future improvements.

5.2 Theory

5.2.1 Vibrations in digital holographic microscopy

Digital holographic microscopy (DHM) is an interferometric technique that is sensitive to undesired phase variations. These vibrations appear as phase variations between the object and reference beam in the interference signal on the detector. The instantaneous intensity as function of time and at position $\vec{r}$ is given by

$$I(\vec{r},t) = |O(\vec{r})|^2 + |R(\vec{r})|^2 + O(\vec{r})R^*(\vec{r})\exp[i\phi(t)] + O^*(\vec{r})R(\vec{r})\exp[-i\phi(t)], \tag{5.1}$$

where $\phi(t)$ indicates the phase variations due to undesired vibrations. The image sensor integrates this intensity, Eq. 5.1, over an acquisition time T resulting in a sampled mean intensity at time instant t_k given by

$$I_k(\vec{r}) = \frac{1}{T}\int_{t_k-T/2}^{t_k+T/2} I(\vec{r},t)dt. \tag{5.2}$$

We assume that the object and reference fields, O and R respectively, are time-invariant so the detected hologram at time t_k is given by

$$I_k(\vec{r}) = |O|^2 + |R|^2 + OR^*C_k + O^*RC_k^*, \tag{5.3}$$

where C_k is a complex-valued contrast parameter that describes the contrast loss due to the phase variation $\phi(t)$ given by

$$C_k = \frac{1}{T}\int_{t_k-T/2}^{t_k+T/2} \exp[i\phi(t)]dt, \tag{5.4}$$

where $\phi(t)$ includes all phase variations between the object and reference beams like mechanical vibrations and air turbulence. In DHM, the relevant amplitude and phase is given in the cross-correlation term OR^*C_k and its complex conjugate as described in

Eq. 5.3. Therefore, one cross-correlation term is filtered in the pupil plane using Fourier transform techniques, given by

$$F_k(\vec{r}) = OR^* C_k. \tag{5.5}$$

In this work, we aim to reconstruct the phase $\phi(t)$ from a sequence of complex-valued holograms I_k. The phase profile $\phi(t)$ can only be reconstructed if the time dynamics of the sample and the variability of the phase disturbances are much slower than the acquisition rate of the camera. Therefore, this method is limited to application which meet these requirements. The sampling frequency for this method to work must be twice the highest vibration frequency, according to Nyquist sampling theory [68]. However, a positive phase change results in the same contrast loss as a negative phase change. So the contrast loss oscillates with a frequency that is twice the vibration frequency. Therefore, to distinguish between the sign of the phase gradient the frame rate should be at least 4 times the sampling of the system. For the 1000 frames per second camera used in this study, the upper limit of the vibration frequency is 250 Hz. After reconstruction of the measured phase $\phi(t)$, the vibration-induced fringe contrast reduction can be calculated and compensated for computationally.

5.2.2 Phase-interpolated correction

A high frame-rate camera is used to acquire a sequence of holograms. Each hologram yields a retrieved phase, as illustrated in Fig. 5.1 with the black dots. In order to retrieve the continuous phase variation over time $\phi(t)$, indicated with the red line, the phase should be interpolated between the measurement points. Therefore, the measured phase points are fitted resulting in the black dotted curve in Fig. 5.1. The phase fit $\phi_F(t)$ is used to calculate the contrast loss $C_{k,F}$ for each measurement point at t_k. Using Eq. 5.4 the contrast loss is given by

$$C_{k,F} = \frac{1}{T} \int_{t_k - T/2}^{t_k + T/2} \exp[i\phi_F(t)]dt. \tag{5.6}$$

The calculated contrast loss due to vibrations $C_{k,F}$ is then used to obtain a corrected signal I_{cor} from the measured signal I_k, Eq. 5.3 given by

$$I_{\text{cor}} = \frac{F_k}{C_{k,F}} = \frac{OR^* C_k}{C_{k,F}} \approx OR^*. \tag{5.7}$$

Eq. 5.7 shows that the correction step removes the phase fluctuations from the measured signal. Dependent on how well the actual phase can be matched by fitting the measured phase points, the correction method can be sufficiently good for time-invariant sample cases of interest.

5.2.3 Phase fitting method

The fitting method used in this work is Fourier coefficient fitting. In reality the vibrations of the phase are not completely random, but rather a combination of a few well defined

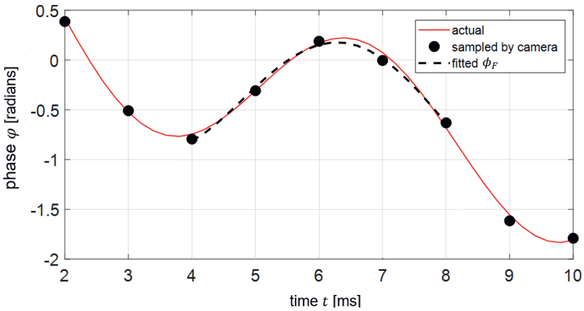

Figure 5.1: An illustration of the retrieved phase interpolation method, where the black dots indicate the phase values per measured hologram. The red line represents the actual phase fluctuation over time and the black dotted curve shows the a fit through five measurement points.

frequencies f_n. Therefore, the phase fluctuations $\phi(t)$ may be described with a limited set of complex-valued Fourier coefficients c_n

$$\phi(t) = \sum_{n=1}^{N} c_n \exp[i2\pi f_n t]. \tag{5.8}$$

Here, in Eq. 5.8, we fit a limited set of unknown coefficients c_n to the set of phase measurements via a standard least-square fitting method. The sensitivity of the frequencies f_n depends on the length of the measurement. In this method the input frequencies f_n are taken from the measurement frequency spectrum itself. Here, we assume that the frequency spectrum is discrete. The technique can fit the lower frequencies better once the measurement is taken over a longer period of time.

5.3 Method

In this section, we will present experimental setups that demonstrate the capabilities of our vibration mitigation technique. We will first verify the concept on a simple Michelson interferometer setup. Secondly, we will explain how the controlled vibrations are introduced in our off-axis DHM setup.

5.3.1 Michelson interferometer

Fig. 5.2 shows a schematic representation of the experimental setup that was built to test our vibration mitigation method. Light from a supercontinuum white light source (Leukos Rock 400) is filtered by an acoustic optical tunable filter (AOTF) tuning the desired wavelength. In this study, a wavelength of 632 nm with a bandwidth of 1 nm is used. The beam is divided into an illumination beam towards mirror 2 (M2) and reference beam towards mirror 3 using a 50:50 beamsplitter. Mirror 2 (M2) is placed under a small angle creating a dense fringe pattern that is similar to a fringe pattern in off-axis holography. A lens (L1) after the beamsplitter images the mirror surfaces on the high speed camera.

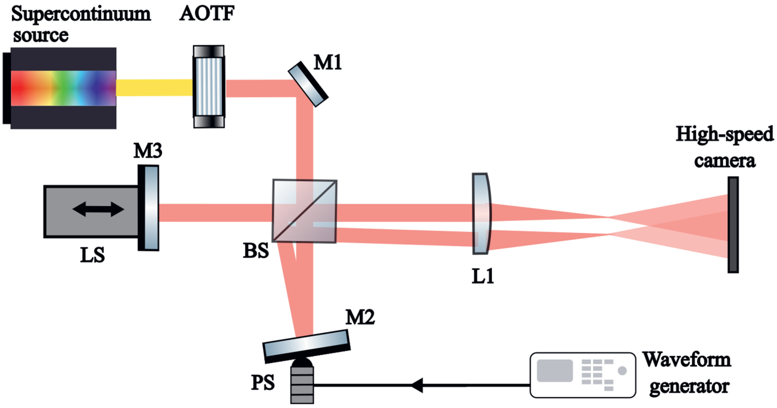

Figure 5.2: Schematic representation of the experimental setup for vibration mitigation in interferometry.

In this setup optical path lengths can be matched by moving mirror 3 (M3) using the linear stage (LS). Then, a vibration can be added to the system via the piezo electric stack attached to the back of mirror 2 (M2). This piezo electric stack (PS) in driven by a waveform generator letting mirror 2 (M2) vibration along the optical axis. The high-speed camera used in this setup is the HZ-2000-G-M from Emergent Vision Technologies (www.emergentvisiontec.com) with the Gpixel GSPRINT4502 CMOS image sensor having 2048 by 1216 pixels with a pixel size of 4.5 µm. The camera has a global shutter and can reach 1782 frames per second at 10-bit mode and 3462 frames per second at 8-bit mode. In this work, the camera is used at 1000 frames per second in 10-bit mode.

5.3.2 Digital Holographic microscopy

After verifying the concept using the Michelson interferometer, an overlay measurement is performed using our dark-field off-axis DHM on dedicated test targets. A schematic representation of the DHM setup is given in Fig. 5.3. The vibrations are introduced with the piezo electric stack vibrating against the $+1^{\text{st}}$ reference output fiber mount. Here, the same high-speed camera is used as presented in the Michelson interferometer setup (HZ-2000-G-M from Emergent Vision Technologies), section 5.3.1.

The phase per measured hologram will be presented as a single value. This single value is retrieved from a nine pixel average of the peak in the Fourier domain. If the sample vibrates laterally, then the fringe contrast loss depends on the local phase gradient. If we had a sample with a phase that varies randomly as function of position, the contrast loss would vary as function of position. However, because in overlay metrology we consider a

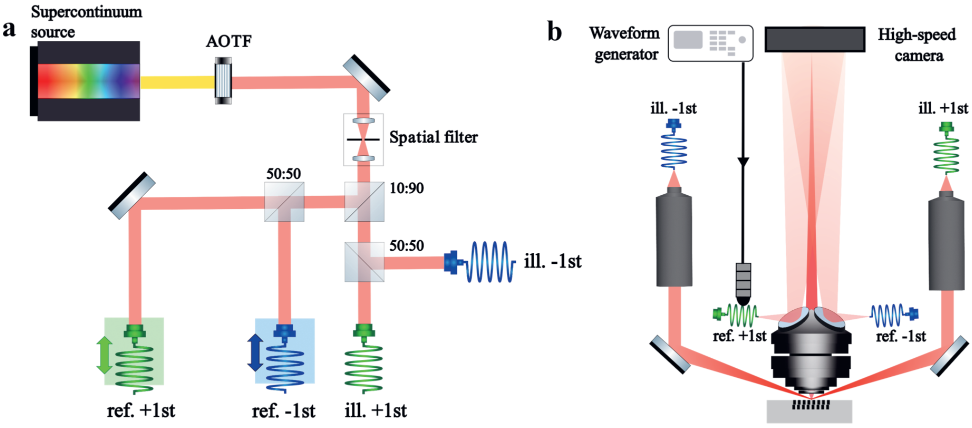

Figure 5.3: Schematic representation of the experimental setup for vibration mitigation in digital holographic microscopy.

target over which the phase gradient is constant, we can unambiguously assign a single phase shift and contrast loss per hologram.

5.4 Experimental results

The experimental results are obtained with a wavelength of 632 nm. The holograms are captured with a frame rate of 1000 frames per second and the exposure time equals 987 µs. The results presented in section 5.4.1 and 5.4.2 are obtained using the Michelson interferometer (section 5.3.1) setup and the results presented in section 5.4.3 are obtained using the off-axis DHM setup (section 5.3.2).

5.4.1 Single frequency

The piezo electric stack actuates the mirror vibration with an amplitude of 1 µm and a frequency of 140 Hz. The retrieved phase and amplitude variations as function of time due to the vibrations are presented in Fig 5.4 (a) and (b), respectively.

Phase fluctuations during acquisition time cause fringe washout, resulting in a decreased retrieved amplitude, as presented in Fig. 5.4. For the retrieved phase plot (a) a 1D Matlab phase unwrap function is used. As shown in Fig. 5.4, a large phase gradient at $t =$ 0.005, indicated with the red dotted line, results in almost 40% decreased amplitude. At the top of the sinusoidal vibration at $t = 0.007$ s, indicated with the blue dotted line, the phase gradient is zero resulting in a corresponding normalized retrieved amplitude of 1. For illustration purposes the minimum fringe contrast (at $t = 0.005$ s) and the maximum fringe contrast (at $t = 0.007$ s) are shown in Fig. 5.4(c). Once the actual phase variation during acquisition time is known, the corresponding amplitude loss can be calculated.

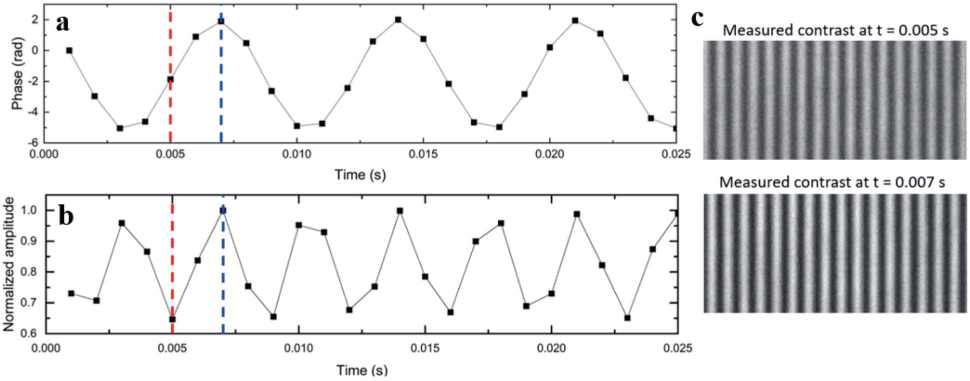

Figure 5.4: Retrieved phase (a) and amplitude (b) values due to 140 Hz 1 µm vibration of 15 holograms measured with 632 nm wavelength. (c) The contrast loss due to vibrations, with minimum contrast at t = 0.005 s (red dotted line) and maximum contrast at t = 0.007 s (blue dotted line). The camera frame rate is 1000 frames per second with an exposure time of 987 µs.

Therefore, a phase profile is fitted to the measurement points as described in section 5.2.3. The interpolated phase profile is plotted in red through the measured phase points as shown in Fig. 5.5.

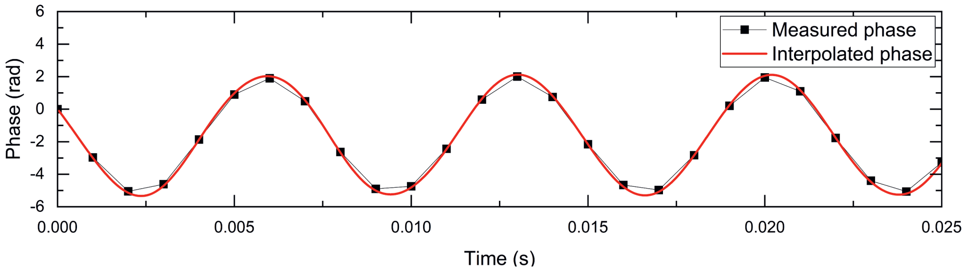

Figure 5.5: Phase measurement of an applied 140 Hz vibration as function of time indicated in black and the interpolated phase between measurement points indicated in red.

Integrating over the interpolated phase where the integration window equals the exposure time of 987 µs results in the calculated phase. Based on the calculated phase the predicted amplitude loss is calculated. Fig. 5.6 (a) shows the measured amplitude in black and the calculated amplitude based on the measured phase changes in red.

The corrected normal amplitude is then obtained by dividing the measured normalized amplitude (black curve) by the calculated normalized amplitude (red curve). The difference between the calculated amplitude and the measured amplitude is shown in Fig. 5.6 (b).

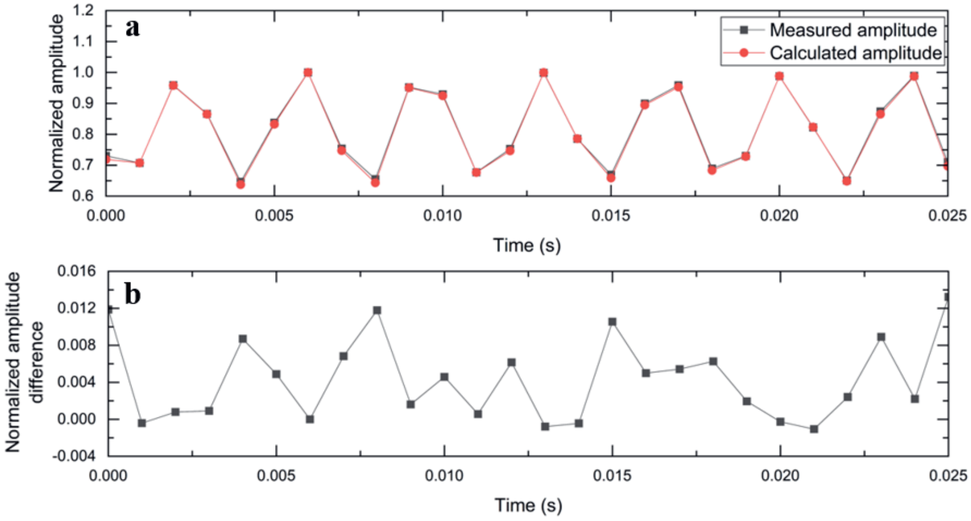

Figure 5.6: (a) Amplitude loss due to an applied vibration of 140 Hz as function of time indicated in black and its corresponding calculated amplitude indicated in red. (b) The difference between the calculated amplitude and the measured amplitude.

5.4.2 Multiple frequencies

By applying an arbitrary waveform to the piezo stack a combination of vibration frequencies can be measured. Here, the frequencies 20, 60 and 140 Hz are combined with an amplitude of 1 μm. The same analysis as presented in the previous subsection is applied to the measurement data. The measured phase as function of time is shown in Fig. 5.7.

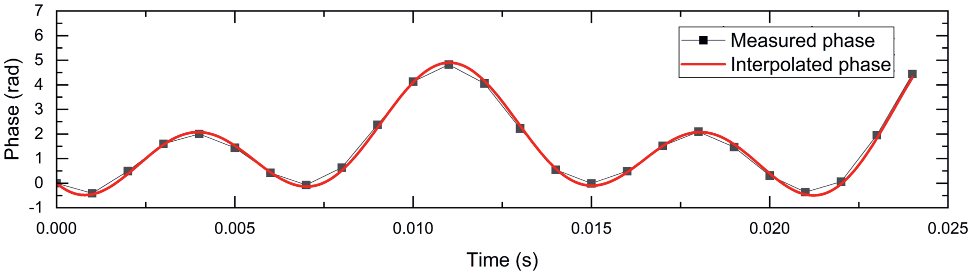

Figure 5.7: A phase measurement of a combined 20, 60 and 140 Hz vibration as function of time indicated in black and the interpolated phase in red.

Based on the phase profile presented in Fig. 5.7 the normalized amplitude loss is calculated and shown in Fig. 5.8 (a) (red curve). The difference between the calculated amplitude and the measured amplitude is shown in Fig. 5.8 (b).

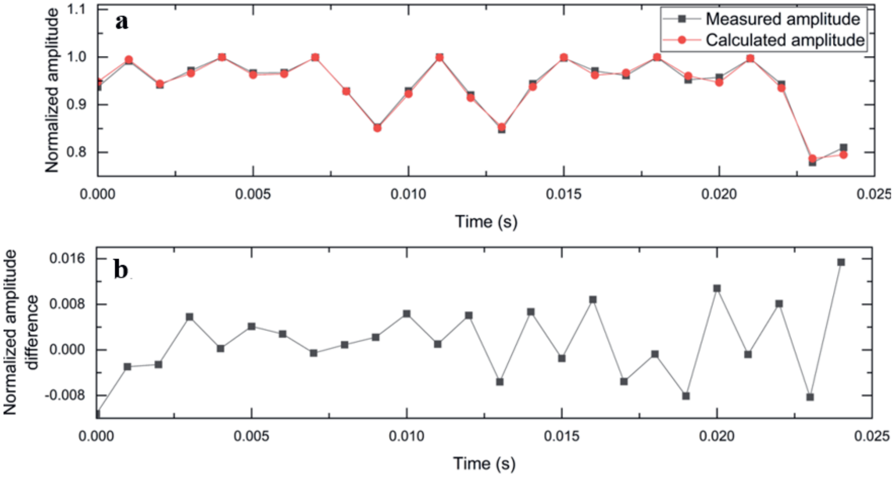

Figure 5.8: (a) Amplitude loss due to a combined vibration of 20, 60 and 140 Hz as function of time indicated in black and its corresponding calculated amplitude indicated in red. (b) The difference between the calculated amplitude and the measured amplitude.

5.4.3 Overlay measurement

The vibration mitigation method presented in the previous sections is here applied to an overlay measurement on dedicated overlay targets of 16 x 16 μm^2 with a grating pitch of 600 nm. 25 holograms were measured with 1000 FPS frame rate and 987 μs exposure time. In overlay metrology, the signal loss C_k (Eq. 5.4) due to phase variations becomes critical when it is different for the $+1^{\text{st}}$ and -1^{st} diffraction order. Therefore, DBO metrology is insensitive for only out-of-plane sample vibrations because it results in the equal contrast loss for the $+1^{\text{st}}$ and -1^{st} diffraction order. However, a combination of out-of-plane and in-plane vibrations results in a different fringe contrast loss for the $+1^{\text{st}}$ and -1^{st} diffraction order. This results in a relative intensity difference between the diffraction order which directly leads to incorrectly retrieved overlay values. Therefore in this experiments, the piezo electric stack vibrates only the $+1^{\text{st}}$ reference beam with 140 Hz. The overlay error in nanometers is calculated using Eq. 1.8 and presented in Fig. 5.9.

The black measurement points in Fig. 5.9 represent the measured overlay error without any vibration correction, resulting in a standard deviation of $\sigma = 7.9$ nm over 25 measurements. The red measurement points in Fig. 5.9 represent the measured overlay error with computational vibration correction using phase interpolation, resulting in a decreased standard deviation $\sigma = 0.8$ nm over 25 measurements. This computation vibration mitigation using phase interpolation results in a 10 times more precise overlay measurement in a vibrating environment. In overlay metrology, the precision in combination with tool induced errors form the overlay accuracy budget. Therefore, a lower overlay precision directly results in a more accurate overlay measurement. In our DHM setup, the standard

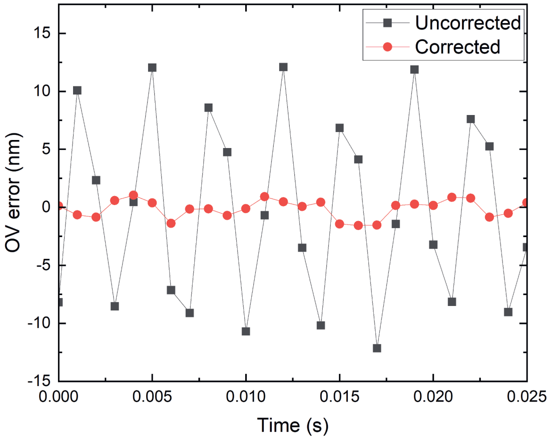

Figure 5.9: Overlay error as function of time with an applied 140 Hz vibration in the +1st reference beam. The black curve represents the uncorrected measurement and the red curve indicates the vibration corrected measurement.

deviation of 25 overlay measurements without any induced vibrations is also $\sigma = 0.8$ nm, which shows that our vibration mitigation method works down to the intrinsic noise floor of the current setup.

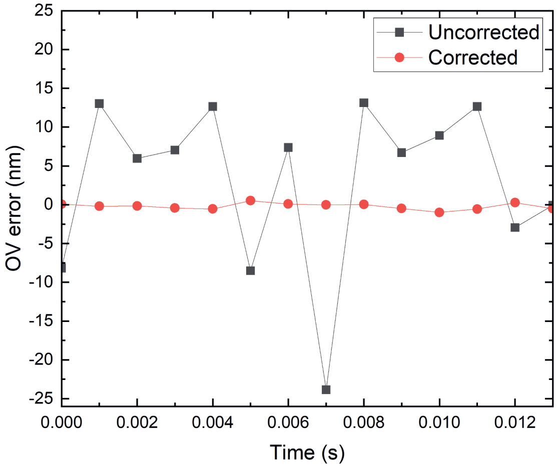

Figure 5.10: Overlay error as function of time with an applied non-sinusoidal vibration in the +1st reference beam. The black curve represents the uncorrected measurement and the red curve indicates the vibration corrected measurement.

To verify whether the proposed method also works under more random phase variations, we have applied a non-sinusoidal vibration to the DHM system at the frequency of 140 Hz. The overlay error in nanometers as function of time is presented in Fig. 5.10.

The black measurement points in Fig. 5.10 represent the measured overlay error without any vibration correction, resulting in a standard deviation of σ = 11.2 nm over 13 measurements. The red measurement points in Fig. 5.10 represent the measured overlay error with computational vibration correction using phase interpolation, resulting in a decreased standard deviation σ = 0.4 nm over 13 measurements. During this measurement the spot size was deliberately reduced resulting in more light on the overlay target. This results in a lower intrinsic noise floor of the system. Therefore, the standard deviation after correction σ = 0.4 nm is lower than the standard deviation after correction from previous overlay measurement (σ = 0.8 nm). In addition to accuracy, high throughput is a key indicator in overlay metrology. This phase interpolation method is not a limiting factor in DHM-based overlay metrology since it is just a 1D fit. The 2D FFT, which is always done in DHM-based overlay metrology, has the largest computational contribution.

5.4.4 Future improvements

As presented in the previous section, computational vibration mitigation using phase interpolation in DHM results in more precise overlay metrology. In order to further explore this technique, several potential future improvements are proposed in this section.

1. **Contrast loss due to coherence length** This phase interpolation method does not take into account contrast loss due to coherence length. Especially, for a relatively short coherence length of 100 μm, vibration with large amplitudes cause additional fringe washout due to the coherence function. Broadening the coherence function by using a smaller bandwidth could be a future improvement as discussed in Ref. [69].

2. **Small overlay targets** The presented method retrieves one phase value per measured hologram. This phase value is retrieved from the diffraction order peak in the Fourier spectrum. In case of a large grating, the diffraction order goes through one point in the pupil. However, the smaller the object is, the more the signal is spread over the pupil. In this case pupil field-position dependent phase fit is proposed. Here, every point in the pupil should have its own vibration correction factor.

3. **Sampling rate** As discussed in section 5.2 the sampling rate determines the upper limit of the vibration frequency which can be corrected for using this method. An improvement in the frame rate of high-speed camera technology in combination small pixels would benefit this method enormously.

4. **Time-variant samples** The phase interpolation method presented in this method is suitable for time-invariant samples. However, several DHM applications consider time-variant samples. Especially, for imaging biological samples this method is limited.

5. **Phase corrections** In our investigation we have demonstrated that our method can correct for vibration-induced amplitude loss. However, the contrast loss parameter C_k (Eq. 5.4) is complex-valued so vibration will also affect the retrieved phase. This can also be corrected with our method and can be a topic of future investigations.

5.5 Conclusion

In conclusion, we have demonstrated a computational vibration mitigation technique using phase interpolation in digital holographic microscopy. DHM is an interferometric technique that is inherently sensitive to undesired phase variations between object and reference beam. Therefore, phase variations during the acquisition time result in a reduced fringe contrast, which directly leads to erroneous signal level measurements in the retrieved images. In case of diffraction-based overlay (DBO) metrology this will lead to overlay errors. We showed experimental results that calculated the amplitude loss based on phase interpolation between measured phase points retrieved from a sequence holograms. Using the calculated amplitude reduction, the contrast loss due to vibrations was corrected per hologram.

In this study, we experimentally showed that the vibration correction resulted in a 10 times improvement in terms of overlay precision. This computational vibration mitigation concept proves to be a great improvement for interferometric measurements that have to operate in a vibrationally challenging environment as found in high productivity manufacturing environments.

CHAPTER 6

FIELD-POSITION DEPENDENT SPURIOUS APODIZATION

The main objective of this chapter is to present our understanding and findings on the spurious apodization effects we came across during our dark-field digital holographic microscopy research. The novelty comes with the use of quasi-monochromatic light in combination with a wavelength-dependent focal length of the high-NA imaging lens which leads to a significant field-position dependent pupil amplitude modulation. The field-position dependent apodization significantly affects the aberration-corrected point-spread-function. We will also present additional experimental data that supports our theoretical understanding. Finally, we will propose solutions that reduce this effect to acceptable levels.

Published as: T. van Gardingen-Cromwijk, M. Adhikary, C. Messinis, S. Konijnenberg, W. Coene, S. Witte, J.F. de Boer and A.J. den Boef, *Field-position dependent apodization in dark-field digital holographic microscopy for semiconductor metrology*, Opt. Express **31**, 411-425 (2023)

6.1 Introduction

Overlay metrology targets typically have dimensions of about 10 × 10 μm^2 and are often surrounded by other structures. Due to the finite imaging resolution of the optical sensor, optical crosstalk can occur where light from the surrounding structures leaks into the image of the metrology target. This effect can impact the quality of metrology and while apodization techniques can be used to minimize these errors, a near-perfect aberration-free imaging performance with a localized point-spread function (PSF) is required. In Chapter 3, we have already reported about the aberration-correction capabilities of our digital holographic microscopy (DHM) concept. In this chapter, we will show that in our DHM concept the finite bandwidth of our light source in combination with a wavelength-dependent focal length of our imaging lens introduces a field-position dependent spurious apodization that leads to a field-position dependent aberration-corrected PSF. A schematic presentation of the field-position dependent PSF that we observed with our DHM setup is shown in Fig. 6.1, demonstrating the importance of a well defined PSF.

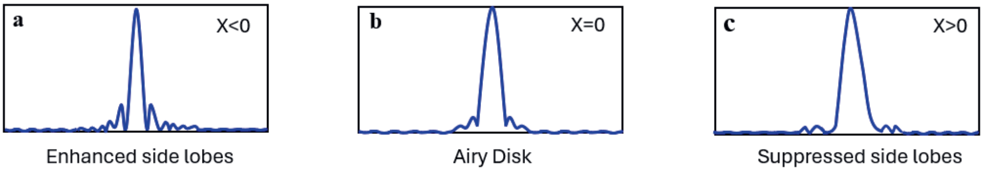

Figure 6.1: Schematic representation of a field-position dependent amplitude modulated point-spread function. (a) cross section of a PSF at left side of the field (X<0) where the side lobes are enhanced resulting in more crosstalk and a higher resolution (b) PSF that we observe in the center of the field (X=0). Here the PSF shape closely resembles an ideal Airy Disk. (c) cross section of an apodized PSF that we observe at the right side of the field (X>0) suppressing the high frequencies, resulting in less crosstalk and a lower resolution.

A gradual broadening of the central peak combined with a strong reduction of the side lobes is shown from Fig. 6.1 (a) towards Fig. 6.1 (c). In Fig. 6.1 (a), the PSF has a narrow central peak and strong side lobes. This yields excellent resolution but increased crosstalk levels. Moving from Fig. 6.1 (a) to (c) through the Field-of-View (FoV), one clearly observes a gradual broadening of the central peak combined with a strong reduction of the side lobes. For PSF (c) one would observe a lower resolution but a strong suppression of optical crosstalk. This observed behavior of a field-position dependent PSF is generally undesired since optical metrology applications usually require a localized PSF that is constant across the FoV.

In the next section, we present a simple model of the image formation in DHM using a quasi-monochromatic light source. For the sake of clarity we use some simplifications in our model. However, despite these simplifications, we can explain the observed field-position dependent PSF. Our analysis also shows that this observation is specific for dark-field DHM and will not be observed in regular dark-field microscopy. In section 6.3, we then present additional experimental data that clearly shows a good match between our model and the observed field-position dependent PSF. Moreover, in this section we will also show data that explains why a field-position dependency of the PSF can have so much impact on overlay metrology. We conclude the paper by presenting some solutions to reduce the field-position dependent apodization.

6.2 Theory

This section presents a simple model that shows that the observed field-position dependent apodization is a consequence of the coherent detection in DHM in combination with a quasi-monochromatic light source and wavelength-dependent focal length of the imaging lens.

In our df-DHM concept the object is illuminated under an oblique angle of incidence. Part of the diffracted light is captured by the imaging lens and coherently mixed with an off-axis reference beam in the image sensor plane. The intensity on the image sensor is obtained by integrating over the source spectrum, $S(\lambda)$

$$I = \int_0^{\infty} S(\lambda)|O+R|^2 d\lambda, \tag{6.1}$$

where O and R are, respectively, the complex amplitudes of the object beam and the reference beam in the image sensor plane. Since we only consider quasi-monochromatic light, it is convenient to split λ in a central wavelength λ_c and a small difference $\Delta\lambda$ that is much smaller than λ_c,

$$\lambda = \lambda_c + \Delta\lambda. \tag{6.2}$$

For our off-axis df-DHM concept we only consider, from Eq. 6.1, the term that contains the coherent coupling between the object field O and the complex conjugate reference beam R^* since the other three terms $|O|^2$, $|R|^2$ and O^*R are removed in the signal processing. This coherent coupling term yields a complex image A_i on the image sensor plane given by

$$A_i = \int_{-\infty}^{\infty} S(\Delta\lambda) O R^* d\Delta\lambda, \tag{6.3}$$

where OR^* is cross-correlation term that describe the interference between the object and reference beam. The integration over $\Delta\lambda$ extends from $-\infty$ to ∞ but it is to be understood that the source spectrum $S(\lambda)$ is narrow ($\Delta\lambda << \lambda_c$) which bounds the actual integration limits to a very narrow range. For simplicity we describe the reference beam in our off-axis df-DHM setup as an infinite plane wave with unit amplitude that is tilted in the x-direction,

$$R = \exp[-i(k_x x + \phi_r)]. \tag{6.4}$$

Fourier transforming A_i, Eq. 6.3, and centering the resulting spectrum around the origin yields a spatial frequency spectrum A_{EP} of the complex object image,

$$F\{A_i\} = A_{\mathrm{EP}} = \int_{-\infty}^{\infty} S(\Delta\lambda) F\{O\} \exp[i\phi_r] d\Delta\lambda. \tag{6.5}$$

The Fourier transform F of the object field O is the complex field E_{EP} in the exit pupil (EP) of the imaging lens. So Eq. 6.5 can be expressed as,

$$A_{\mathrm{EP}} = \int_{-\infty}^{\infty} S(\Delta\lambda) E_{\mathrm{EP}} \exp[i\phi_r] d\Delta\lambda. \tag{6.6}$$

The PSF is measured with the use of isolated nano-scatterers [47]. For simplicity we ignore a possible angle-dependent scattering profile and we assume that the scattered light generates a uniform unit amplitude $|E_{\mathrm{EP}}|$ in the exit pupil. Denoting the phase of E_{EP} by $-\phi_o$ yields

$$A_{\mathrm{EP}} = \int_{-\infty}^{\infty} S(\Delta\lambda) \exp[i(\phi_r - \phi_o)] d\Delta\lambda. \tag{6.7}$$

The phase term in Eq. 6.7 $\phi_{ro} = \phi_r - \phi_o$ depends on $\Delta\lambda$ for two reasons:

1. An Optical Path Difference (OPD) can exist between the object and reference beams on the camera. It has already been shown by Messinis et al. [69] that the OPD varies linearly within the FoV of an off-axis dark-field DHM.

   For narrow-band light ($\Delta\lambda << \lambda_c$) an OPD introduces a linear variation ϕ_{ro} with $\Delta\lambda$,

   $$\phi_{ro} = a_0 \Delta\lambda. \tag{6.8}$$

   In appendix A we will derive an expression for the scale factor a_0.

2. The focal length of the imaging lens in DHM is wavelength-dependent which leads to a radial variation of ϕ_{ro} in the exit pupil that also scales linearly with $\Delta\lambda$,

   $$\phi_{ro} = a_4 \Delta\lambda \sqrt{1 - \rho^2 \mathrm{NA}^2}, \tag{6.9}$$

   where ρ is the normalized radial position in the exit pupil and NA the numerical aperture of the imaging lens. In appendix B we will derive the expression for the scale factor a_4.

So the spatial frequency spectrum A_{EP} of the measured PSF can be written as a Fourier transform of the source spectrum,

$$A_{\mathrm{EP}}(\gamma) = \int_{-\infty}^{\infty} S(\Delta\lambda) \exp[i\gamma\Delta\lambda] d\Delta\lambda, \tag{6.10}$$

where γ is defined as,

$$\gamma = a_0 + a_4 \sqrt{1 - \rho^2 \mathrm{NA}^2}. \tag{6.11}$$

Assuming that the shape of the beam is a narrow-band Gaussian spectrum with a $\frac{1}{e}$ bandwidth of B nm yields

$$S(\Delta\lambda) = \exp\left[-\left(\frac{2\Delta\lambda}{B}\right)^2\right]. \tag{6.12}$$

The spatial frequency spectrum A_{EP} is then given by,

$$A_{\mathrm{EP}}(\gamma) = \int_{-\infty}^{\infty} \exp\left[-\left(\frac{2\Delta\lambda}{B}\right)^2\right] \exp[i\gamma\Delta\lambda]\, d\Delta\lambda. \tag{6.13}$$

Evaluating the integral from equation 6.13 yields,

$$A_{\mathrm{EP}}(\gamma) = \exp\left[-\left(\frac{B}{4}\right)^2 \gamma^2\right], \tag{6.14}$$

with γ as defined in Eq. 6.11. In terms of the normalized pupil plane coordinate ρ, the spatial frequency spectrum A_{EP} of the complex object image equals,

$$A_{\mathrm{EP}}(\rho) = \exp\left[-\left(\frac{B}{4}\right)^2 \left(a_0 + a_4\sqrt{1-\rho^2\mathrm{NA}^2}\right)^2\right]. \tag{6.15}$$

Note that the above spatial frequency spectrum is a result of interference between the object and the reference beams. As a result the amplitude variations in the exit pupil plane are not present in the physical pupil plane and this also explains why this effect will not be observed in regular dark-field imaging.

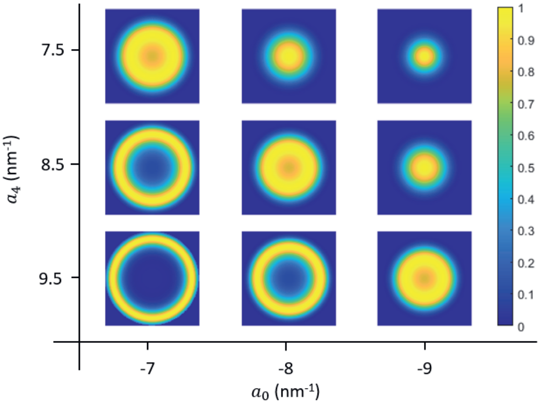

Figure 6.2: A_{EP}, Eq. 6.15, representing the normalized pupil plane as function of a_0 and a_4 for a bandwidth of B = 4 nm. Realistic values of a_0 and a_4 for our dark-field DHM setup are determined using Appendix A and B.

Some examples of pupil plane amplitude distributions A_{EP}, Eq. 6.15, for different values of linear dispersion a_0 and chromatic dispersion a_4 are given in Fig. 6.2.

6.3 Experimental results

In this section, we will present the experimental results of the field-position dependent apodization effect. Firstly, we will described the used imaging lens. Thereafter, the experimental results of the field-position dependent apodization using a point source are presented. In these experiments we will deliberately change the OPD in a controlled manner which allows us to validate the model that we presented in the previous section. Next, we compare the experimental data to the theoretical model presented in section 6.2. Finally, we present measured data to support an explanation why this field-position dependent apodization is so relevant for overlay metrology.

6.3.1 Imaging lens

The experimental data presented in this section is measured with our df-DHM on a breadboard setup as presented in Chapter 2 of this thesis. The custom made imaging lens, manufactured by Anteryon (www.anteryon.com), is a high-NA lens with NA = 0.8 consisting of two lens elements fabricated from a single glass type, where one lens is an aspherical lens, Fig. 6.3 (a). The lens is manufactured using a replication process [48, 49] and is fixed in a holder on which the reference beam mirrors are integrated in such a way that the angle between reference and object beam is optimized. The nominal focal length of the Anteryon lens at 650 nm wavelength is 7.3 mm. Since the two lens elements are made of the same material a significant wavelength-dependent focus will occur, Fig. 6.3 (b), even within the measurement bandwidth. The wavelength-dependent focus shift at a wavelength of 532 nm equals 0.7 μm/nm. To put this value in perspective, we can compare it with the Depth of Focus of this lens which equals roughly 0.8 μm at a wavelength of 532 nm.

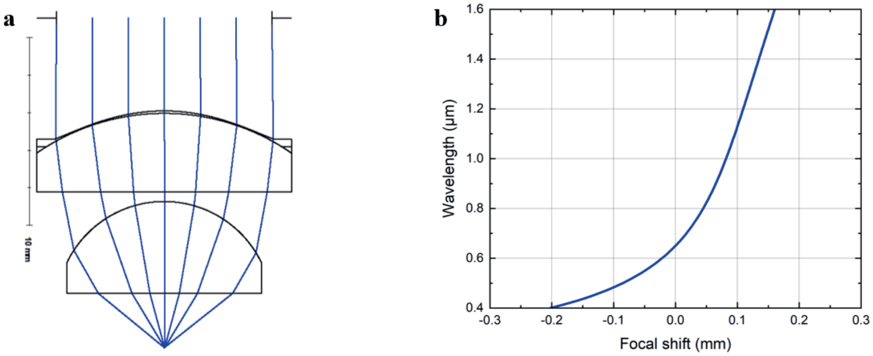

Figure 6.3: (a) A schematic representation of the two element high-NA lens. (b) The longitudinal focal shift as function of the wavelength.

6.3.2 Field-position dependent apodization

To experimentally demonstrate the field-position dependent spurious apodization, a point source illuminates the lens aperture with a spherical wave. This is done by placing a silicon sample with a nanohole on the target position in the df-DHM. The nanohole was manufactured using E-beam lithography resulting in a cylinder shaped hole with a diameter and depth of 100 nm. The nanohole is then illuminated at a wavelength of 532 nm. The diffracted spherical wavefront is captured by the lens and imaged on the camera. At camera level the diffracted light from the nanohole interferes with the coherent reference beam resulting in a digital hologram. Fourier transforming the camera image yields the spatial frequency spectrum of the hologram. This consists of a base band term and two side bands. These two side bands are, respectively, the complex field in the exit pupil and its twin image (complex conjugate and mirrored function). By taking the absolute value of one selected side band the amplitude A_{EP} in the pupil plane is obtained. As shown in Fig. 6.4, translating this nanohole point-scatterer across the FoV results in a change in amplitude distribution in the pupil plane. The light is homogeneously distributed for a point-scatterer in the center of the FoV. Whereas for the point-scatterer at the edges of the FoV the light is either centered in the pupil or spread towards the edge of the pupil as a result of change in OPD. The variation in amplitude distribution affects the PSF, which characterizes the imaging properties such as crosstalk and resolution as demonstrated in the introduction.

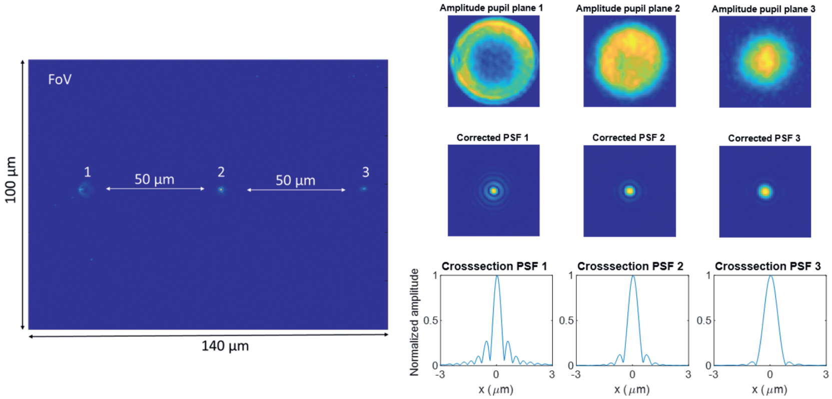

Figure 6.4: The field-position dependent amplitude distribution in the pupil plane, demonstrated by translating a point-scatterer through the FoV, from position 1 to 3. By imaging the PSF the effect on crosstalk and resolution is shown.

This effect is clearly visible in a cross section of the isoplanatic aberration-corrected PSF, shown in Fig. 6.4. Here the isoplanatic aberrations have been corrected using the method reported in reference [47]. For the point source positioned at the left edge of the FoV, the light is distributed towards the edge of the pupil resulting in enhancement of the side lobes of the PSF. Enhancing the higher spatial frequencies of the PSF increases the amount of crosstalk. Whereas for the point-scatterer at the right edge of the FoV, the light is distributed towards the center of the pupil and thereby suppresses the side lobes of the PSF (apodization). Suppressing the higher frequencies of the PSF results in less crosstalk from nearby structures. On the other hand, light filling the edges of the pupil and enhancing the side lobes results in a narrower center peak of the PSF, gaining resolution. In case of light centered in the pupil, the center peak of the PSF gets broader, which leads to a lower imaging resolution. So the position within the FoV creates a certain amount of OPD, leading to a phase shift which results in an amplitude variation.

The field-position dependent OPD shows how the amplitude distribution in the pupil plane affects the resolution of the imaging system and the crosstalk from nearby structures around an overlay target. In the next section, we will present the bandwidth dependency of this effect. Furthermore, we use the delay line in our df-DHM setup in such a way that we can control the amplitude distribution in the pupil plane.

6.3.3 Controlling the amplitude variations in the pupil plane

To further investigate the OPD dependent amplitude variations in the pupil plane, two wedges (Thorlabs BSF2550) are placed in the reference beam path before coupling the light into the optical fiber.. Translating one of these wedges allows us to precisely tune the OPD which changes the a_0 term that we defined in section 6.2. In addition, we investigated the bandwidth dependency. As explained in section 6.2, the amplitude variation is a coherent effect. The coherence length of a source is given by

$$L_c = \frac{2\ln 2}{\pi}\frac{\lambda_c^2}{B}, \tag{6.16}$$

where λ_c is the central wavelength and B the bandwidth [70]. The bandwidth of the light and thereby the coherence length L_c can be controlled either by a laserline filter of 1 nm (Thorlabs FL532-1) or by adjusting the bandwidth with the AOTF to 4 nm or 8 nm at 532 nm wavelength. In this section, we present experimental results on the bandwidth dependency of the amplitude variations in the pupil plane by controlling the OPD with wedges. Thereby we are adjusting the linear dispersion in the DHM which equals the a_0 term from Eq. 6.15.

From the center position of the wedge the OPD is changed by translating one wedge. In Fig. 6.5, the measured normalized amplitude distributions in the pupil plane are presented as function of bandwidth and OPD. The bandwidth has been varied between 1 nm, 4 nm and 8 nm. The OPD is in the range of 32 µm, which is of the order of magnitude as the coherence length for 8 nm bandwidth, $L_c(B = 8\text{ nm}) = 35$ µm.

Analyzing the 1 nm bandwidth case, it shows that in the center position of the wedge, at OPD = 0, the amplitude is homogeneously spread over the pupil plane. Adjusting the OPD to 16 µm the light is slightly more distributed towards the edge of the pupil. However, this effect is not significantly present at an OPD of 16 µm since it is well within the coherence length of 88 µm at 1 nm bandwidth. For the 4 nm bandwidth case, the effect is more significantly visible. The results clearly show that when the OPD is lower, the light gets distributed into the center of the pupil. Whereas for higher OPDs the light gets more distributed towards the edge of the lens pupil. The amplitude variations are

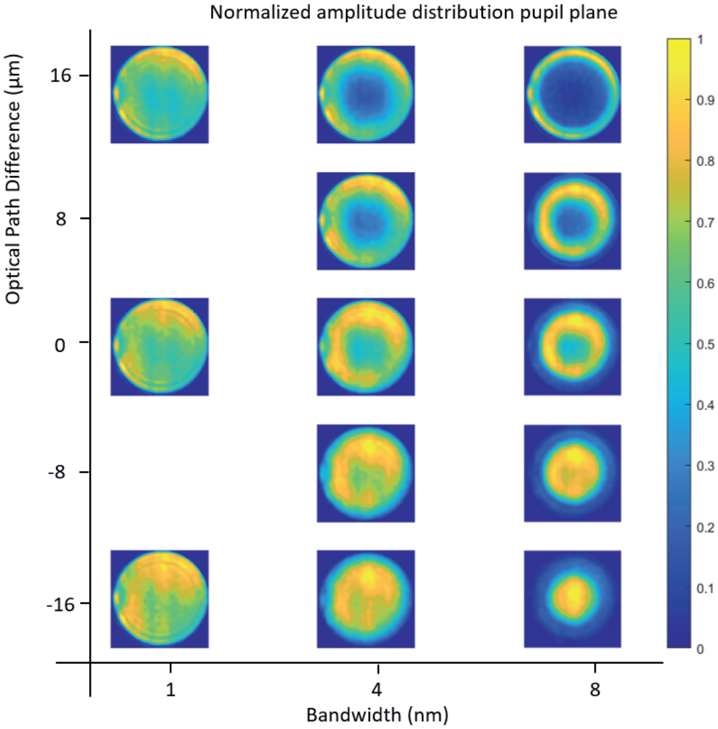

Figure 6.5: The measured normalized amplitude distributions in the pupil plane as function of bandwidth and OPD. Since the change in the amplitude distribution for the 1 nm case is very gradual, no measurements were taken for the OPD = 8 and OPD = -8 points.

most clearly visible for the 8 nm bandwidth sequence. Here the OPD shift of 32 µm is of the same order of magnitude as the coherence length, $L_c(B = 8\text{ nm}) = 35\ \mu\text{m}$. The larger the bandwidth, the more significant the OPD effect is. Moreover, for larger bandwidths, the amplitude distribution becomes donut-shaped when increasing the OPD. This shape is a result of chromatic dispersion, the a_4 term in Eq. 6.15, dominating the amplitude distribution.

6.3.4 Comparison of the theoretical model and the experimental data

To compare the experimental data presented in the previous section with the theoretical model from chapter 6.2, we simulated the expected amplitude distribution as function of bandwidth and OPD based on Eq. 6.15. The derivations of a_4 and a_0 are described in the Appendix A and B respectively. The results are presented in Fig. 6.6, where (a) shows the theoretical amplitude distributions, compared to the measured amplitude distributions in (b).

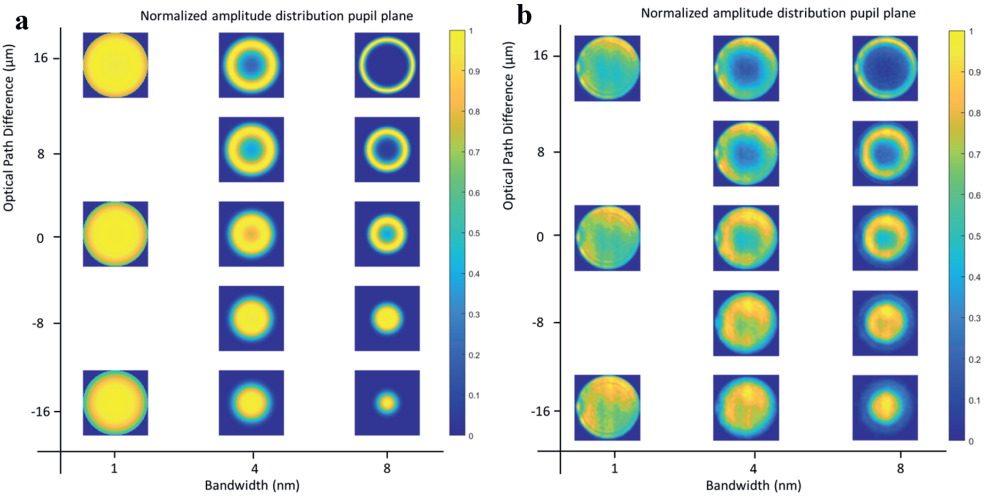

Figure 6.6: The measured normalized amplitude distributions in the pupil plane as function of bandwidth and OPD, where (a) shows the simulated distributions and (b) the measured distributions.

Fig. 6.6 clearly shows that the measurement results are in good agreement with the simple theoretical model for the three bandwidths. A closer inspection of Fig. 6.6 shows that there are still some deviations between our simple model and the experiments. These deviations can be explained by:

1. The theoretical model assumes that the point scatterer (nanohole) generates a flat amplitude distribution, as described by Eq. 6.7. However, this is not necessarily true. Any angle-dependent scattering profile from the nano-scatterers could cause a deviation between the theoretical model and the measurements.

2. In the model we assumed a Gaussian spectrum for simplicity reasons. But in practice the real spectrum may not have a Gaussian shape.

3. The bandwidth of the source is measured with a commercial spectrometer having a resolution of 2 nm, which results in some uncertainty in the measured value for the bandwidth used in the simulation.

4. Due to Fresnel reflection losses at the edges of the two lens elements in our high-NA lens, amplitude losses at the edges of the exit pupil are expected but not covered in the theoretical model.

The four reasons described above potentially explain the small mismatch between the experimental data and the theoretical model. To improve the model we could, for example, measure the spectrum and thereby its spectral shape and bandwidth more precisely. We will elaborate on this idea in Chapter 7 of this thesis.

6.3.5 Relevance for overlay metrology

After having demonstrated the field-position dependent apodization, we will now show why this is relevant for a metrology application like overlay metrology. The overlay error between two semiconductor layers is measured as an intensity difference between the $+1^{\text{st}}$ and -1^{st} diffraction orders that are diffracted by a small grating that is used as an overlay metrology target. These orders are generated by 2 beams that illuminate the target from opposite sides at an oblique angle. Using opposite illumination beams results in an OPD variation in the image field that runs in opposite directions for the $+1^{\text{st}}$ and -1^{st} order holograms on the camera. According to the theory presented in section 6.2, this results in a field-dependent spurious apodization that varies in opposite directions for the $+1^{\text{st}}$ and -1^{st} order images. This is clearly visible in Fig. 6.7 which shows the measured variation of the PSF for different field positions along the x-direction. These results were obtained at a wavelength of 532 nm and a bandwidth of 8 nm. For the sake of clarity we have also included the amplitude distribution in the exit pupil that we have obtained by back-propagating the measured PSFs.

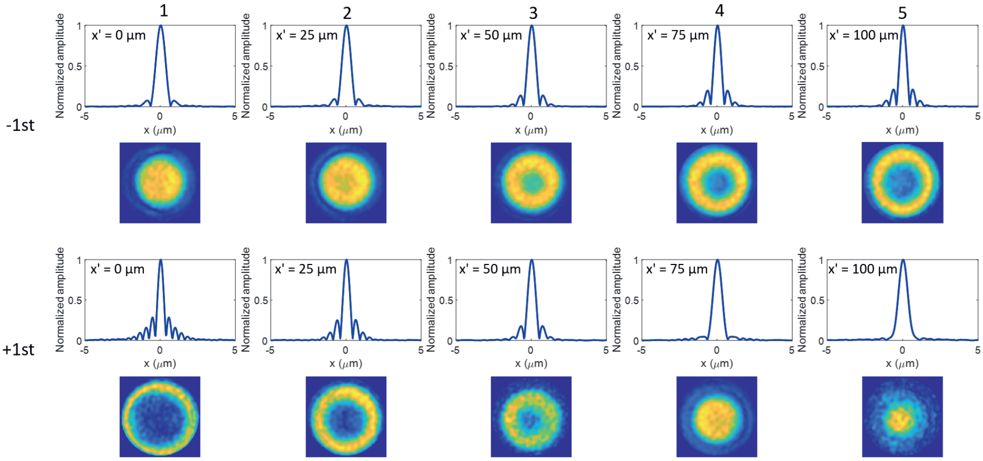

Figure 6.7: Measured PSF and pupil amplitude distribution as function of position in the field for the $+1^{\text{st}}$ and -1^{st} imaging branches in our df-DHM setup. These results were obtained at a wavelength of 532 nm and bandwidth of 8 nm.

In practice, overlay targets are often surrounded by patterns like device structures or other metrology targets. These patterns also diffract the incident illumination beam resulting in a dark-field image of these patterns alongside the dark-field image of the overlay target. Due to the finite resolution of the optical sensor, optical crosstalk from this adjacent pattern leaks into the image of the overlay target as schematically shown in Fig. 6.8.

This crosstalk will impact the measured signal level in the Region-Of-Interest (ROI) inside the metrology target. Due to the opposite PSF variation inside the image field this impact is different for the $+1^{\text{st}}$ and -1^{st} order images. This effect may seem small but

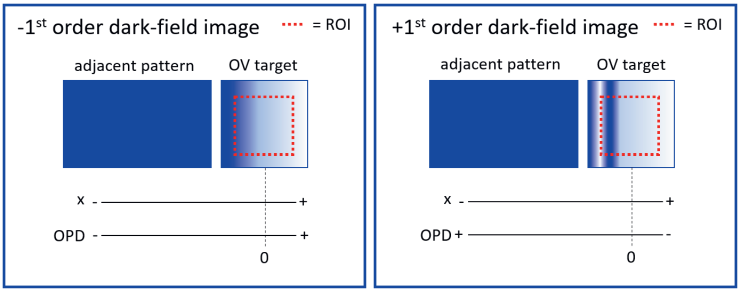

Figure 6.8: Cartoon drawing of the -1^{st} and $+1^{\text{st}}$ order images of the overlay target that is adjacent to an image of a neighboring structure. For clarity, the x-direction and the direction of the OPD are indicated, showing that the OPD runs in opposite directions for the -1^{st} and $+1^{\text{st}}$ order images. The -1^{st} and $+1^{\text{st}}$ order signal levels that are used for the overlay determination is given by the integrated signal levels in the Region-Of-Interest (ROI) that is marked by the red dotted square.

in order to achieve sub-nanometer overlay metrology precision one needs to measure intensity differences between the $+1^{\text{st}}$ and -1^{st} diffraction order with a relative precision of the order of 10^{-4} [26]. For these extreme measurement requirements, even small variations in the PSFs can significantly affect the actual overlay measurement. A proper understanding of the field-position dependency of the PSF and the possible solutions is therefore vital.

6.4 Proposed solutions

As presented in the previous section, the field-position dependent apodization affects the overlay metrology accuracy. In order to minimize this effect or correct for its impact on the image formation, several solutions are proposed in this section. To begin with three different hardware solutions:

1. **Achromatic design with additional lens elements:** In order to compensate for the strong wavelength-dependent focal length, one could add additional lens elements to (partially) correct for a wavelength-dependent focus variation. However, adding more lens elements leads to more light losses due to reflections at the glass-air interface. Since we intend to use our DHM over a very large wavelength range from visible to shortwave infrared we cannot use anti-reflection coatings [71]. It is therefore preferred to keep the number of lens elements to an absolute minimum. More lenses lead to more glass-air interfaces which leads to more light loss and therefore lower intensity levels.

2. **Low dispersion lens material:** Another approach would be to use lens material with lower dispersion, such as CaF_2 that has an Abbe number of $V_d = 94.99$. The field-position dependent apodization will then be minimized in this case. However, such a low dispersive material generally has a low refractive index. Realizing

a high-NA lens with only 2 CaF_2 lens elements would lead to an unrealistically high lens curvature.

3. **Narrow bandwidth:** In this paper we presented the bandwidth dependency of the amplitude variations, showing that the broader the bandwidth the stronger the field-position dependent amplitude variations. The use of a small bandwidth is a potential hardware solution to address these field-position dependent amplitude variations. However, for best possible performance, overlay metrology needs a light source with a tunable wavelength [72–74] so a supercontinuum source is often preferred. The consequence of reducing the bandwidth with such a source is a reduction in optical power which limits the capability to measure on weak overlay targets.

From the description above it is clear that all these hardware solutions have limitations and will lead to trade-offs in terms of available optical power or achievable wavelength range. Therefore, a desired optimal solution would logically be a software correction measure, where computational correction for the field-position dependent amplitude variations in the pupil plane can be applied.

Computational correction: A software solution could be based on existing field-position dependent aberration correction algorithms [44], as discussed in Chapter 3 of this thesis. A similar approach could be used for our case, since the coherent imaging regime of off-axis holography is likewise described in terms of a linear imaging system, but this the measured image field is obtained from the sideband of the hologram. The computational correction for field-position dependent apodization as addressed in our paper can be seen as a natural extension to the 4D-aberration correction approach as proposed in [44]. For that, the field-position dependent phase modulation due to the 4D-aberration function in the pupil plane will be extended with a field-position dependent amplitude modulation in the same pupil plane. This would allow a correction of the field-position dependent apodization without any hardware limitations.

6.5 Conclusion

In conclusion, we have demonstrated that in our df-DHM concept the finite bandwidth of the light source in combination with a wavelength-dependent focal length of the high-NA imaging lens leads to a significant field-position dependent spurious apodization that significantly affects the aberration-corrected PSF.

We have first presented field-position dependent measurements on PSFs to clarify the effect that pupil plane amplitude variations have on the crosstalk and resolution of the imaging system. Light distributed toward the edge of the pupil resulted in enhancement of the side lobes of the PSF, leading to more crosstalk and an increase in resolution. Whereas a centered amplitude distribution results in suppression of the side lobes, leading to crosstalk reduction and a lower resolution.

During the investigation we controlled the effect using wedges and thereby changing the linear dispersion in the imaging system. Moreover, we demonstrated our understanding of the observed field-position dependent apodization by comparing a simple theoretical model with experimental data. The expectations from the model matched our measurements properly with a small deviation presumably coming from the illumination spectrum not being perfectly Gaussian.

Thanks to this investigation we gained a deeper understanding of the phenomenon that impacts the image formation in our df-DHM concept. Based on our understanding and experiments we have presented an explanation why this effect is relevant for overlay metrology and we have proposed various solutions to mitigate this spurious apodization effect. We have come to the conclusion that a computational correction is the most preferred solution direction. A next step in this investigation will be to computationally correct for the amplitude variations in the pupil plane which brings us a step closer toward a df-DHM as a precise overlay metrology tool in semiconductor industry.

Appendix A. Derivation of linear dispersion a_0

The term a_0 represents the linear dispersion in our df-DHM setup. The linear dispersion originates from the delay line, the wedge and the field-position dependence. The optical path length (OPL) for, respectively, the object beam and the reference beam are given by,

$$\mathrm{OPL}_o = L_o, \tag{6.17}$$

$$\mathrm{OPL}_r = L_r + (n(\lambda) - 1)T_w, \tag{6.18}$$

where L_o and L_r are the path lengths for, respectively, the object beam and reference beam through air, T_w is the glass thickness of the tunable wedges and n is the wavelength-dependent refractive index of the wedges. The phase difference between the object and reference beam at camera level can now be described by the following equation,

$$\phi(\lambda) = \frac{2\pi}{\lambda}((n(\lambda) - 1)T_w + L_r - L_o). \tag{6.19}$$

Since we consider quasi monochromatic light with a central wavelength λ_c and a small wavelength variation $\Delta\lambda$ around the central wavelength: $\lambda = \lambda_c + \Delta$, we can approximate Eq. 6.19 by the following linearization,

$$\phi(\lambda_c + \Delta\lambda) = 2\pi\left(\frac{1}{\lambda_c} - \frac{\Delta\lambda}{\lambda_c^2}\right)\left[\left(n_c - 1 + \frac{dn}{d\lambda}\Delta\lambda\right)T_w + L_r - L_o\right], \tag{6.20}$$

where n_c is the refractive index for the central wavelength λ_c. Expanding Eq. 6.20 and defining the tunable OPD at the central wavelength as $\mathrm{OPD}_c = (n_c - 1)T_w + L_r - L_o$ yields,

$$\phi(\lambda_c + \Delta\lambda) = \frac{2\pi}{\lambda_c}\mathrm{OPD}_c - \frac{2\pi}{\lambda_c^2}\left(\mathrm{OPD}_c - \lambda_c T_w \frac{dn}{d\lambda}\right)\Delta\lambda - 2\pi\left(\frac{\Delta\lambda}{\lambda_c}\right)^2 \frac{dn}{d\lambda}T_w. \tag{6.21}$$

The last term on the right-hand side is negligibly small for the several tens of micrometers glass we add to the reference path and the bandwidth of a few nanometers that we normally consider. The 2nd term on the right-hand side of this equation is the a_0 term that gives rise to the linear dispersion:

$$a_0 = -\frac{2\pi}{\lambda_c^2}\left(\mathrm{OPD}_c - \lambda_c T_w \frac{dn}{d\lambda}\right). \tag{6.22}$$

The a_0 term from Eq. can be tuned to 0 by either adjusting the delay line or the wedges. In this paper we adjusted the wedge which leads to a a_0 shift of 0.91 nm^{-1} when translating the wedge by 1 mm at a wavelength of 532 nm.

Appendix B. Derivation of chromatic dispersion a_4

The a_4 term represents the chromatic dispersion of the imaging lens which causes a wavelength-dependent defocus ΔF. The optical path difference (OPD) at a normalized radial position ρ in the exit pupil, introduced by this small defocus of the object ΔF, equals

$$\mathrm{OPD} = \Delta F\sqrt{1-\mathrm{NA}^2\rho^2}. \tag{6.23}$$

The OPD described in Eq. 6.23 results in a phase variation which equals,

$$\phi(\lambda) = 2\pi\frac{\mathrm{OPD}}{\lambda}, \tag{6.24}$$

where λ is the wavelength. The phase shift with respect to the wavelength, can be determined by differentiating Eq. 6.24 yielding,

$$\frac{d\phi}{d\lambda} = 2\pi\left(\frac{1}{\lambda}\frac{d\Delta F}{d\lambda} - \frac{\Delta F}{\lambda^2}\right)\sqrt{1-\mathrm{NA}^2\rho^2}, \tag{6.25}$$

where $2\pi\left(\frac{1}{\lambda}\frac{d\Delta F}{d\lambda} - \frac{\Delta F}{\lambda^2}\right)$ represents the chromatic defocus. Since the quadratic defocus term $\frac{\Delta F}{\lambda^2}$ is negligible small compared to the linear defocus term $\frac{1}{\lambda}\frac{d\Delta F}{d\lambda}$ we obtain the following Eq. for a_4

$$a_4 = 2\pi\frac{1}{\lambda_c}\frac{d\Delta F}{d\lambda}. \tag{6.26}$$

For the custom made high-NA imaging lens we have a wavelength-dependent focus shift of approximately 720 nm/nm at $\lambda = 532$ nm. This yields a value of $a_4 \approx 8.5\ \mathrm{nm}^{-1}$.

CHAPTER 7

COMPUTATIONAL CORRECTION OF SPURIOUS APODIZATION FOR ARBITRARY SPECTRAL SHAPES USING A FOURIER-TRANSFORM SPECTROMETER

The use of quasi-monochromatic light in digital holographic microscopy can lead to spurious apodization effects. The resulting image degradation can be computationally corrected for this effect if the spectrum of the light source is known. Here, we present a simple Fourier-transform spectrometer that accurately measures the spectrum of a quasi-monochromatic light source. This spectrometer is conceptually simple, low-cost and has no moving parts which makes it very suitable for in-line calibrations of the spectral shape of a light source in a metrology tool. We will present measured spectra, obtained with this spectrometer, and we will show how these spectra can be be used to computationally correct for spurious apodization effects.

Published as: J. Kim, T. van Gardingen-Cromwijk, M. Noordam, J.F. de Boer, Y. Kang, C. Park and A. den Boef, *Correcting spurious apodization effects in digital holographic microscopy using a simple Fourier transform spectrometer*, Opt. Continuum **4**, 382-395 (2025)

7.1 Introduction

In the previous chapter, the spurious apodization effect was demonstrated based on measured point-spread functions (PSFs) of the dark-field digital holographic microscope (DHM) system. Fig. 7.1 (a) and (b) show two examples of this study where the variation in amplitude distribution affects the PSF, which characterizes the imaging properties such as crosstalk and resolution. The desired PSF for our imaging system has a homogeneous amplitude distribution, resulting in an Airy disk in the image plane [75]. This pupil amplitude distribution and PSF are presented in Fig. 7.1 (c), and obtained by measuring with a 1 nm bandwidth filter. However, due to photon budget and a ideal coherence length of approximately 150 µm, quasi-monochromatic light is required in DHM for overlay metrology, resulting in spurious apodization.

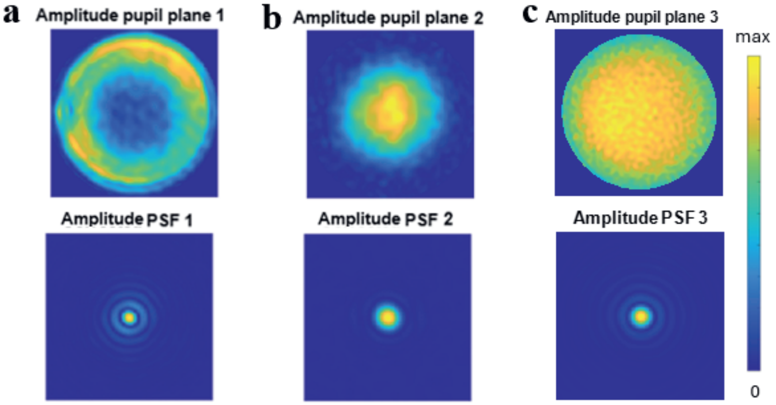

Figure 7.1: (a) and (b) are two examples on the spurious apodization effects, where the measured amplitude distribution affects the imaging quality of the imaging system, demonstrated by the PSF, which was illuminated using a Gaussian spectral shape. [76]

Fortunately, this spurious apodization effect can be computationally corrected provided that we know the spectral shape of the light source. In the previous Chapter (Ref. [76]), a Gaussian shape was assumed but there are plenty of cases where this assumption is not valid. For example, the quasi-monochromatic light generated by a supercontinuum source with an Acousto-Optic Tunable Filter (AOTF) can have a spectrum that significantly deviates from a Gaussian shape [77–80]. Therefore, the spectral shape needs to be accurately measured for the best possible computational correction of the spurious apodization.

The Fourier-Transform (FT) spectrometer, that we will present in this chapter, is ideally suited to measure the spectral shape of quasi-monochromatic light over a large range of wavelengths.Compared to conventional FT spectrometers, our FT spectrometer has no moving parts, is compact, low cost and can be calibrated with only one wavelength. Due to its simplicity and lack of moving parts, it can potentially be fabricated as a photonic integrated circuit, thereby minimizing the spectrometer's footprint. These features make it an attractive option for overlay metrology using DHM. Here, the required sub-nanometer metrology precision drives the need for near-perfect imaging conditions over a large range of wavelengths. The disadvantage of this FT spectrometer concept is that the OPD range limits the spectral resolution. For the application of overlay metrology the spectral resolution is far below what is needed, but for other application this might be a disadvantage.

In this chapter, we present details on our FT-spectrometer concept, along with a description of a simple setup that we build for experimental validation. We will explain the concept and show experimental validation of this spectrometer. Finally, we will show how our FT-spectrometer is able to correctly predict spurious apodization in a DHM setup using light with a strong non-Gaussian spectral shape. We will use this spectrum-based calculation to correct the point-spread function of our DHM setup.

7.2 Theory and System Design

7.2.1 Concept FT-spectrometer

Our FT-spectrometer method is similar to the well-known Young's double-slit experiment [81] and is conceptually shown in Fig. 7.2 [82]. The two pinholes have a separation $2d$ and are placed along the x-axis. These pinholes are both illuminated by the same light source S. The light transmitted by the two pinholes propagate as diverging spherical waves that will overlap and interfere on the image sensor. There is a significant non-linear relation between the optical path length difference (OPD) of the two pinholes (x, y) position on the image sensor which is illustrated with the curved fringes in Fig. 7.2. However, this non-linear relation is well-defined and can be corrected. After a simple non-linearity correction, followed by a Fourier Transform of the interferogram we obtain the source spectrum.

7.2.2 Theory

In this Fourier-Transform spectrometer concept, the two spherical waves generated by the two pinholes interfere with each other at the camera sensor. The complex fields from the two pinholes can be expressed as,

$$E_{\pm 1} = \sqrt{I_S(k)}\sqrt{I_{\pm 1}}\left(x, y\right) \exp\left[-i2\pi k\, L_{\pm 1}\left(x, y\,\right)\right], \tag{7.1}$$

where -1 and $+1$ represent the left and right pinhole respectively, $I_S(k)$ is the source intensity at wavenumber $k = 1/\lambda$ and $I_{\pm 1}\left(x, y\right)$ describe a slowly varying relative intensity variation across the camera plane due to angle-dependent scattering from each pinhole. $L_{\pm 1}$ is the optical path length from each pinhole to a position $\left(x, y\right)$ on the image sensor. The total intensity distribution on the image sensor is obtained by integrating over the entire source spectrum, given by

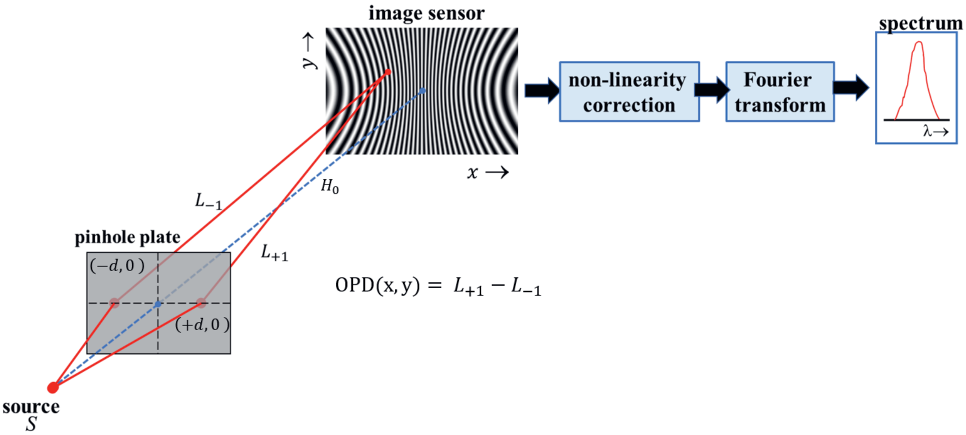

Figure 7.2: Conceptual sketch of our FT-spectrometer. A light source S illuminates the two pinholes that generate two spherical waves that interfere on the image sensor. For the sake of clarity, the fringe density on the image sensor and its non-linear variation, due to the non-linear optical path length different (OPD), is shown highly exaggerated.

$$I(x,y) = \int_0^\infty |E_{+1} + E_{-1}|^2 \, dk = \int_0^\infty I_S(k) \left[I_{+1} + I_{-1} + 2\sqrt{I_{+1} I_{-1}} \cos\left(2\pi k \mathrm{OPD}(x,y)\right) \right] dk. \tag{7.2}$$

The optical path difference is given by OPD = $L_{+1} - L_{-1}$. In our setup, we eliminate the weak angle-dependent diffraction by also measuring the two fields on the image sensor separately. This allows us to obtain a background-free normalized interference signal, given by

$$I_N(x,y) = \int_0^\infty I_S(k) \cos\left[2\pi k \mathrm{OPD}(x,y)\right] dk. \tag{7.3}$$

In Eq. 7.3, the OPD variation across the camera location (x,y) is given by:

$$\mathrm{OPD} = \sqrt{(x+d)^2 + y^2 + H_0^2} - \sqrt{(x-d)^2 + y^2 + H_0^2}, \tag{7.4}$$

where the H_0 is the distance from the pinhole plane to the image sensor and $2d$ is the two pinholes spacing. In practice, the distance H_0 is much larger than the image sensor dimensions and pinholes spacing. Using the Taylor approximation $\sqrt{1+a} = 1 + (a/2) - (a^2/8)$ the OPD can be expressed as:

$$\mathrm{OPD} = \left(\frac{2d}{H_0} - \frac{d^3}{H_0^3} - \frac{dy^2}{H_0^3} \right) x - \frac{d}{H_0^3} x^3. \tag{7.5}$$

As shown in Fig. 7.2 and expressed in Eq. 7.5, a linear relation between OPD and the x-position on the camera sensor is obtained near the center of the image sensor. However, for large x-values a third order distortion becomes significant. Moreover, the OPD scaling is also weakly y-dependent.

The OPD expression of Eq. 7.5 assumes that the image sensor plane is perfectly aligned relative to the two pinholes. In reality, the image sensor can be slightly decentered over a distance S_x and S_y in, respectively the x- and y-direction. Moreover, the image sensor plane can also be tilted over small angles θ_x and θ_y around the x- and y-axis. Finally, the two pinholes can be slightly rotated over a small angle α around the z-axis. These small misalignment's create additional OPD variations across the image sensor area. Combining all misalignment terms, the optical path length for each individual pinhole can be expressed as,

$$L_{\pm 1} = \sqrt{(x \pm d + S_x)^2 + \left(y \pm \alpha d + S_y\right)^2 + \left(H_0 + x\theta_y + y\theta_x\right)^2} \tag{7.6}$$

Here, we assume that angular misalignment's are sufficiently small to use the well-known small angle approximation $\sin(a) = a$, $\cos(a) = 1$. These misalignment's in the setup can degrade accuracy and resolution of our spectrometer concept and must therefore be taken into account. The terms $S_{x,y}$, $\theta_{x,y}$ and α can be calibrated and included in the correction of the non-linear OPD variation across the image sensor plane. The calibration of H_0, d and the parameters that describe the small sensor misalignment's, S_x, S_y, θ_x, θ_y and α is done with a simple model-based iterative technique that needs only one accurately known wavelength (e.g. a HeNe laser) to determine the misalignment parameters. A detailed explanation of the calibration method using a HeNe source is presented in Appendix A.

7.3 Experiment

7.3.1 Experimental setup

In this section, we will describe the experimental setup used in this study. Fig.7.3 (a) shows a schematic drawing of the setup that was built to evaluate our FT-spectrometer concept. Light from a source is collimated with achromatic lens L1 (Thorlabs ACT508-200-A-ML, f=200 mm) and is sent to a regular Michelson interferometer configuration consisting of beam splitter (BS) and two mirrors (M3 and M4). These mirrors are tilted over an angle of approximately 0.48° resulting in two reflected beams that have opposite tilts.

Achromatic lens L2 (Thorlabs AC508-100-A-ML, F=100 mm) focuses these tilted beams on the two pinholes that have a diameter of 5 µm and a separation $2d$ of 4 mm. These pinholes were made in a 300 nm thick Chromium film on a glass substrate using a focused ion beam. The pinholes act as a spatial filter that improve the beam quality resulting in two well-defined diverging spherical beams that travel from the pinholes over a distance H_0 ($\approx$ 126 mm) towards the camera (Basler boA8100-16cm CoaXPress) that records the interference between the two spherical waves. The camera has an Onsemi XGS 45000 image sensor with a global shutter and 8192 (x-direction) × 5468 (y-direction) pixels with a pixel pitch of 3.2 µm. The HeNe laser source (Thorlabs HRS015B) shown in Fig. 7.3 (a)

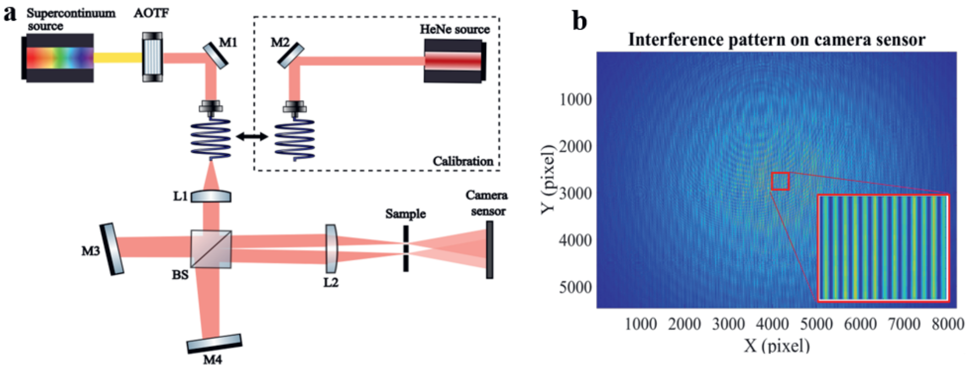

Figure 7.3: (a) Schematic representation of the two pinhole FT-spectrometer setup. (b) A measured interference pattern on the camera sensor.

is used to calibrate our FT-spectrometer. Further details of this calibration method are presented in the next section. The other source in Fig. 7.3 (a) is a white light supercontinuum source (LEUKOS ROCK400-5) with two acoustic optical tunable filters (AOTF's) for wavelength selection covering the visible to near infrared wavelength range. Fig. 7.3 (b) shows an example of a measured interference pattern of the HeNe-laser calibration source before correction of the individual beam profiles. This setup is especially suited for high-brightness sources with a finite bandwidth like supercontinuum sources in combination with AOTF's that are used in our research on DHM for metrology applications.

7.3.2 Non-linearity correction method

Due to the non-linear OPD, described in section 7.2.2, the intensity of the interferogram is not purely sinusoidal but has multiple frequency components, as illustrated using a simulation in Fig. 7.4 (a). Performing a Fourier transform over such a non-sinusoidal interferogram results in a broad undefined spectrum, as shown in Fig. 7.4 (d), indicated in red. Linear interpolation is used to linearize the sample of the OPD, as shown in Fig. 7.4 (b). Here, the non-equidistant dashed lines above represent OPD values that correspond to the pixels at location x in the detector array. The dashed lines below represent the OPD after linear interpolation. This non-linearity correction is performed in MATLAB using the standard interpolation function "interp1" with a spline fit. The interpolated interferogram now has a single frequency component as illustrated in Fig. 7.4 (c). The corresponding Fourier transform of this interpolated interferogram then results in a single-peak spectrum as shown with the blue curve in Fig. 7.4 (d).

To apply this non-linearity correction the system parameter are experimentally calibrated with a HeNe source. This calibration is presented in Appendix A. The non-linear correction method will be validated experimentally in the following section where we present the experimental results of this FT-spectrometer.

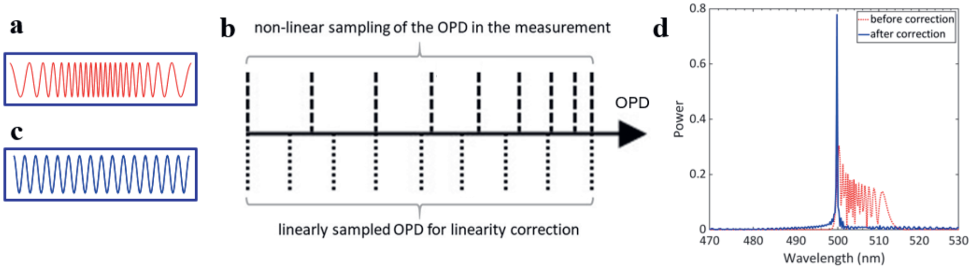
a
c
b
non-linear sampling of the OPD in the measurement
OPD
linearly sampled OPD for linearity correction
d
before correction
after correction
Power
0
0.2
0.4
0.6
0.8
470
480
490
500
510
520
530
Wavelength (nm)

Figure 7.4: Schematic illustration of the non-linearity correction using pixel interpolation. A simulation using Eq. 3 and Eq. 4 of the non-linear interference pattern (a) is linearized using non-linear sampling of the pixels (b) resulting in a linear interference pattern (c). (d) The Fourier transform of the linear and non-linear interference pattern in blue and red respectively.

7.4 Results and discussions

Here, we verify the calibration by measuring the spectrum of a known bandwidth filter. We present first experimental data on the accuracy of the measured spectrum and show that our spectrometer can cover a large wavelength range. Finally, we will show how our FT-spectrometer is able to correctly predict spurious apodization in a DHM setup using light with a strong non-Gaussian shape. We will use this spectrum-based calculation to correct the PSF of our DHM setup.

7.4.1 Validation of calibration quality

After calibrating the system using a HeNe source and following the procedure as presented in Appendix A, the calibrated parameters are now used to correct the non-linear OPD variation in a spectrum measurement. To verify the calibration parameters, a 532 nm color filter with a 1 nm bandwidth is measured. From the non-linear corrected interferogram, each horizontal line can be Fourier-transformed resulting in a spectrum of the light source, as shown in Fig. 7.5 (a). Therefore, also the consistency over the y-axis has been experimentally verified as presented in Fig. 7.5 (b).

The retrieved central wavelength is equal to 532.0 ± 0.1 nm and the measured FWHM is 1.3 nm. The spectral resolution of this FT spectrometer with 8192 number of pixel in one line is 0.4 nm. The coherence length is proportional to $L_c \approx \frac{\lambda^2}{\Delta\lambda}$, which in our system is represented by the maximum OPD range. So, we can approximate the OPD range as OPD $\approx \frac{\lambda^2}{\Delta\lambda}$. Therefore, the spectral resolution of our FT spectrometer is approximately equal to $\Delta\lambda \approx \frac{\lambda^2}{\mathrm{OPD}}$. With a measured wavelength of 532 nm and a OPD ranging from -400 to 400 µm, this results in a spectral resolution of $\Delta\lambda \approx \frac{0.532.^2}{800} \cdot 10^3 = 0.4$ nm. Fig. 7.5 (b) shows the error of the retrieved central wavelength for a source with a 532 nm wavelength. The error is defined as the difference between the retrieved wavelength and the color filter 532 nm. Fig. 7.5 (b) shows that for most horizontal lines in the corrected interferogram array (the range of $-3<y<8$ mm) the retrieved central wavelength runs very smoothly with low

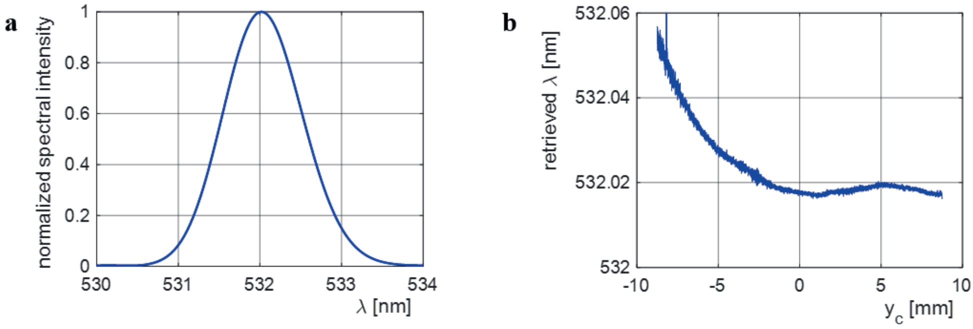

Figure 7.5: (a) Retrieved spectra using middle row of the interferogram after non-linearity correction. (b) Measured error of the retrieved wavelength as function of y-position for a 532 nm source.

noise per interferogram line. The error slightly increases towards y = -8 mm which can be attributed to the larger ΔOPD residuals that were observed in the top left image of the interferogram during the calibration, caused by spherical aberrations. These spherical aberrations could be caused by the relatively large diameter of the pinholes. A potential solution for this problem is described in section 7.5.

Next, the quality of our calibration methods was tested using a supercontinuum source equipped with two AOTF's (A and B). With these two AOTF's we generated quasi-monochromatic light in the range of 450 nm to 950 nm with 50 nm steps. For each programmed wavelength the central wavelength was measured using our FT-spectrometer.

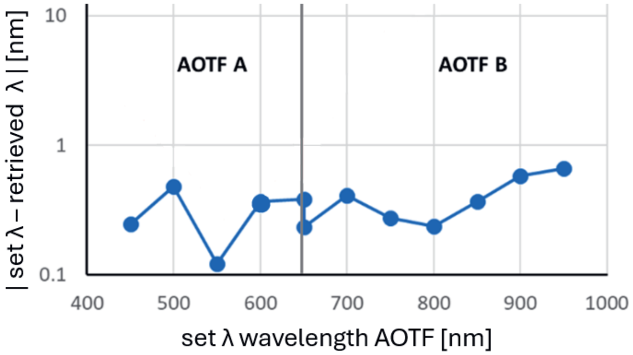

Figure 7.6: (a) Measured wavelength error of our FT-spectrometer as a function of wavelength. The wavelengths of 450 nm – 650 nm were generated with AOTF-A and the wavelengths of 650 nm – 950 nm were generated with AOTF-B.

The results of this wavelength range experiment are shown in Fig. 7.6. The FT-spectrometer shows small errors well below 1 nm over a wavelength range of 450 nm to 950 nm. So with one calibration wavelength our FT spectrometer can accurately measure over a broad wavelength range. Lastly, the results presented in Fig. 7.6 were obtained without readjusting optical elements as we changed the wavelength from 450 nm to 950 nm.

7.4.2 Computational spurious apodization correction

In DHM for overlay metrology, the spectral shape is determined by the acoustic optical tunable filter (AOTF). These AOTFs are commercially available, affordable, and offer fast color switching, making them suitable for high-throughput measurement applications, like overlay metrology. However, the complex non-linear acousto-optic interaction between the propagating optical and acoustical waves [83, 84] can result in spectral line shapes that significantly deviate from the more common Gaussian or tophat-shaped filters. In coherent imaging systems such a non-Gaussian spectral line shape could result in spurious apodization effects affecting the image quality, as described in Ref. [76]. Here, the amplitude distribution in the pupil plane is directly related to the spectral shape. Therefore, accurate knowledge of the spectral characteristics of the illumination light source is required, and can allow for computational correction of this spurious apodization in DHM.

In this section, we will use our FT-spectrometer setup to measure the shape of the spectral transmission of an AOTF in more detail. The spectral shape of the AOTF depends on the wavelength and RF driving power. Variations in spectral shapes with different RF powers in an AOTF arise from non-linearity in acousto-optic interaction. Increasing the RF power amplifies the acoustic wave, affecting diffraction efficiency and the Bragg condition, which results in wavelength dependence. Moreover, material properties also behave non-linearly with RF power. In combination with localized heating from higher powers that alter the refractive index, this results in spectral shape which are highly dependent on wavelength and RF power [77–80]. Fig. 7.7 shows the main findings of the AOTF characterization. The spectral shape is measured for programmed wavelengths of 550 nm (a-d), 650 nm (e-h) and 750 nm (i-l) with four different drive powers (4000, 5000, 6000 and 7000 mW). Especially at the longer wavelength (750 nm) we see that the spectral shape deviates significantly from the desired Gaussian or top hat shape. Moreover, the shape highly depends on the RF-drive power.

In Ref. [76] it was presented that the finite bandwidth of the light source in combination with a wavelength-dependent focal length of the imaging lens leads to a significant field-position dependent spurious apodization in our DHM setup. This significantly affects the aberration-corrected PSF in the DHM tool for overlay metrology. In that study, it was demonstrated that this spurious apodization, coming from an inhomogeneous amplitude distribution in the pupil plane, depended on the finite bandwidth of the source spectrum. In Ref. [76], for simplicity reasons, the spectral shape was assumed to be Gaussian. However, as shown in Fig. 7.7, the output spectrum of an AOTF is not a perfect Gauss-function and is highly dependent on wavelength and RF driving power [77–80]. Therefore, an accurate in-line spectrum measurement is important to allow a computational apodization correction to the levels of accuracy that is needed for demanding metrology applications. Such spectrum measurement can then be used to calculate

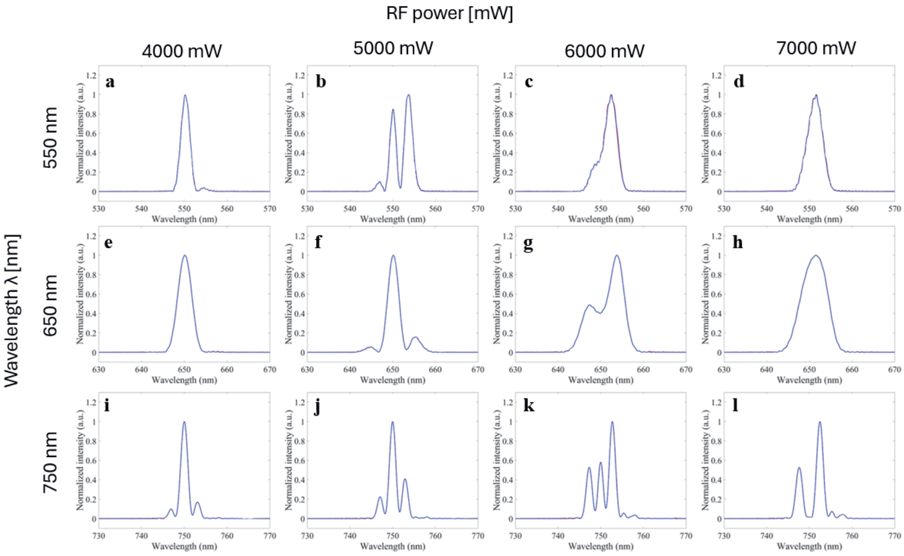

Figure 7.7: Measured spectral transmission of our AOTF for 3 different wavelengths (a-d) 550 nm, (e-h) 650 nm and (i-l) 750 nm) for different radio-frequency (RF) drive powers (4000, 5000, 6000 and 7000 mW).

the amplitude variation in the pupil plane and computationally correct for it. Fig. 7.8 demonstrates this approach with experimental results. Here, a silicon sample with a nanohole, diameter 200 nm and depth 100 nm, is illuminated resulting in a scattering point source. The point source illuminates the lens aperture with a spherical wave. In case of a very narrow bandwidth (B < 1 nm), the amplitude in the exit pupil plane is a homogeneous distribution. For comparison, a measured pupil amplitude distribution of a 1 nm bandwidth filter was presented in Fig. 7.1 (c).

However, when illuminating the nanohole with an non-Gaussian AOTF spectrum, Fig. 7.8 (a), the measured pupil amplitude is a non-homogeneous distribution, as shown in Fig. 7.8 (b). As described in Ref. [76], the amplitude in the exit pupil plane can be expressed as,

$$A_{\mathrm{EP}}(\gamma) = \int_{-\infty}^{\infty} S(\Delta\lambda) \exp[i\gamma\Delta\lambda]\, d\Delta\lambda, \tag{7.7}$$

where $S(\Delta\lambda)$ is the source spectrum and γ a dispersion parameter. Using this expression the expected pupil amplitude distribution can be calculated based on the measured spectrum. The calculated pupil amplitude, using the measured spectrum (Fig. 7.8 (a)), is presented in Fig. 7.8 (c). A computational correction of the non-homogeneous pupil amplitude caused by spurious apodization is then performed by dividing the measured pupil amplitude by the calculated pupil amplitude,

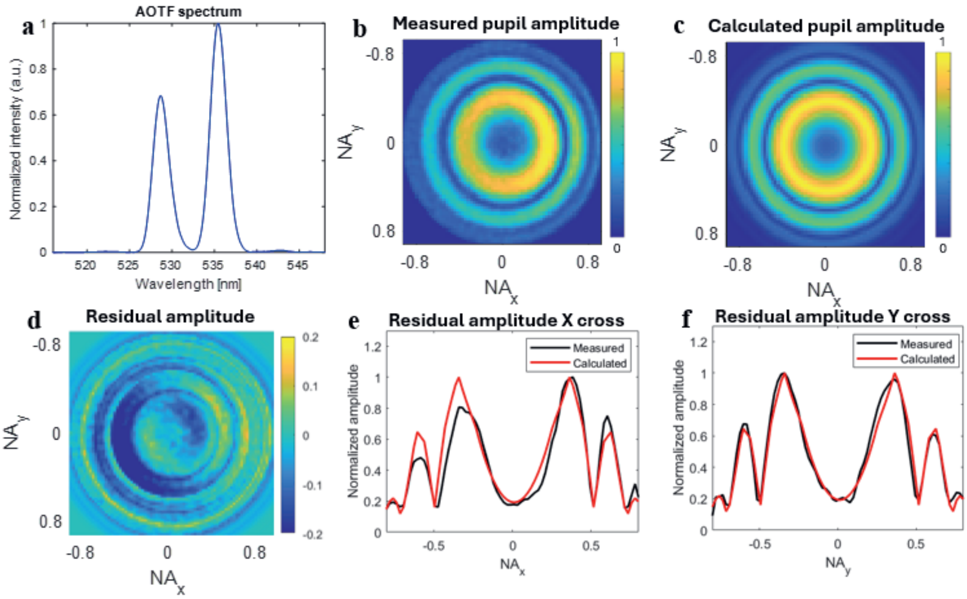

Figure 7.8: Experimental correction of spurious apodization in DHM using the measured spectrum. (a) The measured non-Gaussian AOTF spectrum. (b) The measured pupil amplitude distribution. (c) The calculated pupil amplitude distribution based on the measured AOTF spectrum. (d) The residual amplitude distribution by subtracting (c) from (b). (e) and (f) show a x- and y- cross section of the residual amplitude, respectively.

$$A_{\text{cor}} = \frac{A_{\text{meas}}}{A_{\text{calc}}}. \tag{7.8}$$

The residual amplitude, i.e. the difference between the calculated A_{calc} and A_{meas} is presented in Fig. 7.8 (d). Here, homogeneity in the amplitude distribution significantly improved after correction. Some residual amplitude variations are present caused by a small mismatch between the measured amplitude A_{meas} and the calculated amplitude A_{calc}. This mismatch is mainly related to the scattering profile of the nanohole. This scattering profile is observed in Fig. 7.8 (b) as slightly more light in the right half of the pupil plane. This asymmetry is present in the x-direction, as shown in the x-cross section in Fig. 7.8 (e), but is not present in the y-direction, as shown in the y-cross section in Fig. 7.8 (f). In the y-direction, our calculated amplitude distribution matches the measured amplitude distribution very well. The nanohole's used in this study have a diameter of 200 nm, measured with a center wavelength of 532 nm. For a nanohole to scatter a perfectly spherical wavefront, the diameter should be much smaller than the measurement wavelength. In this study, the diameter of the nanohole is relatively large compared to the wavelength. Therefore, the scattering profile is not perfectly spherical but has some angular dependence in the x-direction. A smaller nanohole makes the scattering profile more symmetrical resulting in less residual artifacts. However, the smaller the nanohole the less light is scattered, resulting in more photon noise in the signal. Therefore, in this study a diameter of 200 nm was chosen accepting the imperfect scattering profile.

Back-propagating the measured and corrected complex-valued pupil planes to the image plane using an inverse Fourier transform, results in the PSF amplitude presented in Fig. 7.9 (a) and (b), respectively. The spurious apodization lead to broadening of the sidelobs of the PSF as shown in Fig 7.9 (a). Correcting the pupil amplitude to a homogeneous amplitude distribution based on the source spectrum, results in a Airy disk function as shown in the Fig. 7.9 (b). Fig. 7.9 (c) shows the cross section of (a) and (b) compared to the theoretical Airy disk function. There is a small mismatch visible between the corrected PSF cross section (red) and the theoretical cross section (black), which can be explained by the scattering profile of the nanohole as discussed earlier. Nevertheless, the accurately measured spectrum using our FT-spectrometer, allows for computational correction of the spurious apodization effect in DHM.

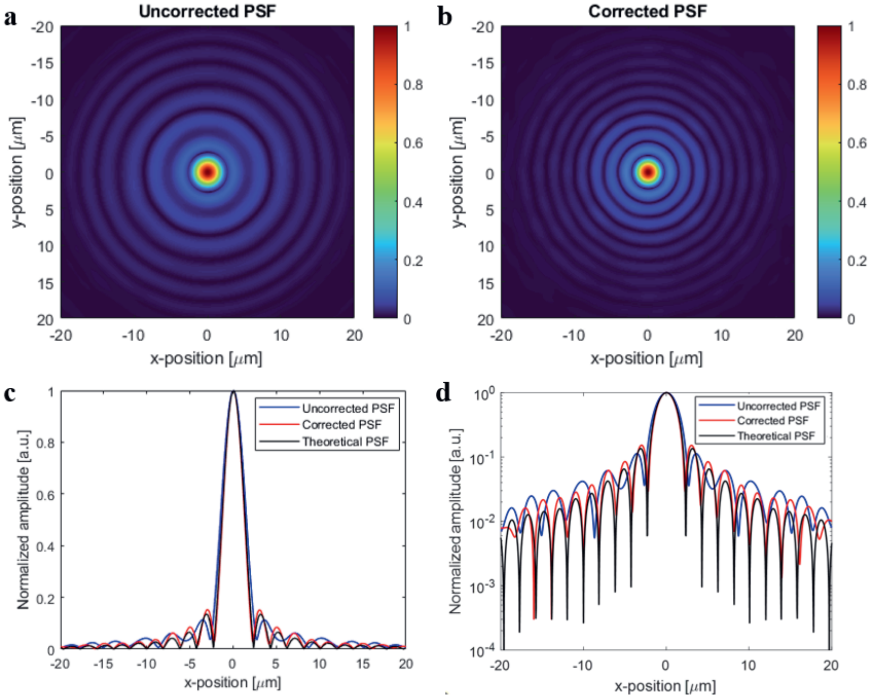

Figure 7.9: The resulting PSF in the image plane before (a) and after (b) correction of spurious apodization in DHM using the measured spectrum. (c) shows the cross section of the uncorrected PSF (blue) and the corrected PSF (red) with respect to the theoretical Airy disk (black) and on logarithmic scale in (d).

7.5 Future improvements

Future improvements: In this section, we will discuss the current limitations of the existing FT spectrometer setup and future improvements.

1. **Aberration minimization:** The main limitation of the current setup are aberrations caused by the relatively large pinhole diameter of 5 micrometer, which degrade fringe quality. As a future improvement, we plan to measure with smaller pinholes. A 1-micrometer pinhole would transmit a less aberrated wavefront, potentially enhancing fringe pattern quality. Additionally, developing an OPD model that accounts for aberrations would allow calibration of these effects as a system parameter, further minimizing their impact.

2. **DHM implementation:** In this study, the concept was experimentally validated using a PSF measurement. As a next step, we aim to measure an actual overlay target and enhance overlay retrieval through computational correction of spurious apodization. Thus far, spectral shape and PSF measurements were conducted sequentially. For overlay measurements, simultaneous spectrum and overlay target acquisition would be more advantageous. Fig. 7.10 illustrates a potential implementation of the FT spectrometer within the df-DHM setup.

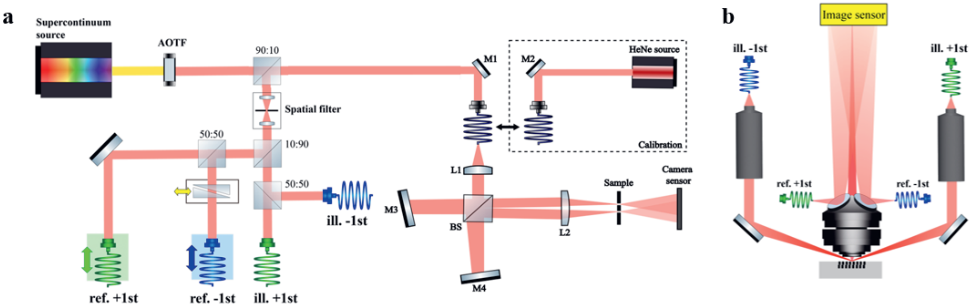

Figure 7.10: A schematic representation of the FT spectrometer concept implemented in our df-DHM setup. (a) The beamsplitting part where the FT spectrometer is connected. The source can be changed from the supercontinuum source to the HeNe source for calibration purposes. The beams are guided via polarization maintaining single mode fibers to the sensor head (b).

3. **Precision study:** The spectral resolution of 0.4 nm achieved with our FT spectrometer concept is currently limited by the OPD range and the finite number of pixels. The demonstrated sub-nm resolution is sufficient for various metrology applications, including semiconductor optical metrology tools. In our work, the number of pixels was constrained to 8192, but advances in image sensor technology are expected to provide sensors with more and smaller pixels, enabling further resolution improvements. Once higher resolution is achieved, a precision study with a detailed error analysis across the entire wavelength range would be valuable.

Implementing these future improvements will overcome current limitations, enhance spectral resolution, reduce aberrations, and streamline measurement processes, ultimately advancing the capabilities and accuracy of the FT spectrometer.

7.6 Conclusion

In this study, we have presented a simple and accurate spectrometer based on two interfering spherical beams. The FT-spectrometer can be calibrated using only one reference wavelength, while still accurately measuring over a large wavelength range. Moreover, our model-based calibration method is simple and robust against misalignment of the few parts in our FT-spectrometer. The sub-nm spectral resolution that we have demonstrated is sufficient for various applications including semiconductor optical metrology tools. We concluded the study with experimental work on spurious apodization correction using the measured spectrum in DHM for overlay metrology.

Appendix A : System parameter calibration

The calibration of H_0, d and the parameters that describe the small sensor misalignment's, S_x, S_y, θ_x, θ_y and α is done with a simple model-based iterative technique that is already well-established in semiconductor metrology applications like optical CD metrology [85]. Fig. 7.11 presents a flow chart of our model-based calibration method.

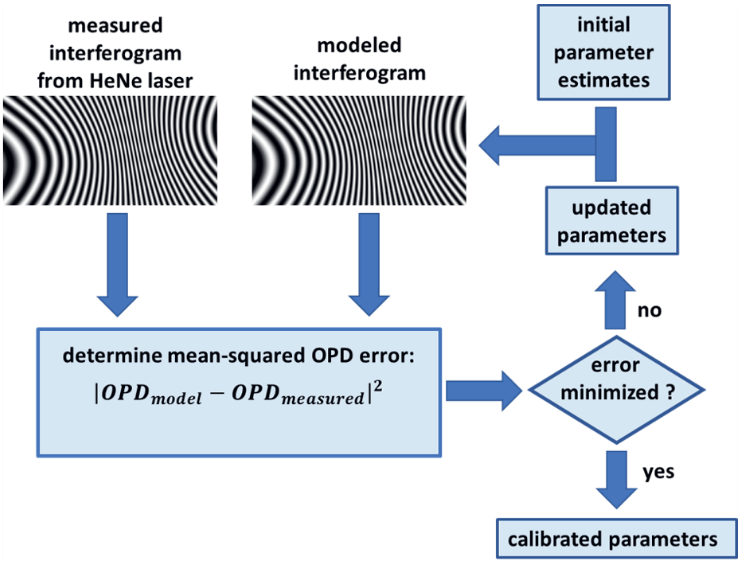
measured interferogram from HeNe laser
modeled interferogram
initial parameter estimates
updated parameters
no
determine mean-squared OPD error:
$|OPD_{model} - OPD_{measured}|^2$
error minimized ?
yes
calibrated parameters

Figure 7.11: Schematic flow chart of the model-based calibration method that was used to determine the parameters $S_{x,y}$, $\theta_{x,y}$, α, d and H_0.

Starting from a set of initial parameter estimates, a modeled interferogram is calculated using Eq. 7.6. A computational phase-stepping approach is then performed to calculate the difference between the OPD of the measured interferogram and the modeled interferogram. Based on the retrieved OPD difference, a new set of parameters is obtained and a new modeled interferogram is calculated. This loop is repeated until the mean-squared OPD difference (ΔOPD = OPD$_{model}$ - OPD$_{measured}$) is minimized. This iterative minimization of the OPD error is fast and accurate since the model is based on simple free space propagation of spherical waves with only a few unknown model parameters. However, it assumes that these model parameters have different OPD-sensitivities. The parameter sensitivities of our FT-spectrometer concept are simulated using Eq. 7.6 for a pinhole separation $2d$ of 4 mm, a pinhole-image sensor distance H_0 of 125 mm. The simulation showed identical OPD sensitivity behavior for image sensor shift in the y-direction (S_y) and tilt around the x-axis (θ_x). These two misalignment's can therefore not be independently calibrated. However, sensor tilt has a much lower sensitivity than sensor shift. Therefore, we assume θ_x to be zero in our calibration.

For calibration of our FT-spectrometer three images are captured. First, we measure the interference pattern on the image sensor using the HeNe laser. Then also images of the individual pinholes, are measured to remove the amplitude envelope and DC background term from the interferogram. Our model-based calibration approach minimized the OPD difference ΔOPD between the measured and the modeled interferogram. Fig. 7.12 shows this OPD difference at various stages the calibration process.

	before calibration	**after calibration of H_0 and d**	**after full calibration**
$\Delta OPD(x,y)$ [nm]	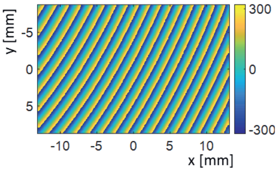	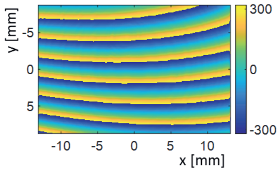	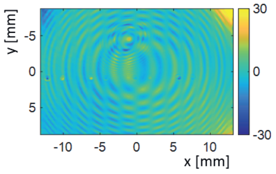
H_0 [mm]	125	127.160	127.160
d [mm]	2	2.009	2.009
S_x [mm]	0	0	1.29
S_y [mm]	0	0	-1.12
θ_y [mrad]	0	0	-9.6
α [mrad]	0	0	-7

Figure 7.12: Difference between measured and modeled OPD at image sensor in various stages of the calibration steps. The table underneath the ΔOPD images shows the corresponding calibration parameters.

In Fig. 7.12, the left image shows the ΔOPD before any calibration has been applied. Here, the parameters are estimated such that the camera and pinholes are perfectly aligned and the the pinhole distance $2d$ equals the design value of 4 mm and the camera-pinhole distance is also equal to its intended value of 125 mm. A clearly visible x-gradient in the ΔOPD indicates that H_0 and/or d need to be adjusted. H_0 and d are then iteratively tuned until the linear x-gradient and the third order non-linearity are eliminated, resulting in the ΔOPD shown in the center image. After this first optimization in the model-based calibration the ΔOPD still contains a strong y-gradient and curvature. Therefore, the parameters $S_{x,y}$ (image sensor shift), θ_y (image sensor tilt) and α (pinhole rotation) are tuned iteratively, resulting in the right column of Fig. 7.12. After this model-based minimization of the ΔOPD a small residual ΔOPD in the range of a tens of nanometers is left. In the residual we clearly see two interleaved concentric rings that are almost certainly caused by spurious interference effects that are introduced by the cover glass that is in front of the image sensor. Moreover, in the residual ΔOPD small but significant ΔOPD values in the upper left and upper right corners are present. This could be caused by a small wavefront aberrations in the two interfering wavefronts. Generally, sufficiently low residual OPD errors were obtained after 10 to 20 iterations. The typical duration of a single calibration iteration on Intel Core i7-1185G7 CPU with 16 GB memory PC is a few seconds, resulting in a total processing time of several minutes.

CHAPTER 8

COMPUTATIONAL IMAGE ENHANCEMENT USING MODEL-BASED SUPPRESSION OF SPURIOUS IMAGING EFFECTS

Achieving sub-nanometer overlay metrology precision requires near-perfect imaging conditions and an almost complete suppression of imaging artifacts. Since digital holographic microscopy measures the full complex-valued field, it enables computational filtering in the pupil plane. In this chapter, we present experimental results of a model-based signal separation technique using digital pupil filtering. This model-based approach allows us to effectively suppress nuisance signals that pose a significant challenge in today;s overlay metrology techniques. Our model-based method does not lead to a loss in resolution so it opens the door towards improved metrology precision on smaller metrology targets.

Published as: T. van Gardingen-Cromwijk, S.G.J. Mathijssen, M. Noordam, S. Witte, J.F. de Boer and A.J. den Boef, *Enhancing diffraction-based overlay metrology capabilities in digital holographic microscopy using model-based signal separation*, J. Micro/Nanopattern. Mats. Metro, **23**, 044006 (2024)

8.1 Introduction

High overlay accuracy and robustness on smaller grating marks with low diffraction efficiency require a strong suppression of undesired signals that impact the desired signal that carries the relevant overlay information. This becomes even more relevant for metrology applications that ask for dense intrafield sampling schemes where overlay must be measured on many points in a field [86]. For these cases there is a need to make the overlay target as small as possible while still maintaining a good metrology precision [16, 17]. Currently, optical overlay metrology is measured in a dark-field microscope and requirements approach sub-nanometer accuracy levels [13] which requires intensity level measurements in diffraction-based overlay (DBO) with a relative precision of the order of 0.01% [26]. Today, these precision levels are easily realized on targets with a dimension of around 16 × 16 μm^2. However, dense intrafield sampling schemes ask for significantly smaller target sizes well below 10 × 10 μm^2 [86].

A reduction of the target size comes with very significant challenges and finite grating effects. For example, a smaller target suffers more from intra-target variations [86]. Therefore, the area where the average intensity level is calculated from, i.e. Region-of-Interest (RoI), should preferably cover the entire grating for small targets, as illustrated in Fig. 8.1 (b). Moreover, a larger RoI will benefit the precision since more photons are available for the overlay measurement.

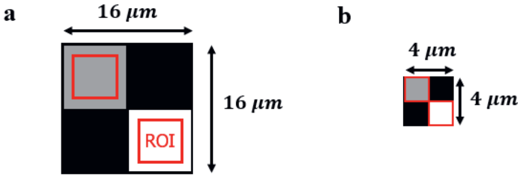

Figure 8.1: Region-of-interest (RoI) selection for conventional (a) and small (b) µDBO targets.

Dark-field imaging of the grating, as shown in Fig. 8.2 (a), results in collecting the first diffraction. For best image quality it is desirable to completely suppress the zeroth order. In practice however, due to the finite size of a target a small amount of zeroth order light leaks into the imaging optics leading to a decrease of imaging quality. This is illustrated in Fig. 8.2 (a), where the zeroth order diffraction (indicated in red) broadens due to the finite grating size. The finite size of the grating causes a sharp change in reflectivity at the edge of the grating. The grating has a reflectivity of R_1 and the top layer has a reflectivity of R_0, as shown Fig. 8.2 (a).

The sharp edges of a finite grating will result in a broadening of the zeroth order signal in the spatial frequency domain. This broadening is inversely proportional to the grating size and will become quite severe for small targets that contain only a few grating lines. Fig. 8.2 (b) shows how these diffraction orders leak into each other, due to the small grating width W = 4 µm in combination with a reflectivity difference of the grating R_1 and the top layer R_0. Fig. 8.2 (c) illustrates this broadening of the zeroth order diffraction

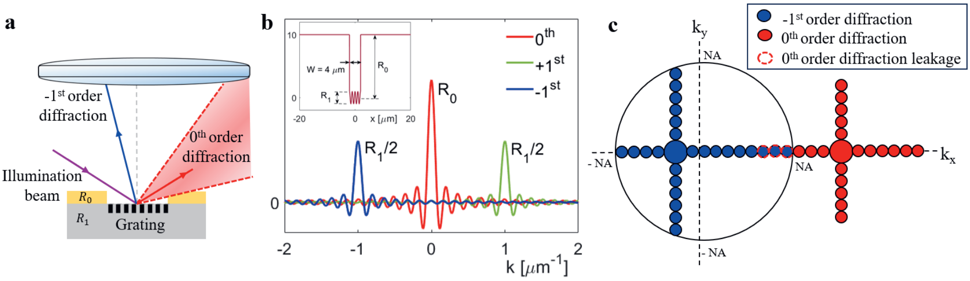
a
-1st order diffraction
0th order diffraction
Illumination beam
R_0
R_1
Grating
b
10
0
W = 4 μm
R_0
R_1
-20
0
x [μm]
20
0th
+1st
-1st
R_0
$R_1/2$
$R_1/2$
0
-2
-1
0
1
2
k [μm^{-1}]
c
k_y
NA
- NA
NA
- NA
k_x
-1st order diffraction
0th order diffraction
0th order diffraction leakage

Figure 8.2: Illustration of zeroth diffraction order leakage concept in (a) dark-field configuration, (b) the 1D pupil plane and (c) the 2D pupil plane. Purple indicates the incoming beam in (a), blue represent the -1^{st} diffraction order and red represents the 0^{th} diffraction order.

leaking into the right side of the 2D case of a pupil, indicated with the dashed red line. In the grating image, zeroth order leakage results in a bright edge of the target and an interference pattern within the target degrading the image quality. For 16 × 16 µm^2 size targets the RoI can be reduced such that bright edges are excluded from the RoI, as simulated in Fig. 8.3 (a), where the red square indicated the RoI. In the case of smaller targets (e.g. 4 × 4 µm^2), the RoI can not be reduced because of intratarget overlay variation due to line edge roughness [86]. For large gratings this effects averages out, but for small gratings that no longer happens. The overlay error due to intratarget variations can be minimized by making the RoI as large as the grating. By doing so, the bright edge end up within the RoI, limiting the DBO metrology performance, as shown in Fig. 8.3 (b) and (c).

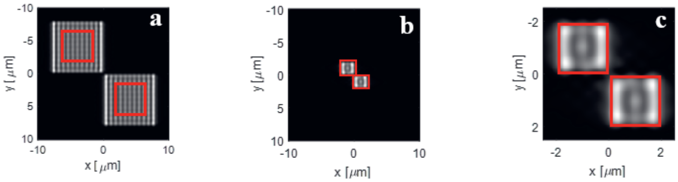

Figure 8.3: Simulation of a (a) 16 × 16 µm^2 and (b) 4 × 4 µm^2 µDBO target with zeroth diffraction order leakage resulting in bright edges and (c) a magnified image of (b). The red box indicates the RoI.

Secondly, putting the RoI boundary at the grating edge results in an overlay measurement which is more sensitive to light leakage from surrounding structures. Photons originating from bright surrounding structures next to the target of interest can leak into the RoI of the overlay target, influencing the accuracy of the overlay measurement. Especially, in coherent imaging systems like digital holographic microscopy (DHM), Gibbs ringing not only leads to degradation of the image quality but also increases the optical crosstalk, i.e. light leakage from surrounding structures into the metrology target.

In this study, we will present a digital pupil filtering technique that allows to suppress target specific artifacts in optical overlay metrology using model-based filtering. We will demonstrate the effectiveness of our technique by presenting nuisance suppression for two different applications. This will allow for a larger RoI enabling the future use of smaller µDBO targets. In order to use digital pupil filtering techniques in dark-field microscopy, the full complex-valued field should be retrieved. In the exit pupil, before an inverse Fourier transform is applied, a digital filter can be applied to filter the signal of interest. Such a filter can be a global window like an apodization window [87], to suppress the overall coherent ringing effects or a specific pupil window to suppress the diffracted light that should not contribute to the OV-signal. The use of an apodization filter is a well-known solution to suppress signal imperfections. These filter do not require any prior knowledge, however apodization normally results in some loss of resolution. In the next section, we will present a model-based digital pupil filter using prior knowledge of the overlay metrology target and the used experimental DHM setup.

8.2 Methods

8.2.1 Model-based digital pupil filter

In semiconductor manufacturing, basic parameters of the overlay metrology target are typically known. Examples of such parameters are size, grating pitch and duty cycle of the grating. Having prior knowledge on the size, geometry or pitch of an overlay metrology target allows for designing a model-based filtering window such that only the diffracted light from the target of interest passes through the pupil. The overlay metrology target, for example, consists of square gratings. Back-propagating a square grating to the pupil plane by Fourier techniques results in a 2D-sinc function [25], as illustrated in Fig. 8.2 (b). The blue 2D-sinc function illustrates the -1^{st} diffraction order in the Fourier plane and the red 2D-sinc function indicates the zeroth diffraction order. The peak of the zeroth diffraction order is not collected in the pupil, but due to the broadening a small portion leaks into the pupil NA indicated with the dashed red circles.

Using the prior knowledge that the zeroth diffraction order leakage shows up as a 2D-sinc function in the pupil, we can fit a model to the measured data. Such model contains two 2D-sinc functions with a relative phase difference. After fitting the model, the zeroth diffraction order contribution can be subtracted from the measurement. This allows one to separate the first- and zeroth-order diffraction signal in the pupil and retrieve an image without the zeroth-diffraction order artifacts. The flowchart of this filter technique is presented in Fig. 8.4.

This model-based technique also applies to other cases where optical crosstalk can impact the quality of an overlay measurement. We can, for example, apply this method to reduce the impact of optical crosstalk from light that is diffracted by structures that surround a metrology target. This diffracted light can leak into the overlay metrology target degrading the overlay measurement accuracy. Reducing the impact of the signal coming from the surrounding structures could result in more robust overlay metrology.

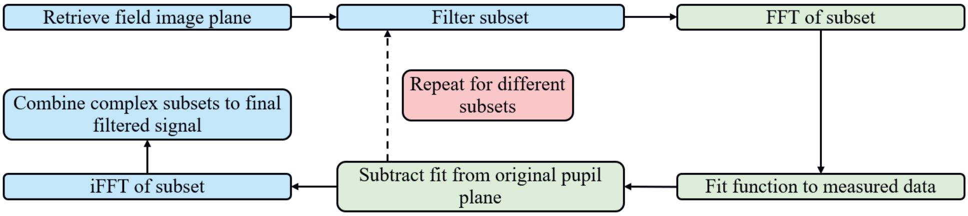
Retrieve field image plane
Filter subset
FFT of subset
Repeat for different subsets
Combine complex subsets to final filtered signal
iFFT of subset
Subtract fit from original pupil plane
Fit function to measured data

Figure 8.4: Algorithm flowchart of the pupil fitting technique, where blue and green represents the image plane and pupil plane respectively.

To test this scenario, here a surrounding target is filtered in the image plane and using a Fourier transform a function, e.g. a complex 2D-sinc function, is fitted to the signal in the pupil plane. This is done for all the surrounding structures and then subtracted from the total measured signal, separating the overlay signal from the surrounding signals. For both presented pupil filtering technique examples an experimental result is presented and discussed in the Results section.

8.3 Results

In diffraction-based overlay metrology it is important to measure the relative intensity differences between the $+1^{st}$ and -1^{st} diffraction order signals as accurately as possible. Any imaging artifacts or target specific artifacts should be eliminated before extracting an overlay value. Here, we will present two experimental examples of signal separation using digital pupil filtering in DHM with the proposed fitting method from Sec. 8.2.1.

8.3.1 Zeroth order suppression

Metrology limitation

The finite size of the grating leads to a broadening of the zeroth order signal in the spatial frequency domain. Fig. 8.5 (a) (simulation) shows this broadening of the zeroth order diffraction leaking into the right side of the pupil. In the grating image, Fig 8.5 (b) (simulation), this results in a bright edge of the target and an interference pattern within the target degrading the image quality and limiting the RoI size.

With the digital access to the pupil plane in DHM, and the prior knowledge of the target geometry we can suppress the zeroth order at the edge of the pupil. By doing so, we eliminate the increased intensity at the edges of the target and the interference pattern within the target, which allows us to select a larger RoI that helps to improve the overlay metrology precision. This suppression will be done by fitting the zeroth order shape, sinc function, in the retrieved pupil of DHM and then subtract that zeroth order field from the pupil plane, as shown in Fig. 8.5 (c). Here, the red line represents a sinc function fitted to the pupil plane. Subtraction of the fitted zeroth order results in a corrected pupil image,

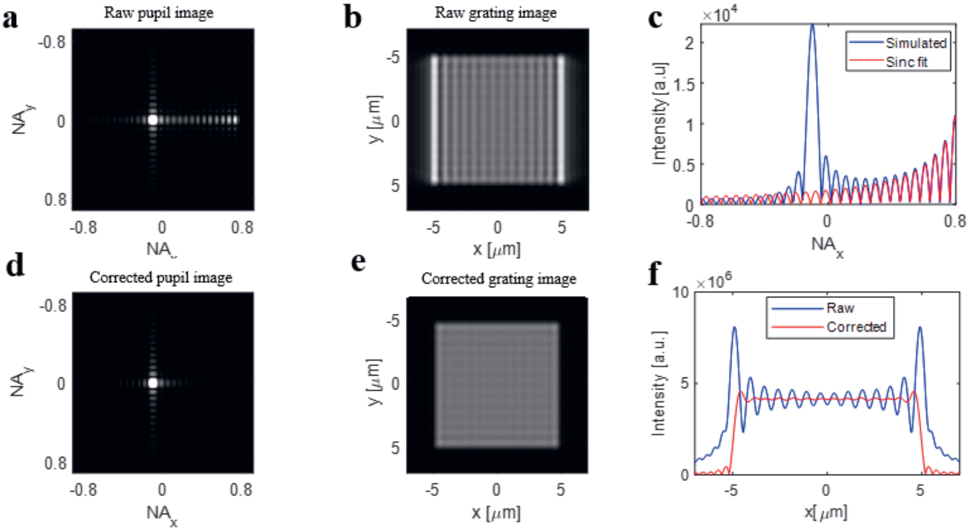

Figure 8.5: Due to the finite grating size the zeroth order diffraction broadens and ends up leaking in the edge of the pupil (a) (simulation). This results in a bright edge in the grating image (b) (simulation). Subtraction of the fitted sinc function to the measured pupil (c) red and blue, respectively, results in a corrected pupil (d) (simulation) and the corresponding corrected grating image (e). Cross sections of grating images (f).

Fig. 8.5 (d), and its corresponding grating in the image plane, as shown in (e). The cross section of the grating images, Fig. 8.5 (f), shows that after correction (red line) the zeroth order artifacts are decreased significantly. The bright edges are suppressed as well as the ringing behaviour across the target.

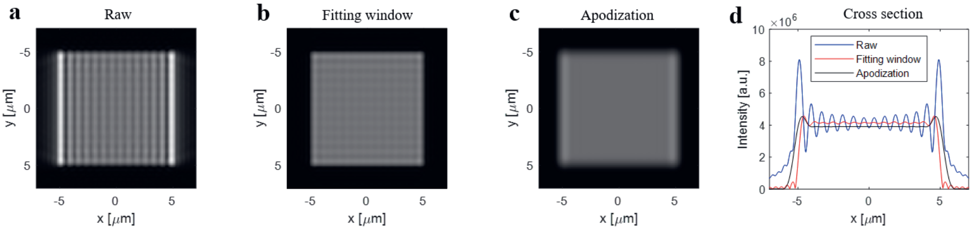

Figure 8.6: Simulated comparison of a 10 × 10 μm^2 grating with a 600 nm pitch and measurement wavelength 632 nm, using a raw, a fitting correction and an apodization window.

Fig. 8.6 shows a comparison between simulations of an unfiltered image (a), a filtered imaged using window fitting (b) and a conventional apodization window (c) (Hamming window). It is clearly visible that the bright edges of the grating are most effectively suppressed using a fitting window. Moreover, using a strong apodization window to suppress the zeroth order leakage will always be at the expense of resolution due to broadening of the point spread function.

Experimental result

We experimentally validated the approach as presented in previous section. Fig. 8.7 shows the experimental results of zeroth diffraction order separation and subtraction in the pupil plane.

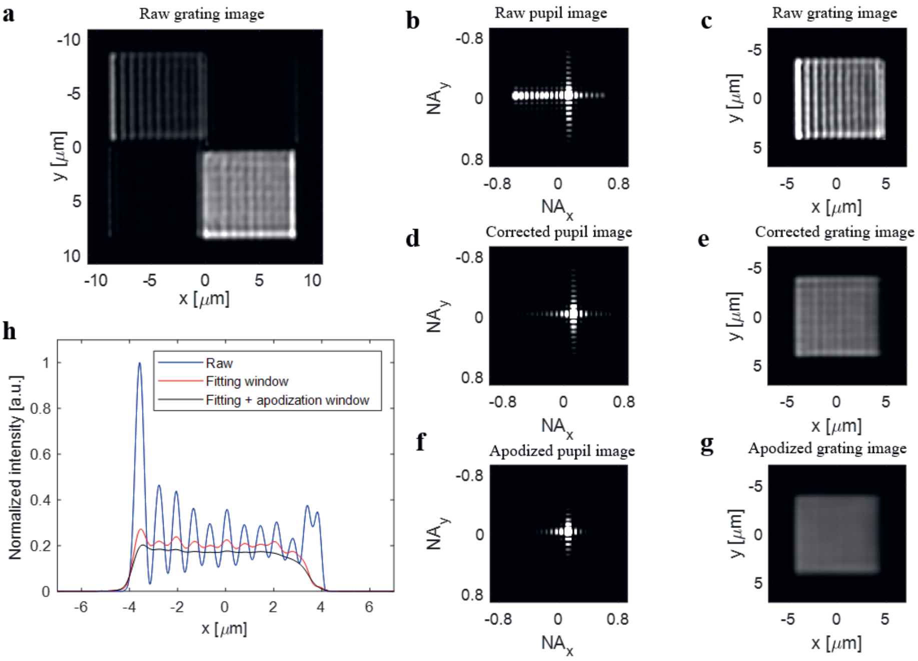

Figure 8.7: (a) A measured 16 × 16 μm^2 overlay target with a pitch of 600 nm measured at 632 nm wavelength. (b) The Fourier transform of a subset from (a) representing the exit pupil plane in. (c) A raw grating image of the inverse FFT (b). (d) A corrected pupil image using window fitting and its corresponding corrected image (e). (f) An hamming apodized window applied to the corrected pupil plane and its corresponding grating image (g). (h) A horizontal cross section of the grating image (c), (e) and (g).

The Fourier transform of the 16 x 16 μm^2 overlay target, (Fig. 8.7 (a)), results in two interfering sinc functions in the pupil plane amplitude. In order to simplify the fitting a subset of metrology target is selected in the image plane. The Fourier transform of the subset is now a simple single sinc function as shown in Fig. 8.7 (b). Here, the zeroth order leakage is visible in the left edge of the pupil plane and in the corresponding image plane, Fig. 8.7 (c), the zeroth order leakage is visible as clear bright lines at the edge of the grating. Moreover, an interference pattern with horizontal lines is visible in the image plane as a result of the interference between the zeroth and first diffraction order. Fitting a sinc function to the zeroth order tail results in a function that separates the zeroth order from the other signal. By subtracting the fitted zeroth order from the measured pupil plane we obtain a filtered pupil as depicted in Fig. 8.7 (d), and the corresponding image plane Fig. 8.7 (e). It is visible that after the zeroth diffraction order leakage is filtered out of the pupil plane the bright edge as well as the interference pattern on the target pad are gone. Only, the coherent Gibbs ringing is left which is then suppressed using a soft apodization window. Applying an soft apodization window (i.e. Hamming window) to the corrected pupil plane (Fig. (d)) results in Fig. 8.7 (f) and (g). This analyses can be repeated for the second subset of the metrology target. The cross sections of the raw, fitted window and fitted window with apodization window images are presented in Fig. 8.7 (h).

With the zeroth diffraction order suppression the target has a more homogeneous intensity distribution over the target and the bright edges a shown in Fig. 8.7 (h). This allows for a larger region-of-interest (RoI) selection inside the target and makes the RoI position less critical. An example of RoI selection is indicated with a red square in Fig. 8.8 (a). The overlay error as function of a square RoI size is presented in Fig. 8.8.

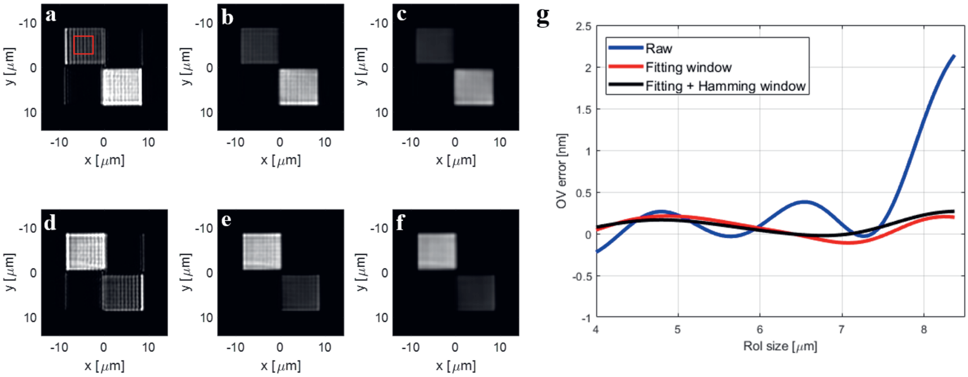

Figure 8.8: The $+1^{\mathrm{st}}$ (a), (b), (c) and -1^{st} (d), (e), (f) diffraction order of a 16×16 μm^2 overlay target with a pitch of 600 nm measured at 632 nm wavelength. (a) and (d) show the raw intensity images, where the red box indicated an example of a RoI selection. (b) and (e) have the zeroth diffraction order leakage filtered in the pupil plane using a fitting window. (c) and (f) have the zeroth diffraction order leakage filtered with an additional Hamming apodization window. (g) shows the calculated overlay error as function of RoI size for the three different cases.

Fig. 8.8 (g) shows the calculated overlay error, using Eq. 1.11 with $d = 20$ nm, as function of RoI size for the raw intensity images (blue), zeroth diffraction order corrected (red) and zeroth diffraction order corrected with an additional soft apodization window (black). The programmed overlay error of this test target equals 0 nm. The measured overlay error for the raw intensity varies 0.6 nm for a RoI size ranging from 4 μm to 7 µm due to the zeroth and first diffraction order interference. When the RoI becomes larger than 7.3 µm the overlay error increases up to 2.2 nm due to the bright target edge. With the zeroth diffraction order filtered using a fitting window in the pupil plane, the bright edge and interference pattern are removed from the signal resulting in a more homogeneous intensity, resulting in a more stable measured overlay error as function of RoI size as shown with the red curve. The residual low frequent oscillation is caused by Gibbs ringing due to the hard cut-off of the pupil edge. This can be suppressed by applying a soft apodization window, i.e. Hamming window. After filtering the pupil and applying an apodization window, the measured overlay error as function of RoI is stable within a range of 0.2 nm.

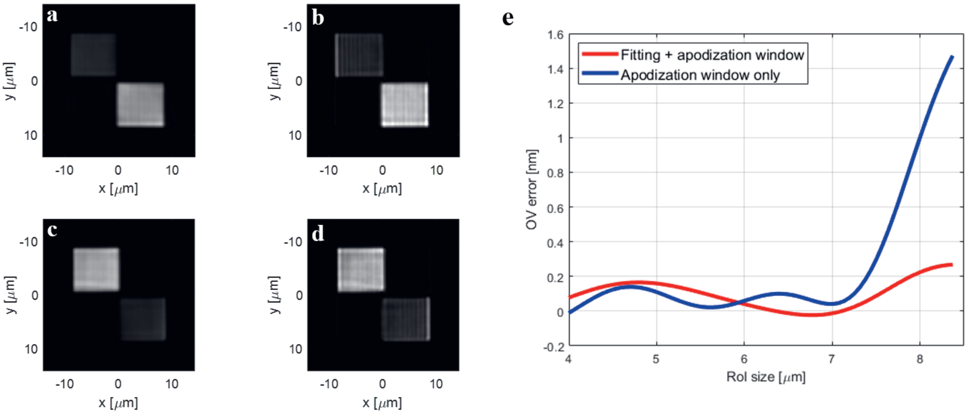

Figure 8.9: The $+1^{\text{st}}$, (a), (b) and -1^{st} (c), (d) diffraction order of a 16×16 µm^2 overlay target with a pitch of 600 nm measured at 632 nm wavelength. (a) and (b) show the measured $+1^{\text{st}}$ diffraction order of the overlay target with a fitting window combined with apodization and apodization only, respectively. (c) and (d) show this for the -1^{st} diffraction order. (e) overlay error as function of square RoI size, where red represents the fitting and Hamming apodization window combined and blue represents a Hamming apodization window only.

A comparison between zeroth diffraction order filtering in combination with apodization and conventional apodization only is presented in Fig. 8.9. (a) and (b) show the measured $+1^{\text{st}}$ diffraction order of the overlay target with a fitting window combined with apodization and apodization only, respectively. (c) and (d) show this for the -1^{st} diffraction order. The overlay error as function of square RoI size is presented in Fig. 8.9 (e). It shows that a conventional apodization window still suffers from zeroth diffraction order leakage, degrading the overlay measurement precision. Whereas, filtering the zeroth diffraction order using a fitting window allows for a larger RoI which becomes especially relevant for smaller (in-die) overlay targets.

Previous presented experimental results were obtained using on 16×16 µm^2 overlay targets. In order to verify that our zeroth order filtering method improves DBO metrology on small targets, 4×4 µm^2 overlay targets with two 2×2 µm^2 grating pairs, were measured. The pitch of the grating is 500 nm and measured with a wavelength of 532 nm. The retrieved overlay values as a function of the programmed overlay are plotted in Fig. 8.10. The blue dots represent the measurement points and the red line shows the linear fit through the retrieved overlay values. (a) represents the retrieved overlay where no zeroth order suppression was applied. Therefore, the RoI was chosen to be 1 × 1 µm^2, which is smaller than the target size. This results in slope of 1 with an offset of -11.8 nm. During this measurement no Tool Induced Shift (TIS) correction was applied, resulting in a constant offset. The relevant parameter here is the R^2 which is equal to 0.96. In Fig. 8.10 (b) the retrieved overlay plot is shown with zeroth order suppression applied and a RoI equal to 1 × 1 µm^2. The R^2 value slightly improved and is equal to 0.97. However, as presented in Fig. 8.8, filtering the zeroth diffraction order using a fitting window allows for a larger RoI selection. Therefore, in Fig. 8.10 (c) we show the retrieved overlay with the zeroth order filtered from the measurement and a RoI equal to the 2 × 2 µm^2 grating size. In this case, the R^2 value improves to 0.99, which is an indication for a more precise overlay measurement.

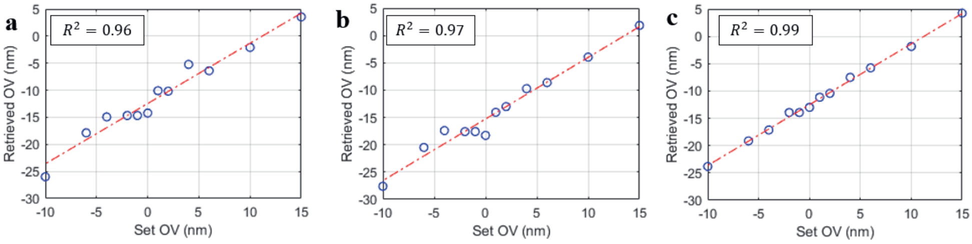

Figure 8.10: The retrieved overlay values measured on 4 × 4 µm^2 overlay targets with a pitch of 500 nm and a measurement wavelength of 532 nm. (a) without zeroth diffraction order filtering and a RoI smaller than the grating size (1 × 1 µm^2). (b) with zeroth diffraction order filtering and a RoI smaller than the grating size (1 × 1 µm^2). (c) with zeroth diffraction order filtering and a RoI equal to the grating size (2 × 2 µm^2).

In conclusion, we have shown that model-based digital pupil filtering allows for nuisance signal reduction resulting in a larger RoI that helps to improve the precision of overlay metrology on smaller targets.

8.3.2 Model-based suppression of the impact of surrounding structures

Metrology limitation

In addition to filtering nuisance signals from the target itself as presented in the previous section, we can also filter nuisance signals coming from structures that surround the target. Photons originating from bright surrounding structures next to the overlay metrology target can leak into the RoI, influencing the accuracy of the overlay measurement. Especially, when the RoI is equal to the grating size. Moreover, in coherent imaging systems like DHM, Gibbs ringing not only leads to degradation of the image quality but also increases the optical crosstalk, i.e. light leakage from surrounding structures into the metrology target. As explained in Section 2.2, an apodization window can suppress coherent ringing effects. However, when the surrounding has a different grating pitch than the overlay mark it will be asymmetrically suppressed due to the position in the pupil and the rotational symmetric origin of the apodization filter, resulting in undesired imaging artifacts. Here we will present first proof-of-concept experimental data that shows that we can also suppress the impact of surrounding structures using a model-based filtering approach.

Experimental result

We experimentally validate the model-based digital pupil filtering for suppression surrounding structure and present the results in Fig. 8.11. The measured sample is a single layer, custom-made test sample that contains two 8 × 8 μm^2 single layer gratings as target, having a pitch of 600 nm, and a 16 × 16 μm^2 bright surrounding target, with a pitch of 500 nm, next to it. A hologram is measured at 632 nm wavelength.

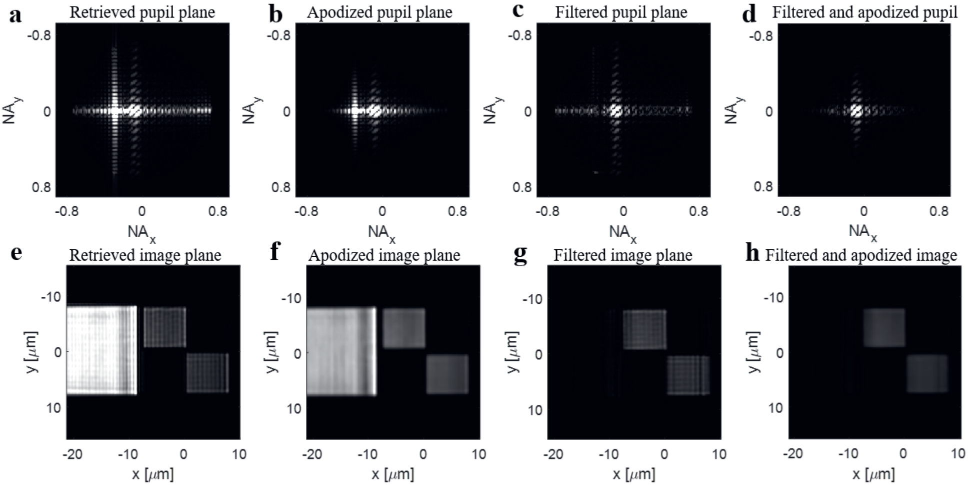

Figure 8.11: Surrounding suppression using fitting and subtraction in the pupil plane. (a) A retrieved pupil plane with a bright diffraction peak from the surrounding structure (left) and a second diffraction peak from the target (right) and its corresponding retrieved image plane (e). (b) Apodized pupil plane and its corresponding apodized image plane (f). (c) Filtered pupil plane and its corresponding filtered image plane (g). (d) Filtered pupil plane combined with a soft apodization window and its corresponding filtered image plane (h). The pitch of the surrounding target is 500 nm, the pitch of the target is 600 nm and measured using 632 nm wavelength.

Fig. 8.11 (a), shows the Fourier transform of the extracted image plane Fig. 8.11 (e). Due to the different pitches of the surrounding and overlay structures the diffraction orders end up at a different locations in the pupil plane. The left diffraction peak (Fig. 8.11 (a)) mainly contains the signal from the surrounding structure. Using the prior knowledge of the surrounding structure being a square, one can fit a 2D-sinc function to the diffraction peak in the Fourier plane. Subtraction of the fit from the pupil plane results in a filtered pupil plane, as shown in Fig. 8.11 (c) and its corresponding filtered image plane (g). Applying a soft Hamming window to the filtered pupil, as shown in Fig. 8.11 (d), results in a filtered image without coherent ringing (h).

This example shows that the unknown diffraction efficiency of the surrounding target can be compensated by fitting the amplitude in the pupil plane making use of the prior knowledge of the structure geometry. Therefore, the signal of the overlay target can be completely separated from the surrounding signals. A conventional apodization window only as presented in Fig. 8.11 (b) and the corresponding image plane (f) reduces the sidelobes and therefore the light leakage into the overlay target. However, apodization loses resolution and therefore the edges of the surrounding structure broaden as well and leak into the target structure. With the computational surrounding fitting method the field from the surrounding structure is completely filtered without the loss of resolution. Therefore, the optical crosstalk between neighboring structures is suppressed, which helps to improve metrology precision.

8.4 Conclusion

In conclusion, we demonstrated that in our DHM concept, where we retrieve the full complex field, we are able to separate signals of interest through model-based digital filtering in the pupil plane. We presented two experimental examples of different types of pupil filtering in DHM allowing for larger RoI selection to improve the DBO metrology precision and accuracy.

First, we demonstrated the zeroth order (i.e. specular reflection) suppression resulting in a reduction of the bright edges of an overlay target and the interference pattern inside the overlay target. This allows one to use a larger RoI inside the target and makes the RoI position less critical. Secondly, we presented a pupil filtering technique to separate the signal of interest from additional signal coming from surrounding structures. Therefore, the optical crosstalk leaking into the overlay target can be strongly suppressed.

To reach the sub-nm precision of overlay metrology we push the capabilities of computational imaging methods and DHM well beyond their existing boundaries. This study experimentally demonstrates that model-based signal separation in the pupil plane can significantly enhance the overlay metrology capabilities in cases where prior knowledge of the sample is present.

CHAPTER 9

CONCLUSIONS AND FUTURE PROSPECTS

In this chapter, we reflect on the investigations that have been reported in this thesis. We summarize the obtained results and place them in a broader context within the research field and we describe how this research has helped addressing some of the most relevant overlay metrology challenges in the semiconductor industry. In addition, we provide suggestions for further research directions toward new discoveries and we describe some potential applications.

Optical metrology has significantly evolved over the past few decades, with advances driven by developments in optics, laser sources, computational power, and precision engineering. Overlay metrology has evolved from basic alignment checks to a sophisticated, high-precision, and scatterometry measurement integrated into semiconductor manufacturing processes. Despite the significant progress in optical overlay metrology over the past decades, measurements still rely solely on the intensity information of light leading to stringent requirements for high quality optics and imaging. Therefore, digital holographic microscopy (DHM) was introduced as a potential novel overlay metrology tool measuring the full-complex field and solving hardware imperfection with computational imaging. The primary objective of this thesis was to tackle three major challenges of DHM as an overlay metrology tool, namely:

- Field-position dependent aberration correction
- Illumination spot profile correction
- Vibration mitigation

In this thesis, we demonstrated our capability to correct the non-isoplanatic lens aberrations in a computationally efficient manner through the co-design of a dedicated imaging lens and a three-step algorithmic approach. Secondly, to address the non-uniform beam profile illuminating the overlay target a computational correction method using calibration step was demonstrated. The third challenge, vibration sensitivity, was addressed by a computational vibration mitigation method using phase interpolation between a sequence of measured holograms. In the second part of this thesis, some less foreseen topics were covered:

- Field-position dependent apodization
- Model-based signal separation

Measurement results that show that the point-spread function of our microscope depends on the position in the Field-of-View. We showed that this novel observation can be explained by a combination of the finite bandwidth of the light source and a wavelength-dependent focal length of the imaging lens. Using a simple Fourier-transform spectrometer that accurately measures the spectrum of a quasi-monochromatic light source, we showed how measured spectral shapes can be used to computationally correct for such spurious apodization effects.

Lastly, in addition to the calibrated computational corrections, a model-based pupil filtering was discussed. We explored a model-based signal separation technique using digital pupil filtering for two different metrology challenges and demonstrate strong suppression of nuisance signals without resolution loss. This technique enables a further reduction in metrology target size while also offering opportunities to improve precision.

Besides the improvements in metrology target size, DHM might offer capabilities for optical depth profiling. In this thesis, overlay structures with a few hundred nanometer separation between top and bottom layer were measured. In more complex layer structures, the spacing might be several micrometers. Computational refocusing in combination with wavelength scanning might result in depth-resolved imaging for thick overlay targets using DHM. A next step would be to demonstrate the ability to reconstruct complex 3D structures, such as 3D MEMS with thicknesses that can reach 1 millimeter.

Secondly, imaging through a wide range of materials with varying optical properties in a multi-layer stack presents a promising application area for DHM. Its broad wavelength range, combined with coherent amplification, enables imaging through opaque layers. Ultimately, the ability to image through 700 µm of silicon unlocks a relatively unexplored domain for DHM, including metrology on thick stacks, bonded wafers, and backside alignment.

DHM generates large volumes of data that need to be translated into precise overlay measurements. Especially, multi-wavelength and multi-polarization holograms retrieved in one acquisition in combination with computational corrections and vibration mitigation methods might push computational load to its limits. Exploring model-based analyses and developing fast algorithms will be essential for DHM to evolve into a overlay metrology tool.

The high-NA EUV lithography scanners introduce thin photoresists, resulting in extremely weak scattering from the grating structures, posing unique overlay challenges. DHM, with its coherent amplification and adaptability to broad wavelength ranges, could enhance precision in high-NA EUV-driven layers. However, until now these thin resists layers are relatively unexplored with DHM. Lastly, suppressing nuisance signals from high-reflectivity interfaces and surrounding structures remains a key topic for future investigation. In this thesis, signal filtering of two known structures was experimentally validated. Expanding this work to model-based filtering techniques for scenarios where the surrounding structures are unknown presents a promising area for further research.

In Chapter 1, we discussed the growing demands that semiconductor industry faces for metrology precision, speed, and efficiency as feature sizes shrink and device complexity grows. This thesis contributes directly to addressing these challenges by advancing DHM as an overlay metrology tool. In modern semiconductor manufacturing, where extremely high precision is required, field-position dependent aberrations are a fundamental limitation in conventional imaging systems. This thesis provides a groundbreaking solution to address field-dependent aberrations computationally using DHM. A three-step algorithmic approach, combined with a co-designed lens system, enables efficient correction of non-isoplanatic aberrations without the need for expensive hardware modifications. This opens the door to improved performance and reduced costs, which are essential for advancing the next generation metrology techniques. Moreover, this thesis demonstrated a model-based signal separation technique enabling a further reduction in metrology target size while also offering opportunities to improve precision. The value for industry comes on one hand with the model-based signal separation and on the other hand with the computational access to the pupil plane of the digital holographic microscope, resulting in a complete suppression of nuisance signals without the loss of resolution improving metrology performance on small targets. A unique combination that the semiconductor industry is searching for for decades.

C. A. Bennet quotes in his book Principles of Physical Optics: *"In principle, holography is very simple"* [75]. It is indeed true that the concept of holography is relatively straightforward. However, the well-known idiom "the devil is in the details" applies when DHM is being considered for overlay metrology. Measuring signal levels with 0.01% precision is far from trivial and requires a deep and detailed understanding of the DHM signal formation. The work reported in this thesis is a significant step forward in gaining this understanding and has brought DHM a step closer towards an overlay metrology application.

SUMMARY

In semiconductor industry, integrated circuits are manufactured on wafers, built up layer-by-layer, resulting in a complex multilayer stack. In order for a chip to work properly after manufacturing, each layer should be positioned with sub-nanometer accuracy relative to the previous layer. This positioning is called overlay, which is the lateral misalignment of a newly patterned layer with respect to the previous layer in a multilayer stacked wafer. With the continued shrink of device feature sizes and more complex devices being developed, there has been a relentless push for semiconductor overlay metrology improvements for accurate, precise, and fast overlay measurements. In this thesis, the potential of dark-field digital holographic microscopy as an overlay metrology tool is explored. Digital holographic microscopy enables the reconstruction of complex fields, allowing for computational corrections of imperfections in the imaging system. In this study, six key challenges are addressed. The questions explore the major difficulties of digital holographic microscopy, its practical implementation, and its potential to meet the demanding requirements of advanced semiconductor metrology.

In Chapter 2, the experimental setup is discussed, which incorporates a supercontinuum light source, acousto-optical tunable filter, and polarization-maintaining fibers. The imaging system includes a high-NA lens without anti-reflective coatings. Specific design features like off-axis illumination and Fourier transform techniques for processing interference patterns are explained. The setup is extended to the near-infrared range using tailored optics and cameras, demonstrating it's applicability to a broader range of semiconductor materials.

In Chapter 3, we demonstrate a solution for the first foreseen challenge of digital holographic microscope: field-position dependent aberrations. A fast and accurate correction of non-isoplanatic aberrations over a wavelength range from visible to near-infrared is experimentally shown. This is done computationally in an efficient manner through co-design of a dedicated imaging lens and a three-step algorithmic approach.

In Chapter 4, we address the challenge of illumination spot profile inhomogeneity, caused by the Gaussian spot in combination with the oblique angle of incidence. A

large grating, covering the entire Field-of-View is used as calibration step to measure the spot profile. A computational correction on measured data, using this calibrated spot profile, demonstrate significant improvements in overlay measurements, reducing errors caused by uneven illumination.

In Chapter 5, a computational approach to mitigate phase variations from environmental vibrations is introduced. By measuring a sequence of holograms using a high-speed camera, the phase variation during acquisition time can be interpolated. It was shown that based on this phase interpolation the impact of the vibrations on the amplitude can be predicted and corrected.

In Chapter 6, spurious apodization effects caused by wavelength-dependent focal depth in combination with a finite bandwidth of the light source was examined. Both theoretical and experimental analyses were conducted to understand how this spurious apodization affect the point-spread function and thereby the image quality. The chapter was concluded by proposing a computational correction method which was investigated in Chapter 7.

In Chapter 7, a Fourier-transform spectrometer is built, measuring the spectrum of the light source accurately to address the spurious apodization in our digital holographic microscope. We concluded the study with experimental work on spurious apodization correction and an acousto-optical tunable filter characterization.

In Chapter 8, computational image enhancement was experimentally explored resulting in a model-based signal separation technique using digital pupil filtering for two different metrology challenges. It demonstrates strong suppression of nuisance signals without resolution loss. This technique enables a further reduction in metrology target size while also offering opportunities to improve precision.

SAMENVATTING

In de halfgeleiderindustrie worden geïntegreerde curcuits gemaakt op wafers, deze wafers worden laag voor laag opgebouwd, wat resulteert in een complexe structuur bestaande uit meerdere lagen. Om ervoor te zorgen dat een chip na fabricage goed functioneert, moet elke laag met sub-nanometerprecisie ten opzichte van de vorige laag worden gepositioneerd. Een verschuiving in deze positionering wordt overlay genoemd, wat verwijst naar de laterale uitlijning van een nieuwe laag ten opzichte van een vorige laag in de wafer structuur. Met chip structuren die voortdurend kleiner worden en de ontwikkeling van complexere chips, is er in de halfgeleiderindustrie een aanhoudende druk om overlay metrologie te verbeteren in termen van nauwkeurigheid, precisie en snelheid. In dit proefschrift wordt dark-field digitale holografische microscopie onderzocht als een mogelijkheid voor overlay metrologie. Digitale holografische microscopie maakt het mogelijk om complexe lichtvelden te reconstrueren, waardoor het computationeel corrigeren van imperfecties in het systeem mogelijk wordt. In dit onderzoek worden zes belangrijke uitdagingen aangepakt. Hierbij wordt gekeken naar de grootste uitdagingen, de praktische implementatie ervan en om te voldoen aan de veeleisende doelstellingen van de halfgeleider industrie.

In Hoofdstuk 1, wordt een overzicht gegeven van bestaande methodes voor overlay metrologie, zoals image-based overlay (IBO) en diffraction-based overlay (DBO), waarbij de beperkingen worden besproken. De potentie van dark-field digitale holografische microscopie als een nieuw instrument voor metrologie wordt besproken. Digitale holografische microscopie biedt veel voordelen zoals coherente optische signaal versterking, aberratiecorrectie en computationele beeldverbetering.

In Hoofdstuk 2, wordt de experimentele opstelling besproken, met daarin een supercontinuum lichtbron, een acoustic optical tunable filter (AOTF) en polarisatiehoudende fiber. Het beeldvormingssysteem omvat een lens met een hoge numerieke apertuur zonder antireflectie-coatings. Specifieke ontwerp keuzes zoals de off-axis verlichting en Fourier-transformatietechnieken voor het verwerken van interferentiepatronen worden uitgelegd. De opstelling wordt uitgebreid naar het infrarood bereik met behulp van extra optica en camera's, wat de toepasbaarheid op een breder scala aan

halfgeleidermaterialen aantoont.

In Hoofdstuk 3, wordt een oplossing gepresenteerd voor een van de eerste uitdagingen van digitale holografische microscopie: veldpositie-afhankelijke aberraties. Een snelle en nauwkeurige correctie van niet-isoplanatische aberraties over een golflengtebereik van zichtbaar licht tot infrarood wordt experimenteel aangetoond. Dit wordt op een computationeel efficiënt manier gedaan via een co-ontwerp van een speciale lens en een algoritmische aanpak in drie stappen.

In Hoofdstuk 4, wordt het probleem van de inhomogeniteit in de verlichtings spot aangepakt, veroorzaakt door de Gaussische spot in combinatie met de schuine invalshoek. Een groot grating dat het gehele Field-of-View omvat, wordt gebruikt als kalibratiestap om de verlichtings spot te meten. Een computationele correctie, gebruik makend van de gekalibreerde spot, laat aanzienlijke verbeteringen zien in overlay metingen en vermindert fouten als gevolg van ongelijke verlichting.

In Hoofdstuk 5, introduceren we een computationele aanpak om fasevariaties door vibraties uit de omgeving te corrigeren. Door een reeks hologrammen met een hogesnelheidscamera te meten, kan de fasevariatie tijdens de acquisitietijd worden geïnterpoleerd. Dit maakt het mogelijk om de invloed van vibraties op de amplitude te voorspellen en te corrigeren.

In Hoofdstuk 6, wordt het apodizatie-effect onderzocht die wordt veroorzaakt door golflengteafhankelijke focus diepte in combinatie met de eindige bandbreedte van de lichtbron. Zowel theoretische als experimentele analyses worden uitgevoerd om te begrijpen hoe deze effecten de point-spread function en daarmee de beeldkwaliteit beïnvloeden. Het Hoofdstuk wordt afgesloten met een voorstel voor een computationele correctiemethode, die verder wordt onderzocht in Hoofdstuk 7.

In Hoofdstuk 7, wordt een Fourier-transformspectrometer beschreven, waarmee het spectrum van de lichtbron nauwkeurig wordt gemeten om de spurious apodization in het digitale holografische microscoop te corrigeren. Experimenteel werk over deze correctie en de karakterisatie van de AOTF wordt gepresenteerd.

In Hoofdstuk 8, wordt computationele beeldverbetering in DHM experimenteel onderzocht. Dit resulteert in een filter methode in het pupil vlak gebruikmakend van een model. Deze techniek toont een sterke onderdrukking van ruissignalen zonder verlies van resolutie. Dit maakt een verdere verkleining van metrologie structuren mogelijk en biedt kansen om de precisie te verbeteren.

REFERENCES

[1] W. Kelvin, *Popular Lectures and Addresses,* Macmillan and Company, 1889.

[2] D. W. Price and D. G. Sutherland, *A fundamental truth of process control,* Solid State technology **57**, 34 (2014).

[3] A. J. den Boef, *Optical wafer metrology sensors for process-robust CD and overlay control in semiconductor device manufacturing,* Surface Topography: Metrology and Properties **4**, 023001 (2016).

[4] T. C. Tin, S. C. Tan, H. Yong, J. O. H. Kim, E. K. Y. Teo, C. K. Lee, P. Than, A. P. S. Tan, and S. C. Phang, *A Realizable Overlay Virtual Metrology System in Semiconductor Manufacturing: Proposal, Challenges and Future Perspective,* IEEE Access **9**, 65418 (2021).

[5] G. Saavedra, M. Martinez-Corral, J. I. Garcia-Sucerquia, E. Sanchez-Ortiga, and A. Doblas, *Recent Advances in Digital Holographic Microscopy,* in *2018 20th International Conference on Transparent Optical Networks (ICTON),* pages 1–4, 2018.

[6] J. Picazo-Bueno, J. García, and V. Micó, *Single-Element Reflective Digital Holographic Microscopy,* Frontiers in Physics **9** (2021).

[7] M. Kim, *Principles and techniques of digital holographic microscopy,* SPIE Reviews, Volume 1, id. 018005 (2010). **1**, 8005 (2009).

[8] J. Xu, L. Qin, Q. Chen, H. Zhi, Y. Wang, Z. Yang, and Z. Mao, *Diffraction-based and image-based overlay evaluation for advanced technology node,* in *2017 China Semiconductor Technology International Conference (CSTIC),* pages 1–4, 2017.

[9] C.-M. Ke, G.-T. Huang, J. Huang, and R. Lee, *Accuracy of diffraction-based and image-based overlay,* in *Metrology, Inspection, and Process Control for Microlithography XXV,* edited by C. J. Raymond, volume 7971, page 79711E, International Society for Optics and Photonics, SPIE, 2011.

[10] P. L. Rigolli, L. Rozzoni, C. Turco, U. Iessi, M. Polli, E. Kassel, P. Izikson, and Y. Avrahamov, *AIM technology for nonvolatile memories microelectronics devices,* in *Metrology, Inspection, and Process Control for Microlithography XX,* edited by C. N. Archie, volume 6152, page 61524C, International Society for Optics and Photonics, SPIE, 2006.

[11] P. Leray, S. Y. Cheng, D. Kandel, M. Adel, A. Marchelli, I. Vakshtein, M. Vasconi, and B. Salski, *Diffraction based overlay metrology: accuracy and performance on front end stack,* in *SPIE Advanced Lithography,* 2008.

[12] W. Yang, R. Lowe-Webb, S. Rabello, J. Hu, J.-Y. Lin, J. D. Heaton, M. V. Dusa, A. J. den Boef, M. van der Schaar, and A. Hunter, *Novel diffraction-based spectroscopic method for overlay metrology,* in *Metrology, Inspection, and Process Control for Microlithography XVII,* edited by D. J. Herr, volume 5038, pages 200 – 207, International Society for Optics and Photonics, Proceeding SPIE, 2003.

[13] M. Adel, D. Kandel, V. Levinski, J. Seligson, and A. Kuniavsky, *Diffraction order control in overlay metrology: a review of the roadmap options,* in *Metrology, Inspection, and Process Control for Microlithography XXII,* edited by J. A. Allgair and C. J. Raymond, volume 6922, pages 23 – 41, International Society for Optics and Photonics, Proceeding SPIE, 2008.

[14] D. Swinkels, *Spectral shaping for the next-generation overlay metrology,* Master's thesis, Eindhoven University of Technology, 2021.

[15] J. Mulkens, B. Slachter, M. Kubis, W. Tel, P. Hinnen, M. Maslow, H. Dillen, E. Ma, K. Chou, X. Liu, W. Ren, X. Hu, F. Wang, and K. Liu, *Holistic approach for overlay and edge placement error to meet the 5nm technology node requirements,* in *Metrology, Inspection, and Process Control for Microlithography XXXII,* edited by V. A. Ukraintsev, volume 10585, page 105851L, International Society for Optics and Photonics, SPIE, 2018.

[16] N. Smith, B. Peterson, and G. Goelzer, *Size matters in overlay measurement,* Proceedings of SPIE - The International Society for Optical Engineering **8324**, 40 (2012).

[17] A. Salerno, I. de la Fuente, Z. Hsu, A. Tai, and H. Chang, *Diffraction order control in overlay metrology: a review of the roadmap options,* in *Proceedings of SPIE 10585, Metrology, Inspection, and Process Control for Microlithography XXXII, San Jose, California, United States,* SPIE, 2008.

[18] J. Du, F. Dai, Y. Bu, and X. Wang, *Calibration method of overlay measurement error caused by asymmetric mark,* Appl. Opt. **57**, 9814 (2018).

[19] D. Gabor, *A New Microscopic Principle,* Nature **161**, 777 (1948).

[20] W. L. Bragg and G. L. Rogers, *Elimination of the Unwanted Image in Diffraction Microscopy,* Nature **167**, 190 (1951).

[21] E. N. Leith and J. Upatnieks, *Reconstructed Wavefronts and Communication Theory,* Journal of the Optical Society of America **52**, 1123 (1962).

[22] J. Goodman and R. Lawrence, *Digital image formation from electronically detected holograms,* Applied Physics Letters **11**, 77 (1967).

[23] M. Yaroslavsky and Leonid, *Methods of digital holography,* Consultants Bureau, New York, 1980.

[24] R. S. W. O. "Peter J. de Groot", "Leslie L. Deck", *Contributions of holography to the advancement of interferometric measurements of surface topography,* 2022.

[25] J. W. Goodman, *Introduction to Fourier optics,* Introduction to Fourier optics, 3rd ed., by JW Goodman. Englewood, CO: Roberts & Co. Publishers, 2005 **1** (2005).

[26] C. Messinis, *Diffraction-based overlay metrology using angular-multiplexed acquisition of dark-field digital holograms,* Optics Express **28**, 37419 (2020).

[27] J. Liesener, X. Colonna de Lega, and P. d. Groot, *Interferometer for determining overlay errors,* 2012.

[28] A. Doblas, E. Sánchez-Ortiga, M. Martínez-Corral, and J. Garcia-Sucerquia, *Study of spatial lateral resolution in off-axis digital holographic microscopy,* Optics Communications **352**, 63 (2015).

[29] P. Leray, S. Cheng, D. Laidler, D. Kandel, M. Adel, B. Dinu, M. Polli, M. Vasconi, and B. Salski, *Overlay metrology for double patterning processes,* volume 7272, SPIE, 2009.

[30] H. Levinson, *Metrology requirements for lithography's next wave,* SPIE, 2004.

[31] N. Sullivan and J. Shin, *Overlay metrology: the systematic, the random and the ugly,* volume 449, pages 502–512, 1998.

[32] I. nigo Molina-Fernández, J. Leuermann, A. O.-M. nux, J. G. Wangüemert-Pérez, and R. Halir, *Fundamental limit of detection of photonic biosensors with coherent phase read-out,* Opt. Express **27**, 12616 (2019).

[33] P. J. Vidal-Moreno, C. Becerril, M. R. Fernández-Ruiz, H. Martins, S. Martin-Lopez, and M. Gonzalez-Herraez, *Noise analysis in direct detection and coherent detection phase-sensitive optical time-domain reflectometry systems,* Opt. Express **31**, 27450 (2023).

[34] D. Fink, *Coherent Detection Signal-to-Noise,* Appl. Opt. **14**, 689 (1975).

[35] T. van Gardingen-Cromwijk, S. Konijnenberg, W. Coene, M. Adhikary, T. Tukker, S. W. F., de Boer, and A. den Boef, *Non-isoplanatic lens aberration correction in dark-field digital holographic microscopy for semiconductor metrology,* Light: Advanced Manufacturing **4**, 453 (2023).

[36] S. Kim, U.-g. Kim, J. Ryu, D. Kim, M. Kim, Y.-C. Joo, and S.-Y. Lee, *Boron-doped amorphous carbon deposited by DC sputtering for a hardmask: Microstructure and dry etching properties,* Applied Surface Science **637**, 157895 (2023).

[37] F. Dubois and P. Grosfils, *Dark-field digital holographic microscopy to investigate objects that are nanosized or smaller than the optical resolution,* Optics letters **33**, 2605 (2008).

[38] F. Verpillat, F. Joud, P. Desbiolles, and M. Gross, *Dark-field digital holographic microscopy for 3D-tracking of gold nanoparticles,* Optics Express **19**, 26044 (2011).

[39] C. Trujillo and J. Garcia-Sucerquia, *Numerical dark field illumination applied to experimental digital lensless holographic microscopy for reconstructions with enhanced contrast,* Optics letters **17**, 4096 (2018).

[40] M. Trusiak, J.-A. Picazo-Bueno, P. Zdankowski, and V. Micó, *DarkFocus: numerical autofocusing in digital in-line holographic microscopy using variance of computational dark-field gradient,* Optics and Lasers in Engineering **134**, 106195 (2020).

[41] C. Larivière-Loiselle, E. Bélanger, and P. Marquet, *Polychromatic digital holographic microscopy: a quasicoherent-noise-free imaging technique to explore the connectivity of living neuronal networks,* Neurophotonics **7**, 040501 (2020).

[42] J. Kühn, F. Charrière, T. Colomb, E. Cuche, F. Montfort, Y. Emery, P. Marquet, and C. Depeursinge, *Axial sub-nanometer accuracy in digital holographic microscopy,* Measurement Science and Technology **19**, 074007 (2008).

[43] A. Fontbonne, H. Sauer, and F. Goudail, *How to integrate digital post-processing algorithms in professional optical design software for co-designing complex optical systems?,* in *Proceedings of SPIE 11871, Optical Design and Engineering VIII*, page 118710P, SPIE, 2021.

[44] L. Denis, É. Thiébaut, F. Soulez, J.-M. Becker, and R. Mourya, *Fast Approximations of Shift-Variant Blur,* International Journal of Computer Vision **115**, 253 (2015).

[45] S. Mathijssen, M. Noot, M. Bozkurt, N. Javaheri, R. Hajiahmadi, A. Zagaris, K. Chang, B. Gosali, E. Su, C. Wang, A. den Boef, K. Bhattacharyya, G.-T. Huang, K.-H. Chen, and J. Lin, *Color mixing in overlay metrology for greater accuracy and robustness,* in *Proceedings of SPIE 10959, Metrology, Inspection, and Process Control for Microlithography XXXIII, San Jose, California, United States*, page 109591G, SPIE, 2019.

[46] J. Sasián, *Introduction to Aberrations in Optical Imaging Systems,* chapter 5, Cambridge University Press, 2012.

[47] C. Messinis, T. van Schaijk, N. Pandey, A. Koolen, I. Shlesinger, X. Liu, S. Witte, J. Boer, and A. Boef, *Aberration Calibration and Correction with Nano-scatterers in Digital Holographic Microscopy for Semiconductor Metrology,* Optics Express **29** (2021).

[48] R. J. M. Zwiers and G. C. M. Dortant, *Aspherical lenses produced by a fast high-precision replication process using UV-curable coatings,* Appl. Opt. **24**, 4483 (1985).

[49] E. J. K. Verstegen, J. H. P. Faasen, H. R. Stapert, P. C. Duineveld, and J. G. Kloosterboer, *Influence of the reaction mechanism on the shape accuracy of optical components obtained by photoreplication,* Journal of Applied Polymer Science **90**, 2364 (2003).

[50] K. Strehl, *Aplanatische und fehlerhafte Abbildung im Fernrohr,* Zeitschrift für Instrumentenkunde **15**, 362 (1895).

[51] D. M. Alloin and J. M. Mariotti, *Adaptive Optics for Astronomy,* Dordrecht: Kluwer Academic Publishers (1994).

[52] H. Ottevaere and H. Thienpont, *Optical Microlenses,* in *Encyclopedia of Modern Optics*, edited by R. D. Guenther, pages 21–43, Elsevier, Amsterdam, 2005.

[53] S. Paolillo, D. Wan, F. Lazzarino, N. Rassoul, D. Piumi, and Z. Tőkei, *Direct metal etch of ruthenium for advanced interconnect,* Journal of Vacuum Science & Technology B **36** (2018).

[54] R. Dändliker, E. Marom, and F. M. Mottier, *Two-reference-beam holographic interferometry,* J. Opt. Soc. Am. **66**, 23 (1976).

[55] N. Verrier and M. Atlan, *Off-axis digital hologram reconstruction: some practical considerations,* Appl. Opt. **50**, H136 (2011).

[56] T. van Gardingen-Cromwijk, M. Adhikary, C. Messinis, S. Konijnenberg, W. Coene, S. Witte, J. F. de Boer, and A. den Boef, *Field-position dependent apodization in dark-field digital holographic microscopy for semiconductor metrology,* Opt. Express **31**, 411 (2023).

[57] K. Bhattacharyya, A. den Boef, M. Noot, O. Adam, G. Grzela, A. Fuchs, M. Jak, S. Liao, K. Chang, V. Couraudon, E. Su, W. Tzeng, C. Wang, C. Fouquet, G.-T. Huang, K.-H. Chen, Y. C. Wang, K. Cheng, C.-M. Ke, and L. G. Terng, *A complete methodology towards accuracy and lot-to-lot robustness in on-product overlay metrology using flexible wavelength selection,* in *Metrology, Inspection, and Process Control for Microlithography XXXI*, edited by M. I. Sanchez, volume 10145, page 101450A, International Society for Optics and Photonics, SPIE, 2017.

[58] A. Quirrenbach, *The development of astronomical interferometry,* Experimental Astronomy **26**, 49 (2009).

[59] D. Nolte, *Optical Interferometry for Biology and Medicine,* 2012.

[60] R. Smythe, *Practical aspects of modern interferometry for optical manufacturing quality control: Part 2,* Advanced Optical Technologies **1**, 203 (2012).

[61] S. Nakadate, *Vibration measurement using phase-shifting time-average holographic interferometry,* Appl. Opt. **25**, 4155 (1986).

[62] P. de Groot, *Vibration in phase-shifting interferometry,* Journal of The Optical Society of America A-optics Image Science and Vision **12** (1995).

[63] K. A. Stetson and R. L. Powell, *Interferometric Hologram Evaluation and Real-Time Vibration Analysis of Diffuse Objects,* J. Opt. Soc. Am. **55**, 1694 (1965).

[64] S. Nakadate, *Vibration measurement using phase-shifting time-average holographic interferometry,* Appl. Opt. **25**, 4155 (1986).

[65] A. Hettwer, J. Kranz, and J. Schwider, *Three channel phase-shifting interferometer using polarization-optics and a diffraction grating,* Optical Engineering **39**, 960 (2000).

[66] J. L. McLaughlin and B. A. Horwitz, *Real-Time Snapshot Interferometer,* in *Surface Characterization and Testing,* edited by K. Creath, volume 0680, pages 35 – 43, International Society for Optics and Photonics, SPIE, 1987.

[67] J. Millerd, N. Brock, J. Hayes, M. North-Morris, B. Kimbrough, and J. Wyant, *Pixelated Phase-Mask Dynamic Interferometers,* in *Fringe 2005,* edited by W. Osten, pages 640–647, Berlin, Heidelberg, 2006, Springer Berlin Heidelberg.

[68] U. Grenander, *Probability and Statistics: The Harald Cramér Volume,* Wiley publications in statistics, Almqvist & Wiksell, 1959.

[69] C. Messinis, V. Tenner, J. Boer, S. Witte, and A. Boef, *Impact of coherence length on the field of view indark-field holographic microscopy for semiconductormetrology: theoretical and experimental comparisons,* Applied Optics **59** (2020).

[70] G. Fowles, *Introduction to modern optics,* chapter 3, Dover Publications, 1989.

[71] T. van Schaijk, C. Messinis, N. Pandey, A. Koolen, S. Witte, J. Boer, and A. Boef, *Diffraction-based overlay metrology from visible to infrared wavelengths using a single sensor,* Journal of Micro/Nanopatterning, Materials, and Metrology **21** (2022).

[72] K. Bhattacharyya, A. den Boef, G. Storms, J. van Heijst, M. Noot, K. An, N.-K. Park, S.-R. Jeon, N.-L. Oh, E. McNamara, F. van de Mast, S. Oh, S. Y. Lee, C. Hwang, and K. Lee, *A study of swing-curve physics in diffraction-based overlay,* in *Metrology, Inspection, and Process Control for Microlithography XXX,* edited by M. I. Sanchez, volume 9778, page 97781I, International Society for Optics and Photonics, Proceeding SPIE, 2016.

[73] K. Bhattacharyya, M. Noot, H. Chang, S. Liao, K. Chang, B. Gosali, E. Su, C. Wang, A. den Boef, C. Fouquet, G.-T. Huang, K.-H. Chen, K. Cheng, and J. Lin, *Multi-wavelength approach towards on-product overlay accuracy and robustness,* in *Metrology, Inspection, and Process Control for Microlithography XXXII,* edited by V. A. Ukraintsev, volume 10585, page 105851F, International Society for Optics and Photonics, Proceeding SPIE, 2018.

[74] K. Bhattacharyya, A. den Boef, M. Noot, O. Adam, G. Grzela, A. Fuchs, M. Jak, S. Liao, K. Chang, V. Couraudon, E. Su, W. Tzeng, C. Wang, C. Fouquet, G.-T. Huang, K.-H. Chen, Y. C. Wang, K. Cheng, C.-M. Ke, and L. G. Terng, *A complete methodology towards accuracy and lot-to-lot robustness in on-product overlay metrology using flexible wavelength selection,* in *Metrology, Inspection, and Process Control for Microlithography XXXI,* edited by M. I. Sanchez, volume 10145, page 101450A, International Society for Optics and Photonics, Proceeding SPIE, 2017.

[75] C. Bennett, *Principles of Physical Optics,* Wiley, 2022.

[76] T. van Gardingen-Cromwijk, M. Adhikary, C. Messinis, S. Konijnenberg, W. Coene, S. Witte, J. F. de Boer, and A. den Boef, *Field-position dependent apodization in dark-field digital holographic microscopy for semiconductor metrology,* Optics Express **31**, 411 (2023).

[77] A. Mahieux, V. Wilquet, R. Drummond, D. Belyaev, A. Federova, and A. Vandaele, *A new method for determining the transfer function of an Acousto optical tunable filter,* Opt. Express **17**, 2005 (2009).

[78] G. Georgiev, D. A. Glenar, and J. J. Hillman, *Spectral characterization of acousto-optic filters used in imaging spectroscopy,* Appl. Opt. **41**, 209 (2002).

[79] C. Stedham, M. Draper, J. Ward, E. Wachman, and C. Pannell, *A novel acousto-optic tunable filter for use in hyperspectral imaging systems,* in *Physics and Simulation of Optoelectronic Devices XVI,* edited by M. Osinski, F. Henneberger, and K. Edamatsu, volume 6889, page 68891C, International Society for Optics and Photonics, SPIE, 2008.

[80] E. G. Bucher and J. W. Carnahan, *Characterization of an Acousto-optic Tunable Filter and Use in Visible Spectrophotometry,* Appl. Spectrosc. **53**, 603 (1999).

[81] T. Young, *I. The Bakerian Lecture. Experiments and calculations relative to physical optics,* Philosophical transactions of the Royal Society of London , 1 (1804).

[82] A. den Boef, P. van Schaijk, I. Setija, T. Cromwijk, and M. Adhikary, *Method and apparatuses for fourier transform spectrometry,* 2024, WIPO International Application No. PCT/EP2023/067754.

[83] S. N. Mantsevich, V. I. Balakshy, K. B. Yushkov, V. Y. Molchanov, and S. A. Tretiakov, *Quasi-Collinear AOTF Spectral Transmission Under Temperature Gradients Aroused by Ultrasound Power Absotption,* IEEE Transactions on Ultrasonics, Ferroelectrics, and Frequency Control **69**, 3411 (2022).

[84] A. Korpel, *Acousto-optics,* volume 57, CRC Press, 1996.

[85] X. Niu, N. Jakatdar, J. Bao, and C. J. Spanos, *Specular spectroscopic scatterometry,* IEEE Transactions on Semiconductor Manufacturing **14**, 97 (2001).

[86] S. Mathijssen, M. Noot, M. Bozkurt, N. Javaheri, R. Hajiahmadi, A. Zagaris, K. Chang, B. Gosali, E. Su, C. Wang, A. den Boef, K. Bhattacharyya, G.-T. Huang, K.-H. Chen, and J. Lin, *Color mixing in overlay metrology for greater accuracy and robustness*, in *Metrology, Inspection, and Process Control for Microlithography XXXIII*, edited by V. A. Ukraintsev and O. Adan, volume 10959, page 109591G, International Society for Optics and Photonics, SPIE, 2019.

[87] F. Harris, *On the use of windows for harmonic analysis with the discrete Fourier transform*, Proceedings of the IEEE **66**, 51 (1978).

[88] C. Messinis, *Dark-Field Digital Holographic Microscopy For Advanced Semiconductor Metrology*, Phd-thesis - research and graduation internal, Vrije Universiteit Amsterdam, 2022.

CURRICULUM VITAE

Tamar Cromwijk was born on 26 February 1998, in Best, the Netherlands. She obtained her secondary education at the Heerbeeck College in Best in 2016. Thereafter, in 2016, she started studying Applied Physics at the Eindhoven University of Technology (TU/e). In 2021 she obtained her Master degree with a research profile in nano-physics. She did her master thesis under the supervision of prof. B. Koopmans on functionalized probes for magnetic-force microscopy. In december 2021 she started her PhD in the Computational Imaging group at the Advanced Research Center for Nanolithography (ARCNL), under the supervision of prof. A. den Boef on dark-field digital holographic microscopy for advanced semiconductor metrology. The outcomes of this research are described in this thesis.

LIST OF PUBLICATIONS

1. Pupil apodization in digital holographic microscopy for reduction of coherent imaging effects,
   C. Messinis, M. Adhikary, T. van Gardingen-Cromwijk, T.M.M. van Schaijk, S. Witte, J. F. de Boer and A. den Boef, *Opt. Continuum* **1**, 1202 (2022).
2. Field-position dependent apodization in dark-field digital holographic microscopy for semiconductor metrology,
   T. van Gardingen-Cromwijk, M. Adhikary, C. Messinis, S. Konijnenberg, W. Coene, S. Witte, J.F. de Boer and A. den Boef, *Opt. Express* **31**, 411 (2023).
3. Non-isoplanatic lens aberration correction in dark-field digital holographic microscopy for semiconductor metrology,
   T. van Gardingen-Cromwijk, S. Konijnenberg, W. Coene, M. Adhikary, T. Tukker, S. Witte, J. F. de Boer and A. den Boef, *Light: Advanced Manufacturing* **4**, 453 (2023).
4. Illumination spot profile correction in digital holographic microscopy for overlay metrology,
   M. Adhikary, T. van Gardingen-Cromwijk, de Wit, S. Witte, J.F. de Boer and A.J. den Boef, *J. Micro/Nanopattern. Mats. Metro* **22**, 024001 (2023).
5. Computational vibration mitigation using phase interpolation in digital holographic microscopy for overlay metrology,
   T. van Gardingen-Cromwijk, S. Konijnenberg, S. Witte, J.F. de Boer and A. den Boef, *Opt. Express* **32**, 36315 (2024).
6. Enhancing diffraction-based overlay metrology capabilities in digital holographic microscopy using model-based signal separation,
   T. van Gardingen-Cromwijk, S.G.J. Mathijssen, M. Noordam, S. Witte, J.F. de Boer and A.J. den Boef, *J. Micro/Nanopattern. Mats. Metro* **23**, 044006 (2024).
7. Diffraction-based overlay metrology using polarization-resolved dark-field digital holographic microscopy,
   M. Noordam, T. van Gardingen-Cromwijk, and A.J. den Boef, *J. Micro/Nanopattern. Mats. Metro* in submission.

8. Correcting spurious apodization effects in digital holographic microscopy using a simple Fourier transform spectrometer,
   J. Kim, T. van Gardingen-Cromwijk, M. Noordam, J.F. de Boer, Y. Kang, C. Park and A. den Boef, *Opt. Continuum* **4**, 382 (2025).

TEN SENTENCES

1. Although digital holographic microscopy is a well-established method for quantitative phase imaging, its potential for amplitude imaging remains relatively unexplored.
2. By measuring the full complex field, digital holographic microscopy allows for computational corrections of system imperfections.
3. High-quality complex optics are replaceable by simple optics when combined with computational correction techniques.
4. Model-based signal separation in combination with computational access to the pupil plane of the digital holographic microscope, results in a suppression of nuisance signals without the loss of resolution improving metrology performance on small targets.
5. Inherently vibration-sensitive measurement instruments, such as interferometers, can reliably function in industrial environments when appropriate mitigation strategies are applied.
6. Developing a novel metrology tool is only feasible with the close collaboration of like-minded researchers with different expertise.
7. It doesn't matter how beautiful your theory is, it doesn't matter how smart you are. If it doesn't agree with experiments, it's wrong. – Richard P. Feynman
8. If you do something for someone else, there will always be those willing to do something for you.
9. People who start walking before the train has stopped never end up first at the door.
10. A list of ten sentences is not the same as propositions.

ACKNOWLEDGEMENTS

In eerste instantie kies je voor een promotietraject omdat het onderzoeksonderwerp je aanspreekt. Wat het extra bijzonder maakt, is als je zoals ik, terecht komt in een omgeving waar niet alleen het onderwerp, maar ook de mensen om je heen leuk zijn. De werkomgeving en de directe contacten spelen een grote rol tijdens een promotietraject, en ik heb het geluk gehad om daarin een geweldige omgeving te hebben. Deze mensen hebben ervoor gezorgd dat ik heb genoten van mijn promotie de afgelopen jaren. Ik hoop dat zij al weten dat ik ze erg waardeer, toch wil ik ze nogmaals bedanken.

Arie, mijn promotor, bedankt dat je mij de kans hebt gegeven om een promotie te starten onder jouw supervisie ondanks het feit dat je geen open vacature had. Jouw kennis over de natuurkunde en de industriele toepassing daarvan, het altijd willen bewijzen door middel van experimenten en jouw rust, flexibiliteit en gevoel voor humor maken jou als persoon en promotor uniek. Op maandag ochtend even het weekend en de komende week bespreken met thee/koffie terwijl ARCNL nog zo goed als leeg was, was voor mij altijd een goed begin van de week. Ik heb veel natuurkunde van je geleerd tijdens onze discussies op een whiteboard of naast de lab opstelling. Aan het eind van de maandag hadden we altijd meer werk verzonnen dan dat ik in een week af kon krijgen. Juist dat maakt jou als promotor zo goed, na het bespreken van meetresultaten had jij altijd nieuwe experimentele ideeën, de groep stond nooit stil. Ik ben blij dat jij mijn promotor bent geweest en dat we nu als ASML collega's kunnen blijven samenwerken, bedankt!

Naast mijn promotor had ik het geluk om zelfs twee co-promotoren te hebben, Johannes en Stefan. Johannes, bedankt voor de positieve en toch kritische feedback die je elke twee weken gaf op mijn onderzoekswerk. Jouw kijk op ons werk gaf vaak nieuwe inzichten. Stefan, al was jouw begeleiding meer op de achtergrond, je hebt mij altijd het gevoel gegeven dat je betrokken en geïnteresseerd was. Bedankt dat je altijd eerlijk je mening gaf als ik mij af vroeg of ik wel de juiste keuzes maakte tijdens mijn promotie.

I would like to thank the committee members for carefully reading and providing valuable feedback: Lyuba Amitonova, Peter de Groot, Jeroen Kalkman, Allard Mosk and

Wim Ubachs.

Dan wil ik ook graag mijn collega's uit de Computational Imaging groep bedanken voor hun gezelligheid en hulp. Manashee, we both joined the group on the same day, you as a Post-Doc and I as a PhD student. I have enjoyed these past two years together spending time in the lab, attending conferences and exploring this for both of us new field of research together. Christos, the few months of overlap we had at ARCNL were very valuable for me. You taught me the fine details and trick of the experimental DHM setup. I am grateful for this smooth start, thanks to you. You also predicted the future quite well 4 years ago: "*I am sure that i will meet again with both of you in the near future, perhaps as colleagues once more*" [88]. I am looking forward to working with both of you in the lab again, this time at ASML. Marc, het was leuk om samen te werken in het lab. De DHM setup die jij in drie maanden tijd had staan vind ik nog steeds indrukwekkend. Bedankt dat je altijd wilde meedenken en (met behulp van een whiteboard) de ideeën duidelijk kon uitleggen. For one year we had Jongsu, an engineer from Samsung, joining our group. It was nice working with you in the lab, your humorous, hardworking and open character resulted in a nice publication of our work finally, thanks! Saad, thanks for being open and discussing less work-related topics during our lunch. I hope you will enjoy your new job and I wish the best to you and your family. Het jongste lid van de computational imaging groep, Nathan, heb ik mogen begeleiden tijdens zijn stage. Nathan, dankzij jouw enthausiasme en zelfstandigheid, verliep het vlekkenloos. Ook wil ik graag Sasha, Nick, Ksenia, Kian, Max, Wei, Zouphing, Tunc en Mengqi bedanken. Of het nou was met simulaties, experimenteel werk, het delen van samples of AFM metingen, jullie hebben allemaal bijgedragen aan dit proefschrift, bedankt!

Zonder technicus kan een promovendus in een lab niet goed werken, daarom bedankt ik graag Bartjan. Naast een technicus had ik ook het geluk dat ik gebruik mocht maken van de software support van AMOLF. Marco bedankt voor het ontwikkelen van de software ChoMore waar ik de hele setup mee kon aansturen vanaf de computer. Later hebben Jorijn en Ivo daar nog een mooie nieuwe versie van gemaakt die de high-speed camera ondersteunt. Bedankt voor jullie support!

Joost, Marjan en Wim, het managementteam van ARCNL, bedankt dat jullie ervoor hebben gezorgd dat je als PhD student bij ARCNL nergens zorgen om hoeft te maken. Jullie hebben een unieke omgeving gecreëerd waar ik met veel plezier heb gewerkt.

Naast ARCNL had ik het geluk dat ik één dag in de week bij ASML mocht komen. Hier mocht ik samenwerken en leren van mensen die het vakgebied en de industrie erg goed kennen. Als eerst wil ik Sander bedanken voor de mooie algorithmes en duidelijke vertaling van de theorie naar experimenten en andersom. Wim en Teus jullie hebben beide ook veel toegevoegd aan mijn proefschrift, bedankt voor de kritische vragen, goede ideeën en het reviewen van een aantal papers. Verder besef ik mij goed dat het een heel groot voordeel is geweest dat ik mocht samenwerken met mensen van ASML research, Alejandro, Patrick, Elbert, Greg, Perry, Robin, Longfei, Roxana, Andres, Armand, Tae Shik, Jo, Thomas, Irwan, Bram, Tom en Rafeeq bedankt daarvoor! Maarten, Coen en Richard bedankt dat ik welkom was bij ASML research tijdens mijn PhD, deze mogelijkheden hebben mij veel gebracht.

Simon, jij kwam de eerste keer naar ARCNL om samen aan cDBO te meten op de DHM opstelling. Ik was in het lab, de tijd vergeten en jou daardoor laten staan bij de receptie. Geen perfecte eerste ontmoeting als je het mij vraagt… Maar de samenwerking die daaruit volgde was naar mijn mening wel goed. Bedankt dat je mij altijd vooruit wilde helpen en mee wilde denken over de talloze onopgeloste puzzels die er nog liggen bij overlay metrologie, Hoofdstuk 8 van dit proefschrift is daar een mooi resultaat van. Ik weet zeker dat je een goede opvolger bent van Arie als groepsleider van de Computational Imaging groep. Ik zal jouw motto erin houden: "*Meten is weten, of weten dat je nog niet alles weet, of weten dat je nog niet alles gemeten hebt.*"

Verder wil ik nog mijn vrienden en familie bedanken, zonder jullie was het een stuk minder leuk geweest. Lieke, Tim, Jorn, Alicia, Anna en DSC3, bedankt voor de hechte vriendschap, ik kan altijd op jullie rekenen wat er ook is. Ik hoop nog veel gezelligheid, feestjes, etentjes en gekkigheid met jullie mee te maken. Mijn schoonfamilie, John en Herma, Marloes, Mike, Lex en Lester, bedankt voor jullie betrokkenheid, liefde en steun. Opa en Oma Bennekom, fijn om zulke lieve mensen als opa en oma te hebben. Opa Son, ook al is het dan in het, volgens jou, lelijkste universiteits gebouw van Nederland, ik ben blij dat jij mijn verdediging nog kan meemaken. Pap, bedankt dat jij mij altijd hebt meegenomen in het uitzoeken 'waarom' en 'hoe' dingen werken of juist niet werken, om het vervolgens samen te maken. Mam, bedankt voor je vertrouwen dat je mij geeft in de dingen die ik doe. En natuurlijk bedankt voor jullie liefde en betrokkenheid! Mijn broetje Menno en zijn vriendin Anouk en mijn zusje Hanna, jullie betekenen heel veel voor mij.

Mark, bedankt dat jij er altijd voor mij bent, de afgelopen 11 jaar met jou waren geweldig, ik kijk uit naar de rest van ons leven samen.

~ *Tamar*

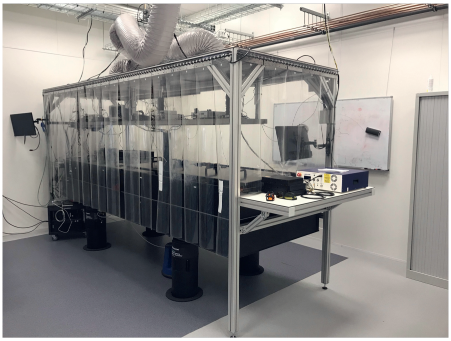

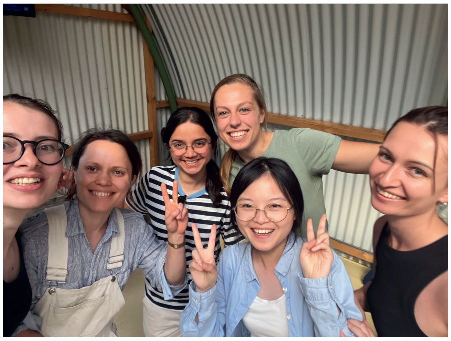

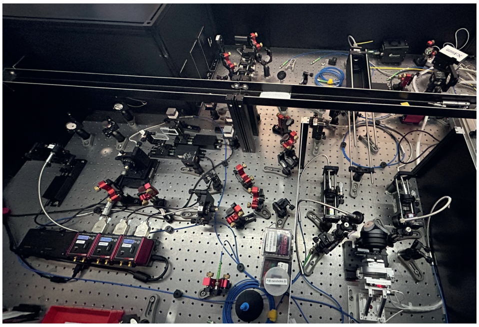

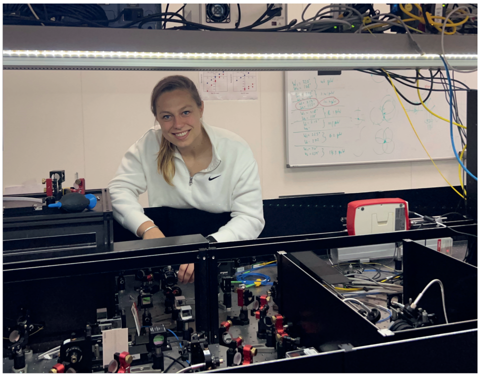

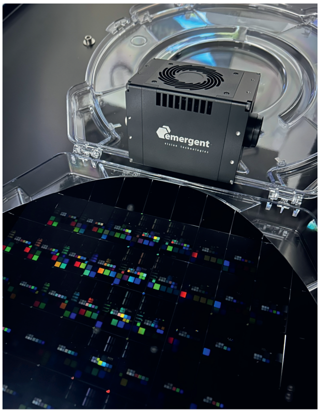
emergent

PERKIN—ELMER
200 Micralign

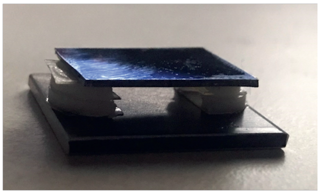

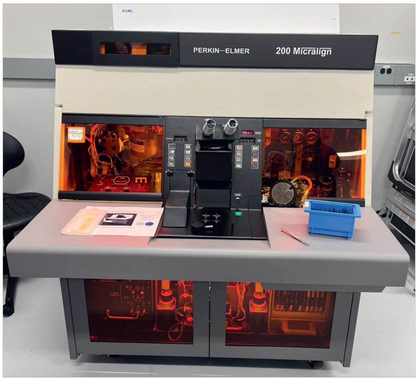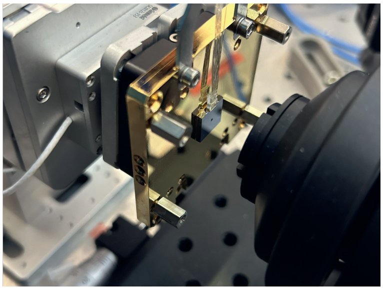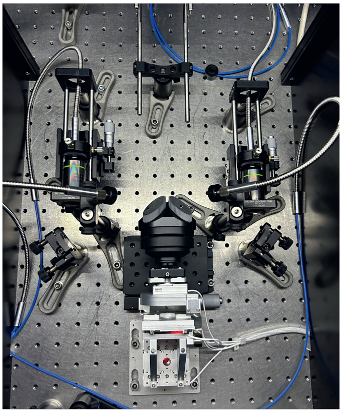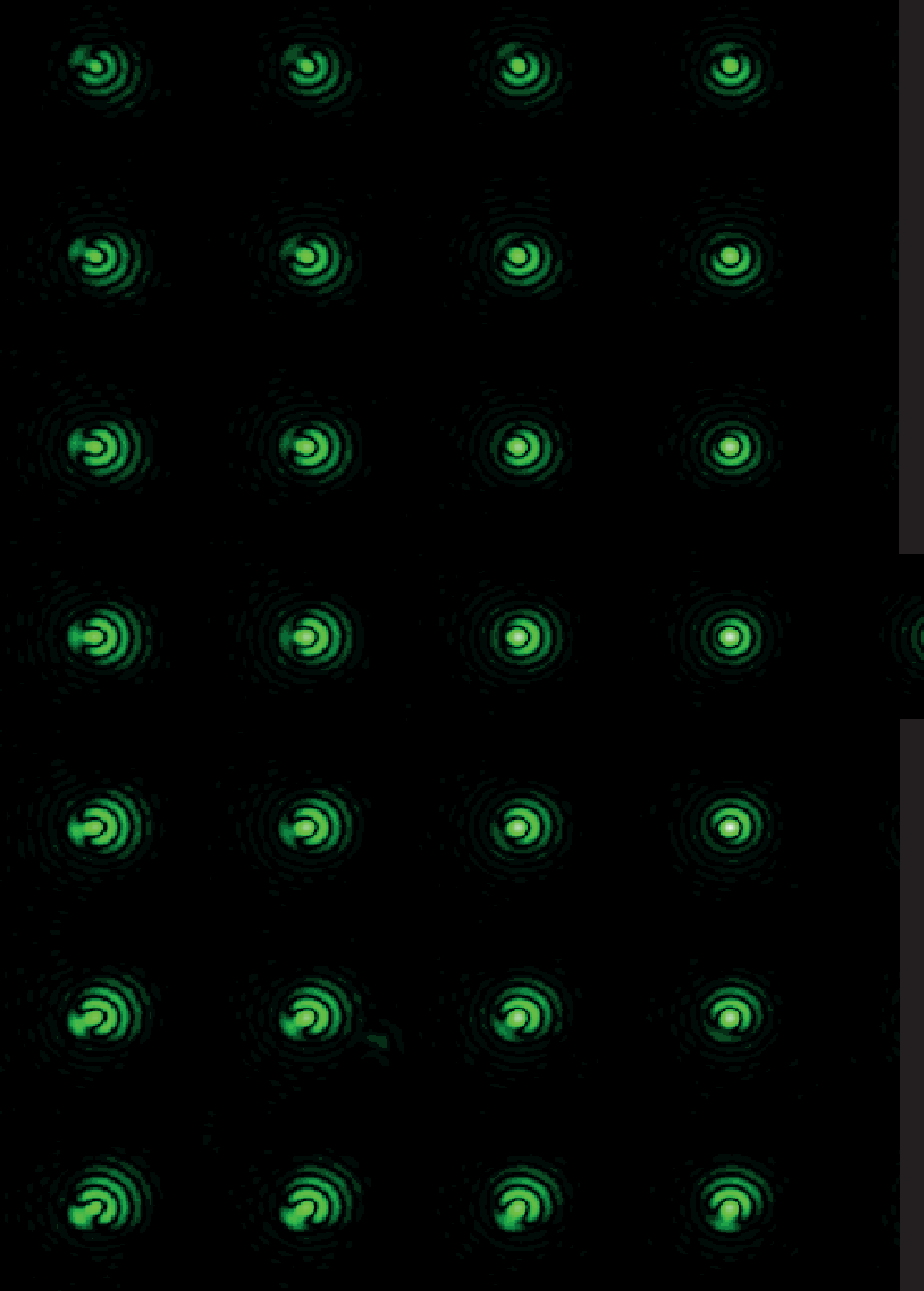
PERKIN—ELMER
200 Micralign